Design and Noise Characterisation of Electromagnetic Systems with Parity and Time-Reversal Symmetry

by

Hassan Farooq

A thesis submitted in the fulfilment of

the requirements for the degree of

Doctor of Philosophy

School of Electronic Engineering and Computer Science

Queen Mary, University of London

United Kingdom

November, 2019

Dedicated to my Family

Abstract

Parity-time (PT) symmetry is a unique space-time reflection symmetry that describes the system invariance to the combined parity (P) and time-reversal (T) operators. The parity operator corresponds to the interchange or inversion of spatial coordinates and the time-reversal operator inverts the time. PT-symmetry in electronics and electromagnetic systems is achieved by combining loss and gain in balanced proportions where loss is a conventional positive resistor and gain corresponds to a negative resistor. This judicious combination of loss and gain proportions has led to intriguing system behavior at exceptional points resulting in exotic wave manipulation effects such as non-linear propagation, negative refraction, sub-wavelength focusing, unidirectional cloaking and invisible sensors. Although such devices have been proposed in theory and proof of concept has been presented at low frequencies, practical implementation at microwave frequency ranges requires precise control and stability of loss-gain components with reduced noise figure. For instance, realisation of a negative resistor at microwave frequencies through active devices, such as bipolar junction transistors, operational amplifiers and tunnel diodes, is not only complex but also prone to instability and high noise figure levels which can further restrict the functional design of PT-symmetric devices. In addition, studies have shown that noise can break PT-symmetry by disturbing the loss and gain balance resulting in performance degradation of such devices. In this thesis, non-invasive design of PT-symmetric circuits to manipulate the reflection and transmission behaviour at microwave frequency ranges has been shown by incorporating an appropriate inductive or capacitive impedance while sustaining PT-symmetry. The studies begin with the design and investigation of ideal PT-symmetric circuits, where the loss, gain

and reactive elements are connected in either series or shunt configurations through a transmission line. The scattering parameters, exceptional points and eigenvalues for the aforementioned PT-symmetric circuit configurations have been shown. The research studies show that the PT-symmetric circuits in series or shunt configurations can behave as either, a cloaking structure or as a switching device, based on the choice of electrical line length. Studies in subsequent sections present the noise characterisation in terms of noise figure by incorporating realistic loss and gain circuit elements with equivalent thermal noise sources at the exceptional points of the PT-symmetric systems. It has been shown that noise in a two-port PT-symmetric systems distorts the location of its exceptional points, resulting in system's performance degradation in terms of increased reflections and the input and output port and reduced transmission towards port-2. In particular to cloaking applications, it has been shown that increased noise figure levels effect the performance of a PT-symmetric cloak by increasing its radar cross-section. The simulations have estimated and compared the performance of the noisy and ideal PT-symmetric cloak at microwave frequency range. Finally, practical implementation and realization of gain element in PT-symmetric systems is proposed with simulated and measured results.

Acknowledgements

I would like to express my gratitude towards my doctoral supervisors, Dr. Khalid Z. Rajab and Prof. Yang Hao for their consistent support, guidance and advise throughout the years of research studies. Without their professional supervision and persistent encouragement it would not have been possible to accomplish this PhD and it has been an honour to work under their professional supervision at Antennas and Electromagnetics research group at Queen Mary University of London. Besides my advisors, I would like to thank Dr. Kamyar Mehran for providing useful comments, encouragement and serving in my examination board. I would also like to thank Dr. Akram Alomainy, Dr. Rostyslav Dubrovka, Dr. Benjamin Vial, Dr. Deepak S. Nagarkoti and Dr. Atheer Barghouthi for their valuable comments, suggestions and support through the learning years.

I would also like to present my special thanks to Paul Denny, director of Peregrine Semiconductor, Theale, United Kingdom, for giving me access to the 5G millimetre-wave laboratory and providing me a great opportunity to further develop and understand valuable knowledge and industrial experience.

Finally, my deepest gratitude to my parents who inspired and encouraged me to stay focussed and provided unconditional love and support. I would also like to thank my siblings, Samia, Aqib and Usama for their encouragement and prayers throughout the years.

Last but not the least, I would like to express my thanks to my wife Sidra, whose prayers, patience, love and encouragement has made it possible to successfully accomplish my research studies.

Contents

Abstract ..... **iii**

Acknowledgements ..... **v**

List of Figures ..... **ix**

List of Publications ..... **xxiii**

1 Introduction **1**

1.1 Research Motivation and Objective 5

1.2 Research Questions and Contribution 7

1.3 Thesis Organization 9

2 Background Theory **11**

2.1 Fundamentals of Wave Electromagnetics 11

2.1.1 Time-Varying Maxwell's Equations 11

2.1.2 Boundary Conditions 13

2.2 Fundamentals of Parity-Time Symmetry 15

2.2.1 Parity-Reversal 15

2.2.2 Time-Reversal 17

2.2.3 Parity and Time-Reversal Symmetry 20

2.2.4 PT-Symmetry in Microwave Electronics 22

2.2.5 Scattering Matrix of a PT-Symmetric System 24

2.2.6 Exceptional Points of PT-Symmetric Systems 28

2.2.7 Negative Refraction Using PT-Symmetric Metasurfaces 31

2.2.8 Realisation of Gain in PT-Symmetric Circuits 34

2.2.9 Design Approaches for Negative Impedance Converters 35

a) BJT Based NIC 37

b) Operational-Amplifier Based NIC 41

c) Tunnel Diode Based NIC 44

d) Modern NIC Design Approaches 46

2.3 Noise Fundamentals of Active and Passive Systems 48
2.3.1 Thermal noise....49
2.3.2 Shot Noise....51
2.3.3 Flicker Noise....51
2.3.4 Realisation of Noise Figure....52
a) Noise Figure Measurement....53
b) Noise Figure Measurement by Y-Factor Method....55
c) Ultra-Fast Noise Figure Measurement....56
2.3.5 Noise Characterisation of Active and Passive Devices....58
a) Resistors and Thermal Noise Figure....59
b) Capacitors....60
c) Inductors....62
d) Transistors....63
e) Operational Amplifiers....64
f) Diodes....65
2.4 Summary....66
3 PT-Symmetric Circuit Design....67
3.1 PT-Symmetric Circuits in Series Configuration....68
3.1.1 Scattering Parameters....69
3.1.2 Eigenvalues and Exceptional Points....74
3.1.3 Reflectionless Transmission at Exceptional Points....75
3.2 PT-Symmetric Circuits in Shunt Configuration....78
3.2.1 Scattering Parameters....78
3.2.2 Eigenvalues and Exceptional Points....81
3.2.3 Reflectionless Transmission at Exceptional Points....82
3.3 Cascaded PT-Symmetric Systems....87
3.4 Summary....89

4 Noise Characterisation of PT- Symmetric Circuits 91
4.1 Noise Figure of PT-Symmetric Circuit in Series 92
4.2 Noise Figure of PT-Symmetric Circuit in Shunt 95
4.3 Summary 99
5 Noise Performance of PT-Symmetric Applications 101
5.1 Cloaking and Invisibility Based on PT-Symmetry 101
5.1.1 An Ideal Unidirectional PT-Symmetric Cloak 102
5.1.2 A Reconfigurable Cloak Based on PT-Symmetry 104
5.2 Noise Performance and Detection of a PT-Symmetric Cloak 111
5.3 An Electromagnetic Switch Based on PT-Symmetry 118
5.4 Summary 121
6 Gain Implementation in PT-Symmetric Circuits and Potential Applications of Negative Impedance Structures 124
6.1 Experimental Model of a PT-Symmetric Circuit 124
6.1.1 Gain Element by Using a Tunnel Diode 125
6.1.2 Gain Element by Using Operational Amplifier 128
6.2 Sensitivity Analysis of Exceptional Points 133
6.3 Potential Applications of Negative Impedance Structures 135
6.3.1 Non-Foster Antenna Arrays for Navigation Platforms 137
a) Accuracy in Angle-of-Arrival Based Approaches 138
b) Accuracy in Time-of-Arrival Based Approaches 139
6.4 Summary 141
7 Discussion and Summary 143
7.1 Summary of the Work Presented in This Thesis 143
7.2 Future Research Work 147
References 149

List of Figures

Fig. 1.01. Parity-time symmetry can lead to real eigenvalues of a system. 1

Fig. 1.02. Simple illustration of a gain/loss system. (a) An unstable isolated gain system. (b) An unsustainable isolated loss system. (c) Stable system with coupled loss and gain. 2

Fig. 1.03. Counts of publications on Parity-Time Symmetry. Data source: Scopus, publication query service accessed on 26 June 2019. 3

Fig. 1.04. Notable PT-symmetric applications in recent years. 4

Fig. 2.01. Fields at a general interface between two different mediums... 15

Fig. 2.02. (a) Transformation Current carrying loop, (b) Assumption of Magnetic field in wrong orientation after parity transformation. 16

Fig. 2.03. (a) Transformation of current carrying loop. (b) Magnetic field transformation in accordance with Ampere's law in correct orientation after transformation. 16

Fig. 2.04. Circuit transformation under Parity (P) operator. 17

Fig. 2.05. Combined PT-symmetry transformation on a system with loss and gain coupled together with a coupling mechanism. 21

Fig. 2.06. A simple electronic circuit under parity-reversal operation with loss and gain impedances connected together through a transmission line..... 23

Fig. 2.07. The circuit shown in Fig. 2.06 undergoing a time-reversal operation. The resistive impedances flip their signs under time-reversal operation. The circuit is PT-symmetric because it is invariant after the combined transformation of parity and time-reversal. 23

Fig. 2.08. Schematic illustration of a two-port microwave scattering system. 24
Fig. 2.09. The two-port microwave scattering system after PT-transformation..... 25
Fig. 2.10. Schematic of the two-port PT-symmetric system modelled as two lumped resistors with a transmission line such that $R_1 = rZ_0$ and $R_2 = -rZ_0$ 27
Fig. 2.11. Circuit simulation setup in Keysight ADS. The two resistors are chosen such that their impedance is twice to that of the characteristic line impedance to reach the exceptional point. ... 30
Fig. 2.12. Simulated s-parameter plot of the PT-symmetric circuit. 30
Fig. 2.13. Equivalent full-wave electromagnetic simulation setup for the schematic shown in Fig. 2.11. The lumped resistors with loss and gain are modelled as an ultrathin metasurface with loss and gain respectively..... 32
Fig. 2.14. Time snapshot of a plane wave incident at 30 degrees on PT-symmetric metasurfaces with loss and gain respectively. The backward power flow is sustained by the active metasurface on the right. 33
Fig. 2.15. Time snapshot of a Gaussian wave incident at an angle of 30 degrees on PT-symmetric metasurface undergoing negative refraction. The backward power flow is being sustained by the active metasurface on the right..... 33
Fig. 2.16. Equivalent voltage-current relationship diagram for Linvill's NIC. 37
Fig. 2.17. Linvill's open-circuit stable NIC design based on cross-coupled BJTs with port-1 as input and port-2 as output/load..... 38

Fig. 2.18. Equivalent circuit model of Linvill's open circuit stable negative impedance converter. 39
Fig. 2.19. Input impedance plot of various transistor's cut-off frequency. A flat negative impedance is achieved using transistors with high cut-off frequency levels. 41
Fig. 2.20. Op-Amp based current inversion NIC circuit. 42
Fig. 2.21. Input voltage measurement across op-amp with a load of1000 Ω at 10 MHz. 43
Fig. 2.22. The output current undergoes 180 degrees phase change resulting in negative impedance. 43
Fig. 2.23. Voltage-current behaviour of a tunnel diode. A small biasing voltage results in large tunnelling current exhibiting first positive differential resistance region. After reaching peak biasing voltage the tunnelling current rapidly falls resulting in NDR. After reaching valley voltage second positive differential resistance (PDR) region is observed. 44
Fig. 2.24. RTD structure with the emitter, collector and double-barrier quantum-well. The resonant energy levels of the electrons enables them to tunnel through the double-barrier. 45
Fig. 2.25. Measured negative resistance of RTD L939F [64]. 46
Fig. 2.26. Photograph of the fabricated NIC with the red box showing its location [69]. 47
Fig. 2.27. Measured negative inductance and resistance of the NIC [69]. 47
Fig. 2.28. Dominant noise sources in comparison with flicker noise. 52
Fig. 2.29. (a) Signal level at the amplifier input. (b) The signal level at amplifier output with internal and amplified noise. 53
Fig. 2.30. Power output against source temperature characteristic of linear, two-port device. The output power is increased by thermal noise

from the source and amplification by the gain parameter of the DUT. 54
Fig. 2.31. Series noise source generator by Agilent. Photo by the courtesy of Peregrine Semiconductor, United Kingdom. 55
Fig. 2.32. Y-factor method using two noise sources at hot and cold noise temperatures. 56
Fig. 2.33. Block diagram of the noise measurement setup. 57
Fig. 2.34. Noise parameters measurement setup with load tuner and noise receiver on a probe station fixture with a DUT. Photograph taken on 9th September 2019 by the courtesy of Peregrine Semiconductor, UK. 58
Fig. 2.35. Thevenin equivalent of a noisy resistor. 59
Fig. 2.36. Norton equivalent of a noisy resistor. 59
Fig. 2.37. Equivalent model of a capacitor with parallel resistance producing thermal noise. 60
Fig. 2.38. A non-ideal capacitor with thermal noise source, delivering power to resistive load. 61
Fig. 2.39. Equivalent model of a non-ideal inductor with series resistance producing thermal noise voltage. 62
Fig. 2.40. Equivalent BJT circuit model of noisy BJT with noise sources. 63
Fig. 2.41. Equivalent circuit model of a noisy operational amplifier. The thermal noise sources, shot noise, and flicker noise sources have been modelled. 64
Fig. 2.42. A two-port small-signal equivalent model of a tunnel diode. ... 65
Fig. 3.01. A two-port PT-Symmetric circuit in series configuration with resistors R_1, R_2 connected together by a tranmission line of length $x = kd$ and an imaginary impedance given by a capacitive or

inductive element. The time-reversal symmetry is applied through negative resistor R_2 with equal magnitude as positive resistor R_1 68

Fig. 3.02. Scattering parameters of the PT-symmetric circuit as a function of electrical length and capacitive reactance in series configuration at an exceptional point of $r = 1$. The schematic diagram has been shown in Fig. 3.01. 72

Fig. 3.03. Scattering parameters of the series PT-symmetric circuit as a function of electrical length and inductive reactance at an exceptional point of $r = 1$. The schematic diagram has been shown in Fig. 3.01. 73

Fig. 3.04. Eigenvalues of the series PT-symmetric circuit as a function of reactance and non-Hermiticity parameter r. The exceptional point occurs at $r = 1$, showing a phase transition of the system. 74

Fig. 3.05. Scattering parameters in complex plane as a function of reactance and non-Hermiticy parameter r. The system always exhibits zero reflection coeffecient at port-1 and unitary tranmission to port-2, regardless of the reactance. However, the output reflection is described by the selection of reactance. Two cases have been shown at 1.5 GHz. (a) At a capacitance of 4.45 pF the system shows unitary output reflection. (b) At a capacitance of 2.12 pF, the output reflection coeffecient magnitude increases to two. (c) At an inductance of 2.65 nH the output reflection coeffecient is 1. (d) At and inductance of 5.3 nH the output reflection magnitude increases to twice. The red arrows correspond to exceptional point of the PT-symmetric circuit. 76

Fig. 3.06. Scattering parameters of a PT-symmetric circuit as a function of series reactance through a capacitor and inductor at an exceptional point of $r = 1$ 77

Fig. 3.07. A two-port PT-Symmetric circuit in shunt configuration with loss and gain resistors R_1, R_2 are connected together by a transmission line and an imaginary impedance X which may be given by a capacitor or inductor. The time-reversal symmetry is applied through negative resistor with equal magnitude as positive resistor. 78

Fig. 3.08. Scattering parameters of the shunt PT-symmetric circuit as a function of electrical length and capacitive reactance at an exceptional point of $r = 1$. The schematic diagram has been shown in Fig. 3.07. 79

Fig. 3.09. Scattering parameters of the shunt PT-symmetric circuit as a function of electrical length and inductive reactance at an exceptional point of $r = 1$. The schematic has been shown in Fig. 3.07. 80

Fig. 3.10. Eigenvalues of the shunt PT-symmetric circuit as a function of reactance and non-Hermiticity parameter r. The exceptional point occurs at $r = 1$, showing a phase transition of the system. 81

Fig. 3.11. Scattering parameters in complex plane as a function of capacitive or inductive reactance, and the non-Hermiticy parameter r at an electrical length of $n\pi / 2$. The two-port system is matched from port-1 with unity transmission regardless of the reactance. However, the output reflection is described by the selection of reactance. (a),(c) Capacitance of 1.1 pF or an inductance of 10.6

nH yields $S_{22} = 1$. (b),(d) Capacitance of 2.12 pF or an inductance of 5.3 nH, the output reflection coeffecient increases to twice... 82

Fig. 3.12. Scattering parameters of a PT-symmetric circuit in shunt configuration as a function of shunt reactance through a capacitor and inductor at an exceptional point of $r = 1$. The capacitor offers a linear response in manipulating output reflection whereas an inductor shows asymptotic behaviour. 84

Fig. 3.13. Geometric setup of the PT-symmetric circuit with loss, gain and reactive elements modelled as a uniform ultrathin respective impedances. 85

Fig. 3.14. Time snapshot of full-wave simulation for the PT-symmetric circuit in shunt configuration at 1.5 GHz. When the system is excited from port-1, the incident EM wave is transmitted through the structure without any perturbation with a forward tranmission coeffecient of unity. The black arrows represent average power flow in the system also known as Poynting vector. 85

Fig. 3.15. Time snapshot of full-wave simulation for the PT-symmetric circuit with an incident wave at port-2. A capacitance of 1.1 pF or an inductance of 10.6 nH yields $S_{22} = 1$. 86

Fig. 3.16. Time snapshot of a full-wave simulation with an excitation from port-2 and a capacitance of 2.12 pF or an inductance of 5.3 nH. The output reflection coefficient is increased to a magnitude of 2. 87

Fig. 3.17. A generalized illustration of a PT-symmetric system with balanced loss and gain modelled as positive and negatives resistor connected together through a simple transmission line, a mutually coupled transformer or a complex passive network. 88

Fig. 3.18. Two cascaded PT-symmetric systems coupled together with an imaginary impedance. Each individual PT-symmetric system is composed of loss and gain resistors with satisfied parity and time-reversal symmetry conditions. The cascaded system also holds PT-symmetry. 88

Fig. 4.01. Schematic from section-3 of series PT-symmetric circuit with ideal lumped elements. The system is free from any associated noise and system losses. 93

Fig. 4.02. Equivalent noise circuit model of the series PT-symmetric circuit. The ideal negative resistance originates through the tunnel diode and therefore has been replaced by its equivalent noise circuit model. 94

Fig. 4.03. Analytical and simulated noise figure of the PT-symmetric system in series at the exceptional point of $r = 1$. The characteristic line impedance Z_0 is 50 Ω. 95

Fig. 4.04. Schematic from section 3.2 of shunt PT-symmetric circuit with ideal lumped elements. The system is assumed to be free from any associated noise and system losses. 96

Fig. 4.05. Equivalent noise model of the shunt PT-symmetric circuit. The thermal noise originates through the loss resistor and internal resistance of the tunnel diode which provides a negative resistance of -49.77 Ω. 97

Fig. 4.06. Analytical and simulated noise figure of the PT-symmetric system in shunt configuration at the exceptional point of $r = 1$. The characteristic line impedance Z_0 is 50 Ω. 98

Fig. 5.01. (a) A simple two-port transmission line model of an ideal unidirectional PT-symmetric cloak. (b) The lossy part of metasurface is composed of conventional positive resistors whereas

the gain metasurface is composed of negative resistors. The horizontal lines show the connecting transmission lines of different length between the loss and gain resistors with satisfied PT-symmetry at the exception point of $r = 0.5$ (c) The incoming plane wave is transmitted through the PT-symmetric structure rendering it invisible to incoming waves. 103

Fig. 5.02. An uncloaked target being illuminated by incident waves from a radar antenna. The target gets reflects the incident electromagnetic waves and gets detected by its radar cross-section approximation. 105

Fig. 5.03. Full-wave simulation setup for system shown in Fig. 5.02. The red arrow represents the excitation direction. 106

Fig. 5.04. An uncloaked target being illuminated by a plane wave incident from the left. The detection is caused due to the large RCS approximation caused by the scattered electric field distribution and the target's shadow on the right. The red arrow represents the direction of the incident wave. The electric field shown is a time snapshot whereas the RCS calculation is an average value. 107

Fig. 5.05. PT-symmetric metasurface constructed from a series PT-symmetric circuit configuration. The reactive element X has a complex impedance originating through a capacitor or an inductor. 108

Fig. 5.06. PT-symmetric metasurface constructed from a shunt PT-symmetric circuit configuration. 108

Fig. 5.07. A PT-symmetric cloaked target with loss (blue) and gain (red) is been shown which is at a sufficient distance from the radar

antenna such that the incoming wave can be considered as a plane wave. 109
Fig. 5.08. Simulation setup for the full-wave electromagnetic simulation for the system shown in Fig. 5.07.....109
Fig. 5.09. (a) Time snapshot of the PT-symmetric metasurface showing that an illumination from the loss side exhibits perfect invisibility under ideal, loss-free conditions. (b) Time snapshot of the PT-Symmetric metasurface showing that the structure illumination from the gain side with an appropriate series or shunt reactance results in bidirectional invisibility. The RCS is an independent value with respect to time and is averaged for incident and scattered electric fields over 360 degrees.....111
Fig. 5.10. The thermal noise current has random Gaussian distribution with a range equal to peak noise current. The probability of finding the peak noise current at any instance of time would be 99% if it is six times of root mean square noise current. Therefore $i_p = 6i_{rms}$. 114
Fig. 5.11. Noise figure for PT-symetric circuits in both shunt and series configurations. The negative resistor of -49.77 Ω originates through resonant tunnel diode of sample L939F with an internal resistance of 7 Ω at a biasing voltage of 2.65 volts at 1.5 GHz. 115
Fig. 5.12. Time snapshot for; (a) An uncloaked target being detected by its RCS approximation and scattered field distribution. (b) A noise-free PT-symmetric metasurface cloak renders the target invisible by reducing its RCS to an extremely low value of -60 dB per unit length under ideal conditions. (c) Using a metasurface cloak with series PT-symmetric circuit topology exhibits a noise figure level

of 3.31 dB, the RCS is increased to -30 dB per unit length. (d) Using a metasurface cloak by following shunt circuit configuration the noise figure approximates to 9.7 dB with an RCS of -10 dB/m. (e) A noise figure level of 20 dB significantly degrades the cloaking performance to a level where the RCS estimation from an uncloaked and cloaked target are comparable. The RCS approximation is an time-independent value which is averaged for 360 degrees incident and scattered electric fields.....116

Fig. 5.13. Time snapshot of the full-wave electromagnetic simulation in ON state. A capacitance of 0.01 pF the system experiences zero reflections at input and output ports and a unity transmission towards port-2. The red arrow shows the excitation direction whereas the black arrows represent the average power flow in the system towards port-2.....120

Fig. 5.14. Time snapshot of a full-wave electromagnetic simulation in OFF state. At a capacitance of 20 pF the system experiences unity input reflection and zero transmission towards port-2. The system has been configured using a shunt configuration however similar results can be obtained by following a series design or appropriate inductance range. 121

Fig. 6.01. An equivalent circuit model of a tunnel diode with parasitics and a pure negative resistance provided by the diode itself in the negative differential region.....125

Fig. 6.02. Tunnel diode IV characteristics measurement setup using Keysight B2912A commanded through MATLAB. The diode bias voltage is precisely swept and the current measurement is recorded. The input and output RF ports have been terminated to 50 Ω. 126

Fig. 6.03. Photograph of the actual measurement setup for DC characteristics of the tunnel diode by using Keysight B2912A and MATLAB. 127
Fig. 6.04. The measured voltage-current curve of the diode. The diode provides a negative resistance of -50.1 Ω at a biasing voltage of 0.191 mV. 128
Fig. 6.05. Schematic diagram for Texas Instruments THS4303 wideband operational amplifier. 129
Fig. 6.06. One-port grounded negative resistance using THS4303 operational amplifier. This op-amp based design is suitable for PT-symmetric circuits designed in shunt configurations. 129
Fig. 6.07. Simulation setup of a one-port grounded negative resistor using Texas Instruments THS4303 operational amplifier. 130
Fig. 6.08. Input impedance of the one-port grounded negative resistance using THS4303 operational amplifier. 130
Fig. 6.09. Schematic of a floating two-port negative impedance converter circuit using two cross-coupled THS4303 operational amplifiers. The inductors at the two terminals are responsible to negate the imaginary part of the input impedance given by the NIC. 131
Fig. 6.10. Simulation setup of the two-port floating negative impedance converter using cross-coupled Texas Instruments THS4303. 132
Fig. 6.11. Simulated results for the two-port floating negative resistance using THS4303. 132
Fig. 6.12. Effect of an uncertain magnitude of the gain resistor on the performance of a PT-symmetric system. 134
Fig. 6.13. Antenna impedance matching: a) conventional matching with an inductive reactance to cancel out a capacitive antenna at a single

frequency; b) non-Foster element, -C to negate the capacitive reactance over a wider frequency range. 136
Fig. 6.14. A general setup for a direction-finding system. 137
Fig. 6.15. Required SNR for N Electrically small antenna elements and specific angle precision σ; showing that for a specific array size D/λ, a dense array with more elements will require a lower SNR. 139
Fig. 6.16. Cramer-Rao lower bound for range estimation with various bandwidths.....140
Fig. 6.17. ESA arrays in a constant physical space with (a) N=3 passive elements with fundamental size limit and; (b) N=5 non-Foster elements, which for the same bandwidth, can be smaller in size. 141

List of Abbreviations

BJT	Bipolar Junction Transistor
EP	Exceptional Point
ESA	Electrically Small Antenna
H	Hamiltonian
$H^{\dagger}$	Hermitian
M	Transmission Matrix
NDR	Negative Differential Region
NF	Noise Figure
NFA	Non-Foster Antenna
NFC	Non-Foster Circuit
NIC	Negative Impedance Converter
NR	Negative Refraction
OCS	Open Circuit Stable
PDR	Positive Differential Region
PT	Parity-Time
PTS	Parity-Time Symmetry
Q	Quality Factor
QM	Quantum Mechanics
RF	Radio Frequency
RSS	Received Signal Strength
RTD	Resonant Tunnelling Diode
S	Scattering Matrix
SCS	Short Circuit Stable
SNR	Signal-to-Noise Ratio

List of Publications

Journal Publications

1) **H. Farooq**, K. Z. Rajab & Y. Hao, "Noise Figure of Electromagnetic Systems with Parity and Time-reversal Symmetry" Opt. Express 13, 373143 (2019). (Highlighted as an editor's pick 2019).

Conference Proceedings

1) **H. Farooq**, D. S. Nagarkoti, K. Z. Rajab, & Y. Hao, (2019, March). Noise Figure of a Unidirectional Cloaking Circuit Based on Parity-Time Symmetry. In *2019 13th European Conference on Antennas and Propagation (EuCAP)* (pp. 1-3).

Chapter 1

Introduction

Parity-time symmetry is a unique space-time reflection symmetry which was discovered as a weaker condition to Hermiticity. The discovery enabled to study and observe new class of systems which may have completely real eigenvalues provided that the system is invariant under combined parity (P) and time-reversal (T) transformations [1–5]. Real eigenvalues also correspond that the system is stable and physically observable. Prior to this discovery it was believed that real spectra can only be observed if a Hamiltonian is Hermitian [6–7]. Where a Hamiltonian describes the total energy of a system. Fig. 1.01 shows the overlapping of non-Hermitian system having real spectrum with satisfied PT-symmetric condition.

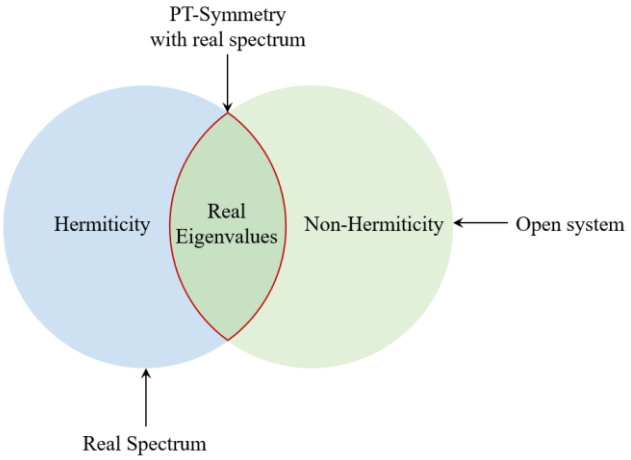

Fig. 1.01. Parity-time symmetry can lead to real eigenvalues of a system.

This concluded that Hermiticity is not the only condition to obtain real eigenvalues of a system and as long as the PT-symmetric condition $V(r) = V^*(-r)$ is satisfied, the non-Hermitian Hamiltonians can also have a real spectrum. Here, V describes the potential of quantum system and *

denotes complex conjugation. The discovery sparked a great surge of research efforts in order to further study the new class of PT-symmetric Hamiltonians. The concept of a PT-symmetric system is further explained in [2] where a simple system has been described with loss and gain coupled together with a coupling factor in terms of a matrix notation as

$$H = \begin{bmatrix} -j\alpha & \gamma \\ \gamma & +j\alpha \end{bmatrix} \tag{1.1}$$

The system given in Eq. (1.1) is interestingly identical to an eigenvalue matrix problem with source and drain that are linked together with some coupling factor. Where $+\alpha$ and $-\alpha$ representing loss and gain respectively and γ represents the coupling coefficient. In a convenient notation, PT-symmetric system can be expressed as a loss-gain system coupled together with a coupling mechanism as shown in Fig. 1.02.

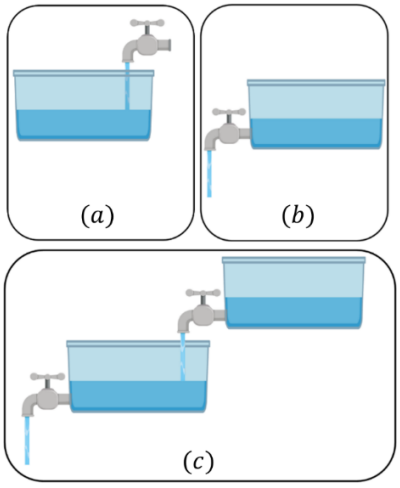

Fig. 1.02. Simple illustration of a gain/loss system. (a) An unstable isolated gain system. (b) An unsustainable isolated loss system. (c) Stable system with coupled loss and gain.

It can be noticed that a system with a single gain source is unstable due to a growing (unbounded) state of energy. Similarly, a system with a

standalone loss or a sink source is also unstable because of the decaying state of energy. However, if the source and the sink are connected together with a balancing/coupling mechanism, the new system is a stable system. The growing energy state of the system has been compensated through decay or loss, whereas the decaying energy state has been compensated through gain. Because the two states have been coupled together, the new system is stable.

Until 2007, PT-symmetry was only limited to quantum mechanics, however further research studies confirmed the potential of PT-symmetry in optics such as optical waveguides and lattices by incorporating spatial regions with optical loss and gain in balanced proportions and by using varying refractive indices [8–9]. It has been noted in particular that great amount of research studies are being performed in PT-symmetry which have been further extended into interesting engineering and electronics publications.

Fig. 1.03 shows the publication data count on PT-symmetry and it is evident that since the initial discovery of PT-symmetry, the amount of research activity has grown exponentially over the years with wide ranging applications.

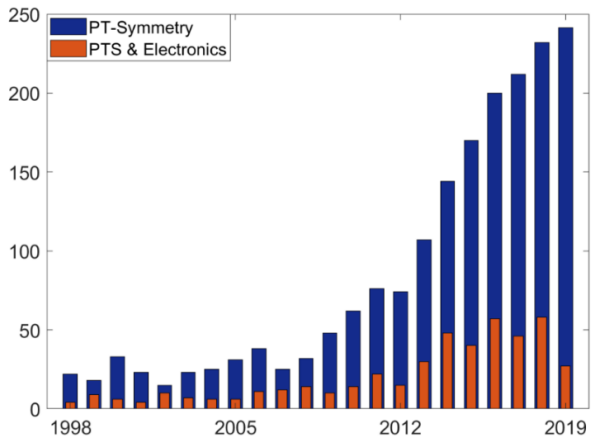

Fig. 1.03. Counts of publications on Parity-Time Symmetry. Data source: Scopus, publication query service accessed on 26 June 2019.

Recent research studies have proposed novel PT-symmetric applications in acoustics electronics such as unidirectional loss-less acoustic sensors [10–14], electromagnetics such as oscillators and waveguides [15–17], photonics such as optical isolators and lattices[18–23], mechanical oscillators with loss and gain feedback loop to achieve single mode oscillation [24], non-linear electromagnetic wave propagation and sub-wavelength focusing such as super lensing [25], active cloaking and invisibility [26–33] and robust long range wireless power transfer [34].

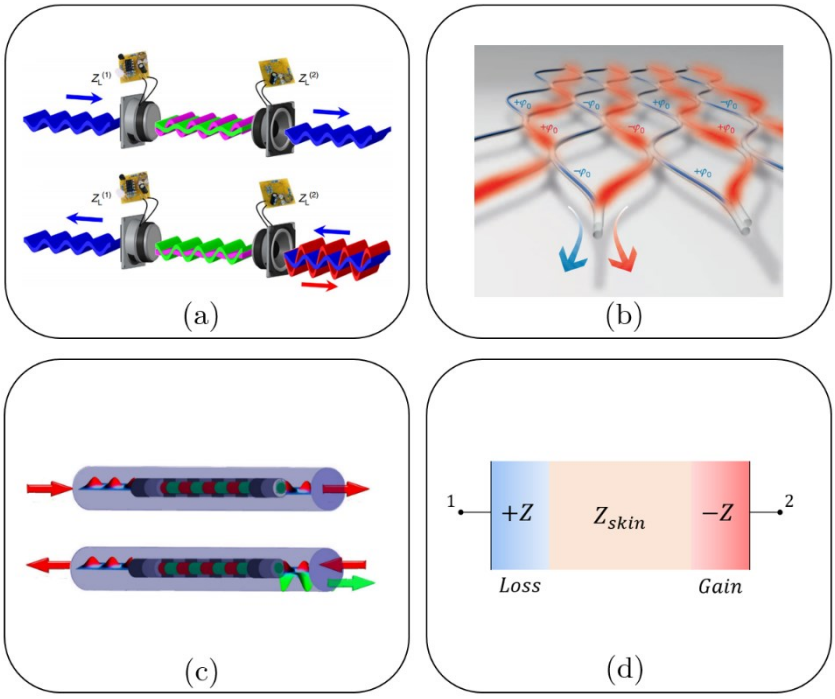

Fig. 1.04. Notable PT-symmetric applications in recent years.

Fig. 1.04 shows the notable PT-symmetric applications proposed in recent years. For instance, [11] showed a unidirectional transparent acoustic sensor based on PT-symmetry, where electro-acoustic resonators loaded with loss and gain were employed to successfully detect an incoming signal without

perturbing the incident acoustic signal. Further study in [18] demonstrated that a fibre loop mesh network with optically switched loss and gain in balanced proportions can achieve unidirectional propagation. Another study was demonstrated in [26] where a PT-symmetric Bragg grating with optical gain and loss regions was employed to experience unidirectional reflectionless propagation. The wave entering from one side of the PT-symmetric structure gets transmitted towards port-2 without any reflection as if the structure is not present, however a wave entering from the port-2 experiences an enhanced reflection. Another study in [35] showed a non-invasive technique to detect the change in blood glucose levels by measuring the electromagnetic frequency shift through a PT-symmetric system with loss and gain. The loss due to the skin is balanced by the equivalent amount of gain by a PT-symmetric system and the resonance shift is able to detect the blood glucose level without using any skin invasion techniques.

1.1 Research Motivation and Objective

PT-symmetry in electronics and electromagnetic systems is achieved by judiciously combining loss and gain in balanced proportions through a coupling mechanism such as a transmission line or an inductive transformer. The loss element simply corresponds to a conventional resistor ($+R$) that dissipates energy over time whereas the time-reversed version of such component already exists in electronic circuits in the form of a negative resistor ($-R$). Negative resistors does not exists as a standalone circuit element however can be engineered through negative impedance converter (NIC) circuits with active elements such as transistors, operational amplifiers and tunnel diodes. The design complexity and stability of a NIC varies depending upon the operating frequency and application requirements.

Research studies have shown that NIC stability is achievable through careful design considerations [36]. However, dominant noise inclusion such as thermal noise, is a fundamental property of electromagnetic systems operating at microwave frequencies and therefore cannot be neglected in a practical system. In addition, the realisation of a negative resistor through NIC is itself complex, challenging, and is prone to instability and high noise figure levels which effectively restrict the application design of functional PT-symmetric devices. Further studies in [37] have shown that noise can weakly break PT-symmetry hence performance of such devices in practical is expected to be degraded up to a certain threshold which is defined by the system noise figure.

Conclusively, it is evident that practical implementation of functional PT-symmetric devices such as invisibility cloaks [28–30], sensors [11] and other devices operating at microwave frequency ranges is an arduous task. The realisation of such devices in practical are primarily bottlenecked by instability and high noise figure constrains. While a stable system may be realised through prudent design considerations, noise would still be a fundamental inclusion degrading the performance and therefore requires further consideration.

In context to this thesis, the presented work primarily investigates the noise characterisation, modelling and performance of PT-symmetric systems and their potential application design. The realisation of such systems at microwave frequency ranges has been shown by combining passive (loss) and active (gain) elements together in parity and time-reversed pairs through a transmission line. Reflection and transmission properties of aforementioned systems can be manipulated by incorporating an appropriate imaginary impedance in the system while sustaining PT-

symmetry. Application design of a PT-symmetric system exhibiting reflectionless unidirectional or bidirectional transmission, unidirectional cloaking with reconfiguration and tuning capabilities, EM switches and enhanced signal reflectors has been proposed.

Further, PT-symmetric circuit design configuration in series and shunt topologies has been discussed and noise figure has been calculated by using analytical and simulation methods. Particularly, for cloaking applications, performance of a PT-symmetric cloak has been analysed in terms of radar cross-section in realistic environments with various noise levels. Finally, practical implementation of gain element for PT-symmetric devices has been shown along with simulated and measured results.

1.2 Research Questions and Contribution

The fundamental research questions and the contribution to the subject of PT-symmetry in microwave electronics has been presented in this section.

Research Questions

- Novel applications and wave-manipulation effects based on PT-symmetry have been proposed and demonstrated in optics and acoustics. How these concepts can be realized and implemented in microwave electronics and at microwave frequencies for novel applications.
- A study in quantum physics has shown that PT-symmetry can be weakly broken due to quantum noise. Based on this finding and relating this to RF and microwave electronics, can thermal noise effect the performance of a PT-symmetric system at RF

and microwave frequency ranges. If it does, what would be the performance levels of PT-symmetric devices and applications.

- PT-symmetry in optics with has been studied to provide unidirectional reflectionless transmission. Can an equivalent study be performed in RF and microwave electronics and cloaking model can be developed and studied. Further in this regards, a noise characterisation may be performed to estimate noise figure levels and detection thresholds of a PT-symmetric cloaked target.

Contribution Summary

- Proposed a non-invasive design technique to manipulate the reflection and transmission properties of PT-symmetric circuits in microwave electronics.
- Proposed and presented novel, reconfigurable and scalable PT-symmetric systems at microwave frequencies to be employed for cloaking and switching applications.
- Performed noise characterisation and performance study of aforementioned PT-symmetric applications. The studies have been performed using analytical methods, circuit level and full-wave electromagnetic simulations and measurements.
- Performed a sensitivity and robustness study of aforementioned PT-symmetric systems. And proposed the design of gain element using a negative impedance converter. The negative impedance converter can be designed as a floating one-port (narrow band) or grounded 2-port (wide-band) design by using an op-amp at 1.5 GHz.

1.3 Thesis Organization

Chapter 2 presents the fundamental concepts of electromagnetics, negative impedance converters and PT-symmetry that form the foundation of the research work presented in this thesis. The chapter begins with the discussion of time-harmonic electromagnetic fields and discusses the fundamental postulates of PT-symmetry in electronics and microwave circuits. The chapter further discusses the scattering matrix formulation of a PT-symmetric microwave system and then explains the concept of a negative impedance converter circuits and their potential design techniques. Finally, the chapter discusses about the fundamental noise sources in a microwave system and equivalent noise models of active and passive elements.

Chapter 3 presents PT-symmetric circuit design in series and shunt configurations and discusses the scattering matrix formulism of the PT-symmetric systems. It also defines the unique exceptional points in PT-symmetric system and explains the necessary loss, gain and transmission line conditions to achieve such points for unique wave manipulation effects. The chapter then discusses the required scattering matrix condition to realize unidirectional reflectionless transmission.

Chapter 4 presents the noise characterisation of the PT-symmetric circuits explained in Chapter 3. It discusses the fundamental and dominant noise sources in the system that contribute towards the noise figure of the PT-symmetric systems. The chapter presents equivalent noise models of realistic PT-symmetric circuits in series and shunt configurations and then estimates the analytical noise figure of each aforementioned design configuration. In addition, it also presents the simulation validation of noise figure.

Chapter 5 discusses the potential design application of PT-symmetric circuits such as unidirectional or bidirectional cloaking and invisibility, radar cross-section reduction and electromagnetic switching. The chapter extends the analytical results from Chapter 3 and Chapter 4, and presents a full-wave electromagnetic model of a reconfigurable metasurface cloak based on PT-symmetry, in series and shunt design configurations. The proposed cloaking models can be configured to provide unidirectional or bidirectional structural transparency or invisibility through an imaginary impedance. The chapter then evaluates the performance of an ideal and realistic PT-symmetric metasurface cloak in the presence of various noise figure levels and then estimates the radar cross-section in each case. It further shows the design of an electromagnetic switch or an attenuator based on PT-symmetry.

Chapter 6 discusses the potential design techniques of a functional gain element in PT-symmetric circuits. It presents the realisation of a negative resistor through a tunnel diode and operational amplifier. It also discusses the performance degradation caused due to uncertainty in the magnitude of gain resistor. Finally, it presents further applications of a negative impedance converters.

Chapter 7 discusses, concludes and summarises the research studies performed in this thesis.

Chapter 2

Background Theory

2.1 Fundamentals of Wave Electromagnetics

Fundamental theoretical concepts of electromagnetics and PT-symmetry are the core foundation of the research work presented in this thesis. The chapter begins with the Maxwell's equations and then introduces the concept of parity symmetry, time-reversal symmetry and combined parity-time symmetry in electromagnetics. The chapter then describes the concept of negative impedance and the conversion circuits that enable the practical realisation of a parity-time symmetric system in microwave electronics. Further, the chapter includes fundamental concepts of the noise figure for basic circuit elements such as resistors, capacitors, inductors, diodes, transistors and operational amplifiers.

2.1.1 Time-Varying Maxwell's Equations

Maxwell's equations formulated by James C. Maxwell to describe the dynamics of the macroscopic electromagnetic phenomenon [38–39]. These equations resulted from the theoretical and experimental work done previously by Gauss, Ampere, Lenz, Faraday and various others [40–42]. They can be expressed in either integral or differential forms. The integral form of Maxwell's equations provide more understanding of underlying physics but they are usually solved analytically for canonical objects [43]. Modern computing advantages have made it possible to utilize the differential form of these equations to numerically compute the problems in both time and spatial domain with high precision.

Maxwell's curl equations in differential form are given as

$$\nabla \times \bar{H} = \bar{J}_e + \frac{\partial}{\partial t}\bar{D} \tag{2.1a}$$

$$\nabla \times \bar{E} = -\bar{M} - \frac{\partial}{\partial t}\bar{B} \tag{2.1b}$$

where the description of each quantity along with its units in an SI system has been given in table-1. All of these vector field quantities are real functions of time and spatial coordinates. For instance, electric field vector in Cartesian coordinates can be expressed as $\bar{E} = \bar{E}(x, y, z; t)$. Similar notation to be followed for other vector field quantities.

From Maxwell's curl equations described above, it can be followed that the generation of magnetic field $\bar{H}$ takes place in space due to time-varying electric flux density $\bar{D}$. Similarly, time-varying magnetic flux density $\bar{B}$ produces an electric field $\bar{E}$ provided that the space and time dynamics of magnetic and electric fields are coupled together. The coupling of these fields is related to the macroscopic response of the electric and magnetic property of the material which is also known as constitutive relations. Maxwell's constitutive equations in time-domain are given as [40, 44–45].

$$\bar{J}_e = \sigma(t) * \bar{E} \tag{2.2a}$$

$$\bar{D} = \varepsilon_0 \left(1 + \chi_e(t)\right) * \bar{E} \tag{2.2b}$$

$$\bar{B} = \mu \bar{H} \tag{2.2c}$$

where σ, ε_0, μ_0 and χ_e are material dependent electromagnetic properties which are stated in table-1 along with their units.

It is to be noted that * is the time domain convolution operator that is defined as

$$f(t) * \bar{E}(t) = \int_0^\infty f(\tau).\bar{E}(t-\tau)\,d\tau \tag{2.3}$$

Here in, $f(t)$ is the time-varying function of $\sigma(t)$ and $\chi_e(t)$.

Table-2.1. Electromagnetic quantities along with their symbols and units.

Symbol	Unit	Name
$\bar{E}$	V/m	Electric field vector
$\bar{D}$	C/m^2	Electric flux density vector
$\bar{H}$	A/m	Magnetic field vector
$\bar{B}$	Wb/m^2	Magnetic flux density vector
$\bar{J}$	A/m^2	Electric current density vector
$\bar{M}$	V/m^2	Magnetic current density vector
ε	F/m	Electric permittivity
μ	H/m	Magnetic permeability
σ	S/m	Electrical conductivity
χ_e	-	Dielectric susceptibility

2.1.2 Boundary Conditions

The time-varying curl equations described in (2.1.1) are only valid in a continuous medium. However, in the presence of material discontinuity, the solutions to Maxwell's equations can be described by appropriate boundary conditions that are dependent on the geometrical structure. The vector field response at an interface or a boundary between different materials is

described by Maxwell's divergence formulae for the time-varying field in a source-free region. These are expressed as follows [42].

$$\nabla.\bar{D} = 0 \tag{2.4a}$$

$$\nabla.\bar{B} = 0 \tag{2.4b}$$

Applying Gauss's law to Eq. (2.4a) at an interface or boundary of two different media whose electromagnetic properties are denoted by ε_1, μ_1 and ε_2, μ_2 as shown in figure Fig. 2.01, it can be concluded that the normal components of electric field density are not continuous and are given by mathematical expression as [42].

$$\bar{D}_{n1} = \bar{D}_{n2} \tag{2.5}$$

where $\bar{D}_n$ is the normal component of the electric field density.

Similarly, using Stoke's theorem it can be shown that the tangential components of the electric field are always continuous at the interface [40–42].

$$\bar{E}_{t1} = \bar{E}_{t2} \tag{2.6}$$

The boundary conditions for $\bar{B}$ and $\bar{H}$ can be obtained in a similar way and can be given as [40–42].

$$\bar{B}_{n1} = \bar{B}_{n2} \tag{2.7}$$

$$\bar{H}_{t1} = \bar{H}_{t2} \tag{2.8}$$

The boundary conditions described here are only valid in a source-free interface, therefore the surface current density and charge densities have been neglected. Fig. 2.01 shows the boundary conditions of electric and magnetic field quantities at the interface of the two different mediums.

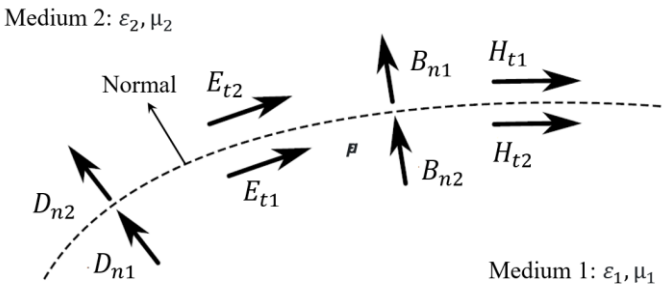

Fig. 2.01. Fields at a general interface between two different mediums.

2.2 Fundamentals of Parity-Time Symmetry

This section discusses the underlying concept of parity-symmetry, time-reversal symmetry and combined parity-time symmetry. In order to have better understanding, it is important to review fundamental postulates, concepts and definitions that lead to the realisation of PT-symmetry.

2.2.1 Parity-Reversal

The parity or mirror inversion involves the transformation of the coordinates such that they are reflected through a certain reference plane. Parity transformation flips the sign of an electric field components that are normal to the mirror plane however the transverse components remain unaffected. On the contrary, the magnetic field components that are normal to the plane remain unaffected however the transverse components get interchanged.

To have a physical insight of the parity phenomenon, we consider a case of a current carrying loop that produces a magnetic field which is perpendicular to the loop, given by the Ampere's law. The current vector of the current carrying loop is effected such that the components normal to the reflection plane change their sign but transverse components are

unaffected. This has been explained in Fig. 2.02 where the normal reflection has been shown and we may assume that the magnetic field will obey the same transformation rules. However, the application of Ampere's law on current carrying loop implies that this transformation is incorrect since the magnetic field is pointing in the wrong direction.

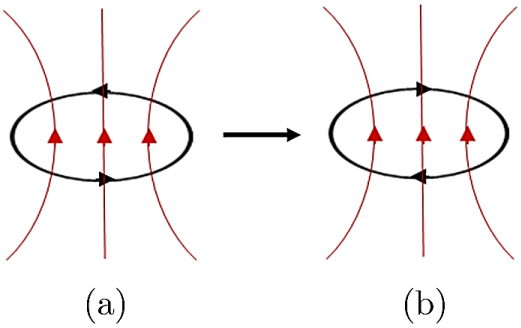

Fig. 2.02. (a) Transformation Current carrying loop, (b) Assumption of Magnetic field in wrong orientation after parity transformation.

The correct orientation of the magnetic field governed through Ampere's law after the transformation has been shown in Fig. 2.03. It is evident that the magnetic field must be transformed in a different manner, unlike the standard vectors under the parity transformation. This is because the electric field is a polar vector, whereas the magnetic field is an axial vector which is a cross product of polar vectors [46–47].

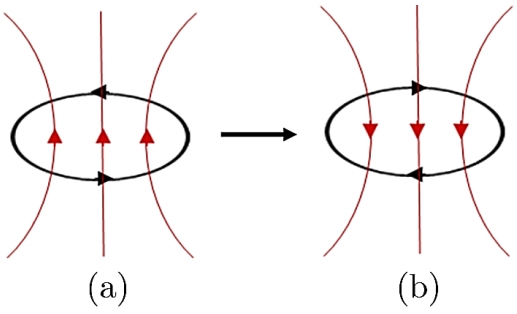

Fig. 2.03. (a) Transformation of current carrying loop. (b) Magnetic field transformation in accordance with Ampere's law in correct orientation after transformation.

In electronics circuits, parity inversion is related to the circuit topology and corresponding circuit elements interchange their coordinates such that

$$x \rightarrow -x \tag{2.9}$$

$$y \rightarrow -y \tag{2.10}$$

$$z \rightarrow -z \tag{2.11}$$

Therefore parity inversion is relatively simple in electronic circuits in comparison with spatial systems. For instance, consider the arbitrary circuit schematic shown in Fig. 2.04 which has been transformed using parity (P) operator. After the parity transformation, the circuit elements spatial coordinates get interchanged i.e. $R_1 \rightarrow R_3$ and $C_1 \rightarrow L_1$

It can be noticed that the element R_2 remains unchanged since it is located at the origin of transformation reference. The circuit discussed here does not obeys parity invariance.

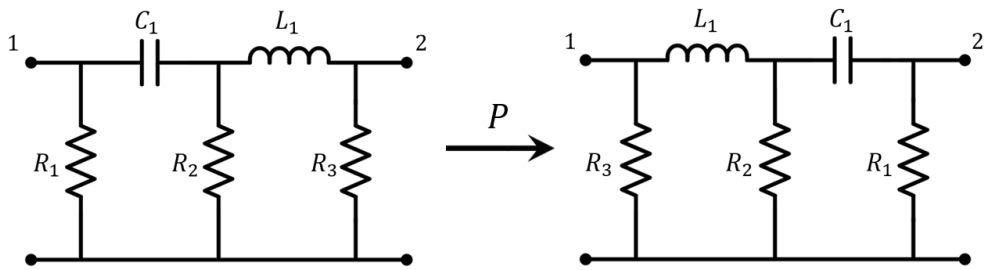

Fig. 2.04. Circuit transformation under Parity (P) operator.

2.2.2 Time-Reversal

Time reversal systems with time-reversal operator $t = -t$ would appear to run backwards in time. Time-reversal transformation does not affect spatial vectors but time dependent spatial quantities would get reversed in such that if the time would be running backwards, for instance electric current,

magnetic field, velocity and more. According to Maxwell equation curl equation [47].

$$\nabla \times \bar{H} = \frac{\partial \bar{D}}{\partial t} + \bar{J} \tag{2.12}$$

Time-reversal transformation implies that the time-variance with respect to the reference is negative such that $\Delta t = -t$ therefore $\frac{\partial}{\partial t} \to -\frac{\partial}{\partial t}$ and $\bar{J} = -\bar{J}$. The magnetic field is also time dependent hence it implies that $\bar{H} = -\bar{H}$. Therefore after time-reversal transformation, we get

$$\nabla \times (-\bar{H}) = -\frac{\partial \bar{D}}{\partial t} - \bar{J} \tag{2.13}$$

In other words, reversing the current vector also reverses the magnetic field vector. Similarly other field quantities transformation under time-reversal operation would be transformed such that $\Delta t = -t$.

$$\bar{E}(r,t) \to \bar{E}(r,-t) \tag{2.14a}$$

$$\bar{D}(r,t) \to \bar{D}(r,-t) \tag{2.14b}$$

$$\bar{J}(r,t) \to -\bar{J}(r,-t) \tag{2.14c}$$

$$\bar{H}(r,t) \to -\bar{H}(r,-t) \tag{2.14d}$$

$$\bar{B}(r,t) \to -\bar{B}(r,-t) \tag{2.14e}$$

Similarly, the constitutive parameter would be transformed under time-reversal by replacing the time invariance as negative such that $\Delta t = -t$.

$$\varepsilon(r,t) \to \varepsilon(r,-t) \tag{2.15}$$

$$\mu(r,t) \to \mu(r,-t) \tag{2.16}$$

Frequency and time-varying parameters are related to each other by Fourier transform which implies that a variable $F(r,\omega)$ which undergoes a transformation of $t \to -t$ would essentially be equivalent to $F^*(r,\omega)$. Hence, in the frequency domain, we have following relationship [48–49].

$$\bar{E}(r,\omega) \to \bar{E}^*(r,\omega) \tag{2.17a}$$

$$\bar{J}(r,\omega) \to \bar{J}^*(r,\omega) \tag{2.17b}$$

$$\bar{H}(r,\omega) \to \bar{H}^*(r,\omega) \tag{2.17c}$$

Time reversal in electronics effectively reverses the sign of resistive impedances whereas the reactive impedances remains unchanged [50].

$$R \overset{-t}{\to} -R \tag{2.18}$$

$$C \overset{-t}{\to} C \tag{2.19}$$

$$L \overset{-t}{\to} L \tag{2.20}$$

We can take a simple example of Ohm's law, for instance, we have

$$V(t) = I(t).R \tag{2.21}$$

The flow of charge is a time dependent quantity and it can be expressed as dQ/dt which would resultantly give current. In a time-reversal transformation, it the current can be written as

where

$$dQ / d(-t) = -dQ / dt \tag{2.22}$$

This further implies that

$$dQ / dt = -I \tag{2.23}$$

Or in a simple notation we can write Eq. (2.21) after time-reversal transformation as

$$V = -IR \tag{2.24}$$

The current in the conventional positive resistor in forward time corresponds to energy dissipation. However, after time-reversal transformation it would imply that that the current direction is reversed which means that energy is being drawn from the resistor. In electronic circuits, such a resistor is known as negative resistor which is realised by the means of negative impedance converters (NIC).

2.2.3 Parity and Time-Reversal Symmetry

Parity-time (PT) symmetry was originally presented in quantum mechanics, hence it is important to review basic fundamental definitions that lead to the understanding of PT-symmetry.

In quantum mechanics, Hamiltonian (H) operator describes the total energy of a particle in the system as a function of its position and momentum [51–52].

$$\hat{H} = \hat{p}^2 + \bar{V}(x) \tag{2.25}$$

Here, $\hat{p}$ denotes the linear momentum and $\bar{V}$ describes the potential energy function. It follows that if the potential function $\bar{V}(x)$ is a real function in space, then the energy of the Hamiltonian is real and measurable. In other words, if the Hamiltonian $\hat{H}$ is Hermitian $H^{\dagger}$, the energy states associated with the Hamiltonian are also real.

$$\hat{H} = H^{\dagger} \tag{2.26}$$

where the Hermitian is an adjoint matrix operator which corresponds to the transpose and complex conjugation.

Bender and Boetcher showed in [3–4] that although Hermiticity sufficiently describes all the possible energy states, is not the only condition for a Hamiltonian to have real energy. Further it was shown that a weaker condition can enable the Hamiltonian to possess real energy function, which is Parity-Time (PT) symmetry [3–6] and such a Hamiltonian would be invariant under combined PT transformation.

$$PT\left(\hat{H}\right)TP = \hat{H} \tag{2.27}$$

where P is the Parity operator that interchanges the spatial position and T is time-reversal operator that inverts the time.

Systems that are invariant under combined Parity-Time (PT) symmetry are regarded at PT-symmetric systems. For instance, consider the Fig. 2.05 shown where loss and gain are coupled together. Since parity-transformation corresponds to the interchange of spatial coordinates, loss and gain are interchanged. Similarly, time-reversal corresponds to the state of the system as if the time would be running backwards, therefore the system regains its original state after the combined transformation of parity and time-reversal operations.

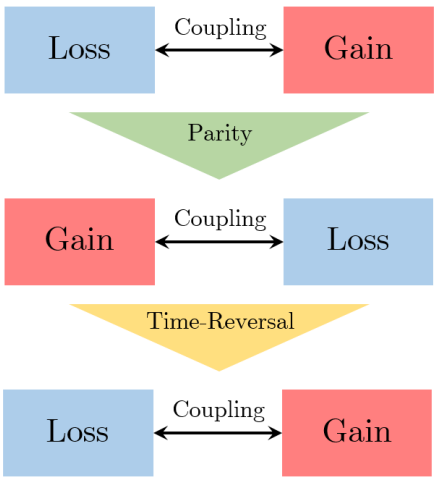

Fig. 2.05. Combined PT-symmetry transformation on a system with loss and gain coupled together with a coupling mechanism.

2.2.4 PT-Symmetry in Microwave Electronics

A PT-symmetric system can be realised through a combination of loss and gain that are coupled together through a coupling mechanism. In electronics and electromagnetics circuits, the coupling may correspond to a simple transmission line combing gain and loss, or in a complex domain may correspond to a mutually coupled inductive transformer.

In electronics, electromagnetics and RF circuits, loss and gain elements can be realised as positive and negative impedances that can be incorporated in series/shunt configurations with satisfied parity and time-reversal conditions. For instance, a parity operator switches the spatial coordinates of both impedances, and time-reversal operator will interchange positive impedance (loss) and negative impedance (gain). Under the combined transformation of parity and time-reversal operations, if a circuit remains invariant then it would be regarded as PT-symmetric circuit.

According to PT-postulates described in (2.2.4), the PT-symmetric system must only be invariant under combined parity and time-reversal operations but should not be invariant under individual parity or time-reversal transformations [50, 53]. Fig. 2.06 shows a simple circuit where two lumped impedances Z_1 and Z_2 are connected together through a transmission line of length kd in series configuration.
The two impedances are modelled such that Z_1 is positive and Z_2 is negative, to respectively incorporate loss and gain in the system. Under the parity (P) transformation the two impedances swap their spatial coordinates such that $x \rightarrow -x$, $y \rightarrow -y$ and $z \rightarrow -z$ [32]. Therefore, after a parity-transformation, the impedances Z_1 and Z_2 interchange their respective coordinates as shown in Fig. 2.06.

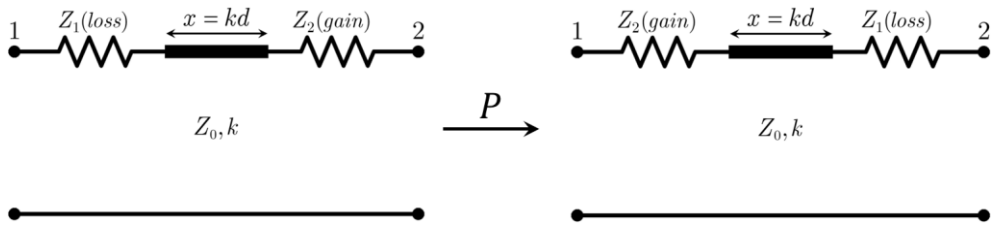

Fig. 2.06. A simple electronic circuit under parity-reversal operation with loss and gain impedances connected together through a transmission line.

Applying time-reversal operation on the parity-reversed system would change the signs of the resistive impedances, however the imaginary part of the impedances do not change. Applying time-reversal operation on the parity-reversed circuit shown in Fig. 2.07 will correspond that the gain impedance Z_2 becomes loss and the loss impedance Z_1 gets transformed into gain. Therefore under combined parity and time-reversal operations the circuit reinstates its original form. Hence, it can be concluded that the circuit shown is PT-symmetric because it is invariant under combined parity and time-reversal operations. To have a physical insight of the reflection and transmission behaviour, the subsequent section discusses the scattering matrix notation and scattering properties of the PT-symmetric system.

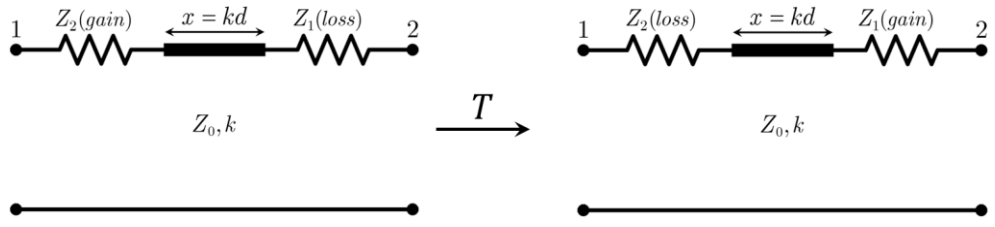

Fig. 2.07. The circuit shown in Fig. 2.06 undergoing a time-reversal operation. The resistive impedances flip their signs under time-reversal operation. The circuit is PT-symmetric because it is invariant after the combined transformation of parity and time-reversal.

2.2.5 Scattering Matrix of a PT-Symmetric System

In microwave engineering scenarios, it is convenient to express the system reflection and transmission properties in terms of its scattering parameters. Consider Fig. 2.08 where the schematic of a two-port microwave network has been shown. The incoming and outgoing waves at port-1 are represented by a_1 and b_1 respectively. Similarly, incoming and outgoing waves at port-2 are described by a_2 and b_2 respectively.

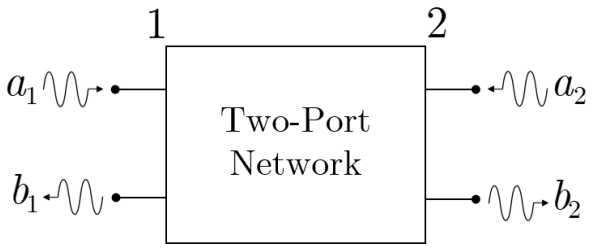

Fig. 2.08. Schematic illustration of a two-port microwave scattering system.

Following the scattering matrix formulism for a two-port microwave network described in [46], the scattering properties can be written as

$$\begin{pmatrix} b_1 \\ b_2 \end{pmatrix} = S \begin{pmatrix} a_1 \\ a_2 \end{pmatrix} \tag{2.28}$$

where

$$S = \begin{pmatrix} S_{11} & S_{12} \\ S_{21} & S_{22} \end{pmatrix} \tag{2.29}$$

The transfer matrix (T) relating the incident and reflected waves can be constructed as

$$\begin{pmatrix} a_1 \\ b_1 \end{pmatrix} = M \begin{pmatrix} b_2 \\ a_2 \end{pmatrix} \tag{2.30}$$

where

$$M = \begin{pmatrix} \frac{1}{S_{21}} & -\frac{S_{22}}{S_{21}} \\ \frac{S_{11}}{S_{21}} & S_{12} - \frac{S_{11}S_{22}}{S_{21}} \end{pmatrix} \tag{2.31}$$

We assume that the network is invariant under combined transformation of parity and time-reversal operations and hence is PT-symmetric. Therefore, the system described in Fig. 2.08 can be redrawn after PT transformation as shown in Fig. 2.09.

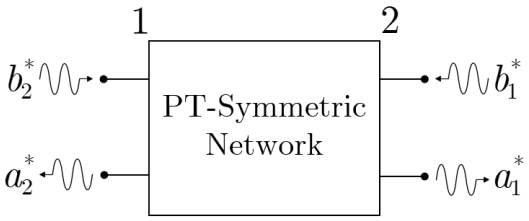

Fig. 2.09. The two-port microwave scattering system after PT-transformation.

The transfer matrix of the PT-symmetric system can now be constructed as

$$\begin{pmatrix} b_2^* \\ a_2^* \end{pmatrix} = M^{PT} \begin{pmatrix} a_1^* \\ b_1^* \end{pmatrix} \tag{2.32}$$

Comparing Eqs. (2.31) and (2.32) for before and after PT-transformation yields [54–57].

$$M \overset{PT}{\rightarrow} M^{PT} = M^{-1^*} \tag{2.33}$$

If the PT-symmetric is reciprocal then the forward and reverse transmission are equal i.e. $M_{12} = M_{21}$ and by following Eq. (2.33) we can write

$$|M| = 1$$

Using above expression it can be followed that [54]

$$M_{11} = M_{22}^{*}$$

Using these relationships, the transmission matrix in Eqs. (2.31) can be parametrised as

$$M = \begin{pmatrix} A & -jB \\ jC & A* \end{pmatrix} \tag{2.34}$$

where B and C are transmission coefficients and are always real numbers.

The each parameter in the transmission matrix can be expressed in terms of scattering parameters as

$$A = \frac{1}{S_{21}} \tag{2.35}$$

$$B = -j\frac{S_{22}}{S_{21}} \tag{2.36}$$

$$C = j\frac{S_{11}}{S_{21}} \tag{2.37}$$

$$A^{*} = S_{12} - \frac{S_{11}S_{22}}{S_{21}} \tag{2.38}$$

The determinant of a transmission matrix for a PT-symmetric system has a value equal to unity. Using this exploitation on Eq. (2.34) yields

$$|M| = 1 = \begin{vmatrix} A & -jB \\ jC & A^{*} \end{vmatrix} \tag{2.39}$$

Solving Eq. (2.39) and substitution from Eqs. (2.35)–(2.38) further yields following expression [54-57]

$$1 - |S_{21}|^{2} = S_{11}S_{22}^{*} \tag{2.40}$$

From Eq. (2.40) it is evident that when the transmission becomes unitary, the product $S_{11}S_{22}^{*}$ must be zero, which further leads to the conclusion that

one of the reflection coefficients from either input ports must be equal to zero [54–57].

To have a further insight of this exciting phenomenon, consider the schematic of the circuit from section 2.2.4 in Fig. 2.10 where a two-port PT-symmetric system has been shown with incident and reflected waves. The two lumped resistors have been connected together through a transmission line of length kd. In order to satisfy PT-symmetric conditions, the two resistors are defined such that their magnitudes are opposite to each other corresponding to loss and gain. A dimensionless non-Hermiticity parameter r is introduced to define the resistors in terms of characteristic line impedance such that $R_1 = rZ_0$ and $R_2 = -rZ_0$.

It is to be noted that a lossy resistor is a conventional positive resistor (loss) drawing energy from an electronic circuit. Whereas, to have time-reversal symmetry, negative resistor (gain) is employed in the system which provides energy to the system. For the purpose of brevity, we have chosen ideal lumped models of both resistances.

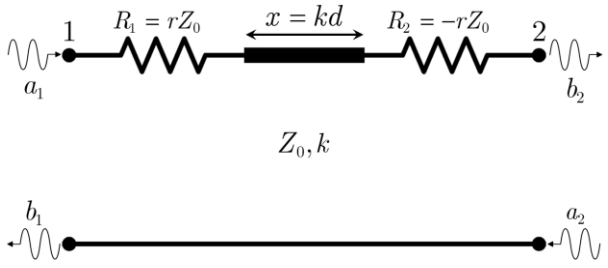

Fig. 2.10. Schematic of the two-port PT-symmetric system modelled as two lumped resistors with a transmission line such that $R_1 = rZ_0$ and $R_2 = -rZ_0$.

The point of interest is to define the PT-symmetric system in terms of its reflection and transmission properties or scattering parameters. The

scattering parameters are found by cascading the transmission or ABCD matrix of each individual element by following [46] as

$$S = \begin{pmatrix} \dfrac{ir\sin x(-r+2)}{2\cos x + i\sin x(-r^2+2)} & \dfrac{2}{2\cos x + i\sin x(-r^2+2)} \\ \dfrac{2}{2\cos x + i\sin x(-r^2+2)} & \dfrac{ir\sin x(-r-2)}{2\cos x + i\sin x(-r^2+2)} \end{pmatrix} \tag{2.41}$$

Such a matrix satisfies the PT-symmetric condition $PTS(\omega^*)PT = S^{-1}(\omega)$ [55]. Further discussion of unitary transmission and zero reflection coefficient has been performed in the subsequent sections where the application of PT-symmetric exceptional points have been discussed for unidirectional reflectionless transmission.

2.2.6 Exceptional Points of PT-Symmetric Systems

The relationship between incident, transmitted and reflected waves is well described by the scattering matrix notation. The formulism has been previously discussed for PT-symmetric systems in section 2.2.5. This section will focus on the investigation of the spectral properties of the scattering matrix of PT-symmetric system described earlier in Fig. 2.10.

For a linear passive system with no loss and gain, the scattering matrix is given as unitary [58].

$$S^{\dagger} = S^{-1} \tag{2.42}$$

where $\dagger$ denotes transpose and complex conjugation operation.
This also implies that the eigenvalues of a linear, passive system are unimodular i.e.

$$|\lambda| = 1 \tag{2.43}$$

Therefore, the power of a linear and passive system is conserved with no net amplification or dissipation which can be conveniently regarded as the law of energy conservation.

Since PT-symmetric systems employ loss and gain, the spectral behaviour is non-trivial and the system may undergo a phase transition i.e. from a power conservation phase to non-power conversation phase. This phase transition of PT-symmetric system can be manipulated through loss and gain proportions. The point at which the phase transition of PT-symmetric systems occur are known as exceptional points (EP) and because the transition is unique, EP have been studied to provide reflectionless transmission, unidirectional cloaking and invisibility, lasing and more.

For convenience, the scattering parameters of the schematic shown in Fig. 2.10 have been given as follows

$$S_{11} = \frac{ir\sin x(-r+2)}{2\cos x + i\sin x(-r^2+2)}$$

$$S_{12} = S_{21} = \frac{2}{2\cos x + i\sin x(-r^2+2)}$$

$$S_{22} = \frac{ir\sin x(-r-2)}{2\cos x + i\sin x(-r^2+2)}$$

It can be readily concluded that the system exceptional point is located at $r = 2$, because the substitution would yield a zero input reflection coefficient regardless of the electrical line length. Using an arbitrary frequency the magnitude of scattering parameters at the exceptional point are given as

$$S = \begin{pmatrix} 0 & 1 \\ 1 & 4 \end{pmatrix} \tag{2.44}$$

It can be noticed that the transmission coefficients are unitary and equal due to reciprocity and by following Eq. (2.44) we can verify that reflection coefficient at port-1 has indeed vanished at exceptional point. However, the reflection coefficient seen at port-2 is non-zero and is higher than unity which describes that an impinging wave at port-2 would experience a very strong output reflection coefficient due to the gain resistor.

To have further understanding and to verify the analytical results of the PT-symmetric circuit described earlier, we have carried out a lumped circuit element model simulation in a commercially available RF circuit simulator. The schematic has been shown in Fig. 2.11 followed by the simulated scattering parameters plot in Fig. 2.12.

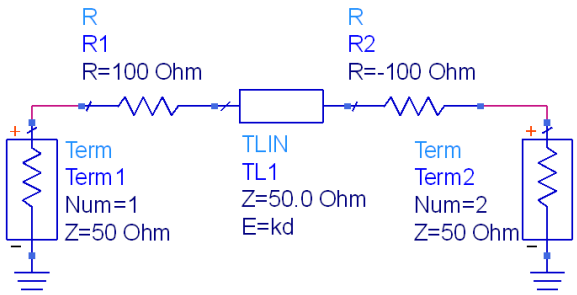

Fig. 2.11. Circuit simulation setup in Keysight ADS. The two resistors are chosen such that their impedance is twice to that of the characteristic line impedance to reach the exceptional point.

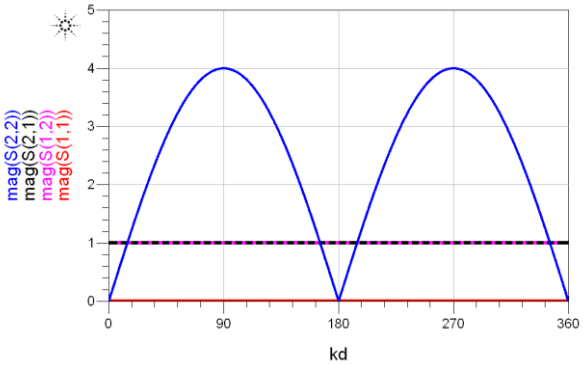

Fig. 2.12. Simulated s-parameter plot of the PT-symmetric circuit.

The simulated circuit model confirm the analytical results described in Eq. (2.44). The transmission line model shows that the reflection coefficient at port-1 vanishes at the exceptional point at $r = 2$. While the transmission towards port-2 is unity, the output reflection is calculated to be four times. This is because the wave entering from port–2 faces the active element $R_2 = -rZ_0$ and hence experiences enhanced reflection.

From a practical design and implementation perspective, it is to be noted that the reflection and transmission coefficients in the aforementioned system are fixed at the exceptional point and cannot be manipulated in any fabricated PT-symmetric circuit. Therefore, the design of a PT-symmetric circuit with the ability of reflection and transmission manipulation is essential. For this purpose, more detailed discussion has been performed in Chapter 3.

2.2.7 Negative Refraction Using PT-Symmetric Metasurfaces

The scattering parameters of the PT-symmetric system described in Fig. 2.11 show that the transmitted wave to port-2 undergoes phase advance equal to the electrical line length, a property which has been studied in [25, 59] for negative refraction and super-lensing. The phase advance of the wave is caused due to the backward phase velocity, maintained by the active metasurface and directed towards the passive metasurface. By examining the scattering parameters, we find that this is indeed the case. The scattering parameters at an exceptional point of $r = 2$ are given as follows which show that the incident wave is fully transmitted through the structure with a phase advance equal to $+x$.

$$S = \begin{pmatrix} 0 & e^{+ix} \\ e^{+ix} & 4\sin^2(x) - 2i\sin(2x) \end{pmatrix}$$

To have a further insight to this phenomenon, we have performed full-wave electromagnetic simulations using COMSOL Multiphysics RF module in frequency domain for the schematic shown in Fig. 2.11 with loss and gain metasurfaces separated by a simple transmission line.

The simulation setup for the full-wave model has been shown in Fig. 2.13 where a plane wave with an amplitude of 1 V/m is incident from port-1 at the pair of loss and gain metasurfaces. The equivalent lumped element circuit schematic has been shown in Fig. 2.11. The loss and gain resistors are given as

$$R_1 = +2Z_0$$

$$R_2 = -2Z_0$$

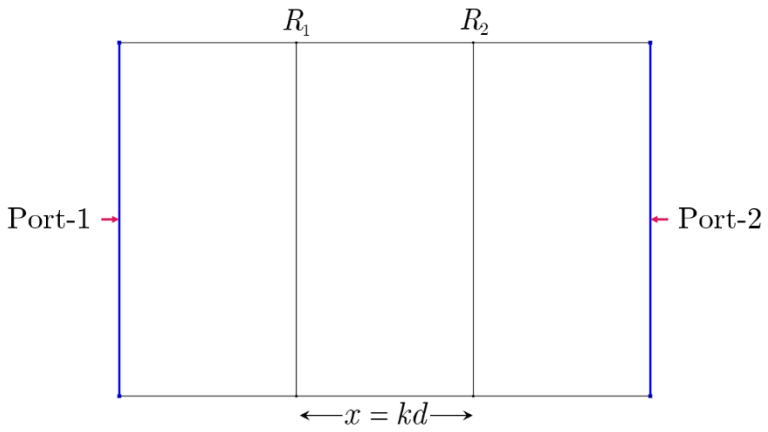

Fig. 2.13. Equivalent full-wave electromagnetic simulation setup for the schematic shown in Fig. 2.11. The lumped resistors with loss and gain are modelled as an ultrathin metasurface with loss and gain respectively.

Fig. 2.14 shows the time-snapshot of the z-component of the incident electromagnetic wave on the metasurface pair undergoing negative refraction. The power flow is represented by the black Poynting vectors.

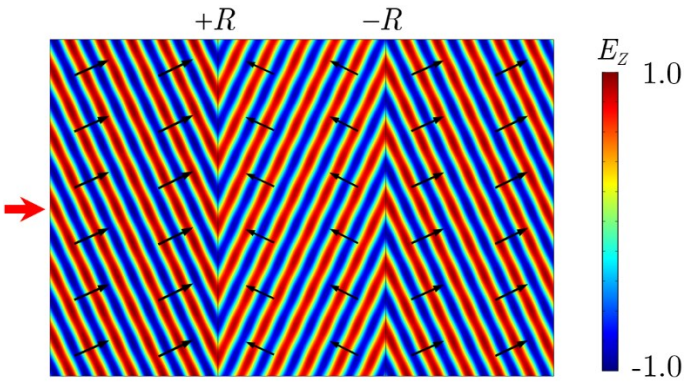

Fig. 2.14. Time snapshot of a plane wave incident at 30 degrees on PT-symmetric metasurfaces with loss and gain respectively. The backward power flow is sustained by the active metasurface on the right.

Similar phenomenon is noticed for an incident Gaussian beam at loss and gain metasurface pair which has been shown in Fig. 2.15.

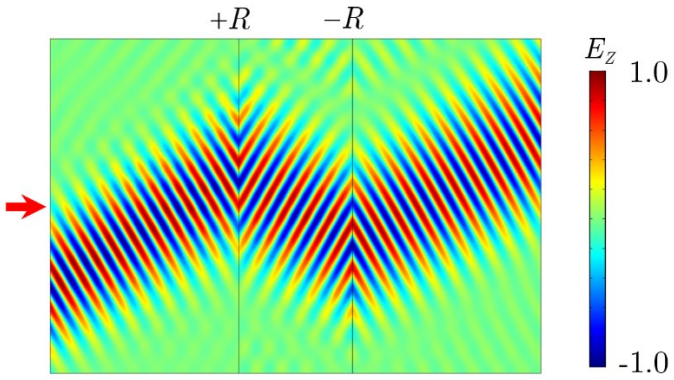

Fig. 2.15. Time snapshot of a Gaussian wave incident at an angle of 30 degrees on PT-symmetric metasurface undergoing negative refraction. The backward power flow is being sustained by the active metasurface on the right.

It is also to be noted that the simulations have been performed in an ideal and loss-free domains where the system losses and fundamental noise sources have not been considered.

2.2.8 Realisation of Gain in PT-Symmetric Circuits

We have described in earlier sections that the PT-symmetric systems are composed of loss and gain elements that are coupled together by some coupling mechanism. In electronic and microwave circuits, the realisation of loss element simply corresponds to a conventional positive resistance in which is also a power sink, attenuation or a loss element. The gain element is chosen such that it satisfies parity and time-reversal conditions described in section 2.2.1, 2.2.2 and 2.2.4. Therefore, an element satisfying parity and time-reversal operators is a negative resistance which does not occurs as a standalone circuit element however can be artificially engineered by the means of negative impedance converters (NIC) and hence requires further attention. One may suggest an amplifier as a potential gain element since PT-symmetry is composed of equal proportions of loss and gain. It must be noted that the parity and time-reversal operations are not applicable to amplifiers due to the reasons that they are unilateral devices which provide gain in a single direction only. Further, the time-reversal operations are performed only on resistive impedances as studied in [13–14]. Therefore, positive and negative impedances are the most appropriate loss and gain elements in designing and implementing PT-symmetric systems.

Negative resistance is an uncommon property that occurs in a limited number of non-linear electronic components such as in tunnel diodes, Gunn diodes or by the means of a negative impedance converters. The negative resistance means that the slope of the voltage-current $\Delta V \,/\, \Delta I$ is less than

zero or negative. A negative impedance converter is an active two-port device which takes the DC power applied to it and utilizes it to amplify the input AC signal at a particular frequency. In microwave engineering, this process is usually performed using bias-tee which combines the input AC and DC signals at input and output device terminals. In a negative resistance region, the current decreases as the voltage is increased resulting in a behaviour known as a negative differential region. For instance, a tunnel diode can be biased at a specific voltage to operate in the negative differential region and an AC signal at the input port can be seen inverted at the output. Due to high non-linearity, negative resistance rapidly varies with respect to the biasing voltage and hence the negative differential region can only be viewed over a limited range. Unlike conventional resistors providing positive resistance at all current ranges, negative resistance is realized through active components and circuitry such as transistors, operational amplifiers or through negative differential diodes. These are based on voltage or current inversion techniques resulting in an overall negative current-voltage slope. The upcoming section discusses the design approaches to realize negative resistance through a negative impedance converter.

2.2.9 Design Approaches for Negative Impedance Converters

The concept and design of a negative impedance conversion circuit was first proposed in 1950 which was composed of vacuum tubes and BJTs [60–61]. The primary purposed of these NICs was to provide resistive gain to overcome the losses in telephone lines. In 1953, Linvill presented voltage inversion based NIC design which was composed of cross coupled

transistors. Because of non-ideal behaviour the performance of these NICs was poor and a compensation network was required which was proposed by Larkey [62]. Larkey also defined the ideal negative impedance converter as an active two-port device whose impedance present at port-1 is exactly negative of that of port-2. Until late 1960, the concept of NIC was well-known in engineering and electronic applications however, the usability was primarily restricted due to the instability, primarily at high frequency ranges. NICs are able to invert real and imaginary impedances such that

$$R \rightarrow -R$$

$$L \rightarrow -L$$

$$C \rightarrow -C$$

Negative impedances can be realised for interesting applications in communication and RF microwave electronics. For instance, electrically small antennas are a solution to the constraints of space limitation but at a reduced size, they exhibit high reactance and small radiation resistance hence possessing poor gain, low bandwidth and limited efficiency. Conventional antenna matching techniques usually employ an inductor to cancel the reactance of ESAs but only at a single frequency. On the contrary, a negative capacitor implemented through NIC can cancel the capacitive reactance of a small antenna over broadband frequency range, effectively bypassing the fundamental gain-bandwidth limitations with a smaller size. A more detailed discussion of NIC based ESA have been performed in section-6.3. At present, the design and implementation of a stable NIC at microwave frequency ranges is challenging and hence fundamental design concepts have been discussed in this section.

The NIC design is primarily categorized into voltage or current inversion techniques. The voltage inversion NICs are primarily designed using BJTs and operate by inverting the voltage to realize a negative impedance. Similarly, a current inversion NIC consists of op-amps that invert the current to realize negative impedance. Another approach to realize negative impedance is through a resonant tunnel diode (RTD). Typically at low-frequency ranges op-amp or transistor based NIC is suitable whereas RTD enables the NIC design at frequency ranges up to THz. RTD based design approach enables the low profile and wide operating frequency range of NIC. The aforementioned design techniques to realize negative impedance have been discussed in this section.

a) BJT Based NIC

The transistor based NIC design was proposed by Linvill [60] for current and voltage inversion to provide negative impedance across the terminals. Linvill's design is composed of two cross-coupled BJTs such that their emitter terminals are connected with the input port whereas the collector terminals are connected with the output port or load as shown in Fig. 2.16.

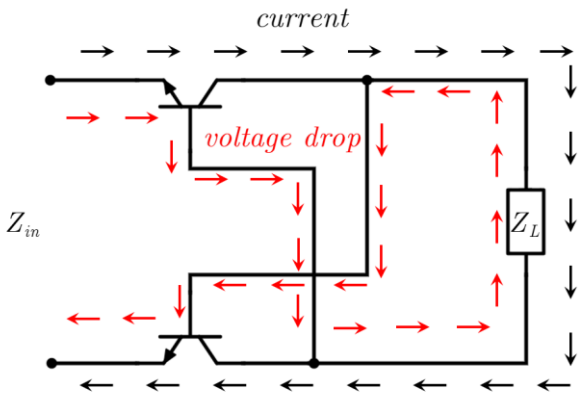

Fig. 2.16. Equivalent voltage-current relationship diagram for Linvill's NIC.

The collector current of first transistor is fed to the base of the second and vice versa. This configuration has been known as open-circuit model however, other configurations such as short-circuit model are also defined in which collector and emitter terminals of the BJT's are connected with input and output load respectively. The biasing network for the circuit is designed by using dc blocking capacitors such that it remains isolated from the RF input-output path to avoid interference. In theory, all of the current flows to the collector and then gets cross-coupled back to the transistor base terminal resulting in a voltage inversion across the load. The Linvill's open circuit schematic has been shown in Fig. 2.17.

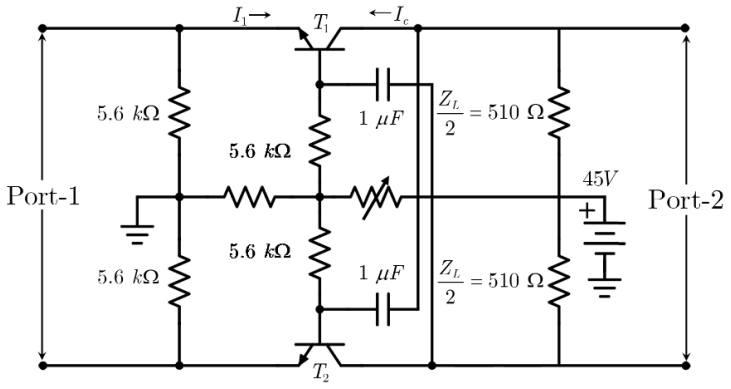

Fig. 2.17. Linvill's open-circuit stable NIC design based on cross-coupled BJTs with port-1 as input and port-2 as output/load.

The low resistance present at the emitter base causes the majority of the current to flow through the collector. The current I_1 is then cross-coupled back towards the base of the transistor causing the voltage inversion across the load. The variable resistor enables to achieve the stability of the biasing point at a required negative impedance.

The schematic shown in Fig. 2.17 can be redrawn with the equivalent T circuit models of the two transistors with their emitter, base and collector resistances as r_e, r_b and r_c respectively. The large current gain α is the ratio of the collector and the emitter currents whereas the collector terminal

is modelled as a parallel combination of the current source and collector resistance. The biasing current impedance and the DC blocking capacitors are represented as Z_g and Z_d respectively. With the redrawn schematic with equivalent circuit models shown in Fig. 2.18, we can write the junction voltages as

$$V_b = V_a - I_1 r_e \tag{2.45a}$$

$$V_c = V_b - (1-\alpha) I_1 r_b \tag{2.45b}$$

$$V_d = I_1 r_e + (1-\alpha) I_1 r_b \tag{2.45c}$$

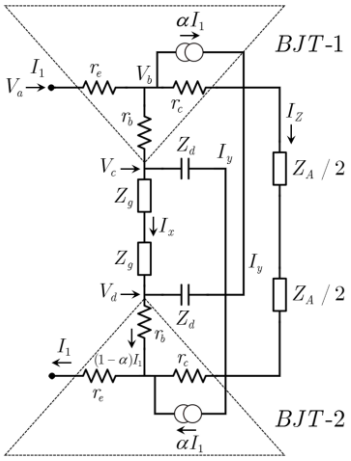

Fig. 2.18. Equivalent circuit model of Linvill's open circuit stable negative impedance converter.

The current I_x can be calculated through the potential difference between the terminal voltages V_c and V_d across the impedance Z_g.

$$I_x = \frac{V_c - V_d}{2Z_g} \tag{2.46}$$

Substituting the values of V_c and V_d from Eq. (2.45b) and Eq. (2.45c) yields

$$I_x = \frac{V_a - 2I_1 r_e - 2(1-\alpha) I_1 r_b}{2Z_g} \tag{2.47a}$$

The current through the feedback path are given as

$$I_y = (1-\alpha)I_1 - I_x \tag{2.47b}$$

$$I_z = \alpha I_1 - I_y \tag{2.47c}$$

Substution of Eq. (2.47a) into Eq. (2.47b) and solving

$$I_y = (1-\alpha)I_1 - \frac{V_a - 2I_1 r_e - 2(1-\alpha)I_1 r_b}{2Z_g} \tag{2.48a}$$

$$I_z = (2\alpha - 1)I_1 + \frac{V_a - 2I_1 r_e - 2(1-\alpha)I_1 r_b}{2Z_g} \tag{2.48b}$$

Another way to calculating I_z is by applying Kirchhoff's voltage law on the loop as

$$I_z = \frac{V_d + I_y Z_d - (V_c - I_y Z_d)}{Z_A} \tag{2.48c}$$

Comparing Eqs. (2.48b) and (2.48c) for I_z and substitution of I_y from (2.48a) can yield the impedance seen at the input terminals as

$$Z_{in} = 2r_e + (1-\alpha)\left(2r_b + \frac{2Z_g(2Z_d + Z_A)}{2Z_g + 2Z_d + Z_A}\right) - \alpha Z_P \frac{Z_g}{Z_g + Z_d} \tag{2.49}$$

where Z_P is the parallel equivalent of Z_A and $2(Z_g + Z_d)$. Also it can be noticed that the capacitor acts as a short circuit at high frequencies with a negligible impedance close to zero. The Eq. (2.49) can be simplified a

$$Z_{in} = 2r_e + (1-\alpha)2r_b + (1-2\alpha)Z_P \tag{2.50}$$

It is noticed that the transistor current gain α is frequency dependent and is given as

$$\alpha = \frac{\alpha_0}{1 + \frac{jf}{f_c}} \tag{2.51}$$

It can be followed from Fig. 2.19 that the transistor with a high cut-off frequency f_c, would result in a flat negative impedance, therefore the transistor choice in designing negative impedance circuits is critical. Fig.

2.19 shows the cut off frequencies of various transistors. For instance, a transistor with a cut of frequency of 10 GHz would provide a negative impedance circuit operation at a frequency of up to 1 GHz which is $1/10^{th}$ of the cut-off frequency.

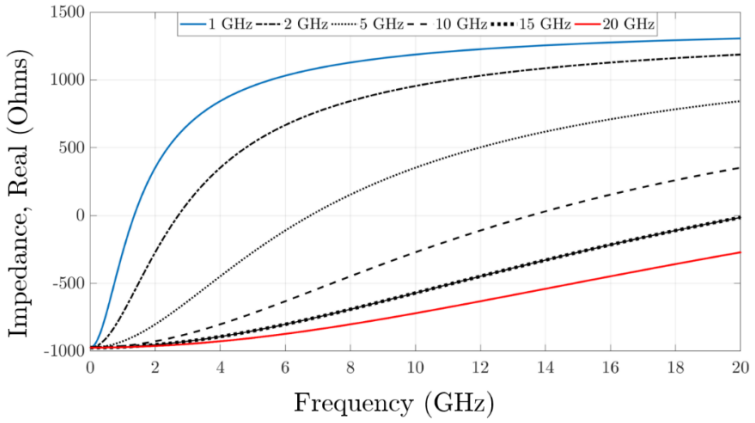

Fig. 2.19. Input impedance plot of various transistor's cut-off frequency. A flat negative impedance is achieved using transistors with high cut-off frequency levels.

A BJT based NIC works on the principle of voltage inversion, whereas the current remains unchanged and since the loop gain and bandwidth product is constant, the BJT based NIC design can allow a smaller bandwidth for a UHF and VHF frequency operation. However, the downfall comes in the form of uncertainty in defining the poles and zeroes of the NIC circuit which results in instability and difficulty of implementation.

b) Operational-Amplifier Based NIC

In the previous section, the voltage inversion NIC approach was discussed using Linvill's BJT design for open circuit stable design. Another approach to realize a negative impedance circuit is by the means of current inversion which is performed by using operational amplifiers (op-amp). The primary advantage of using this approach is stability because the poles and zeroes

of the NIC system are defined much precisely as compared to the transistor based design. Further, operational amplifiers are readily available as surface mount chip packages that are more immune to parasitic losses and hence offer better stability. However, the design flexibility using operational amplifiers is limited due to the package solution and positive feedback loop which also limits the operational bandwidth of the NIC. The schematic of an op-amp based NIC has been shown in Fig. 2.20.

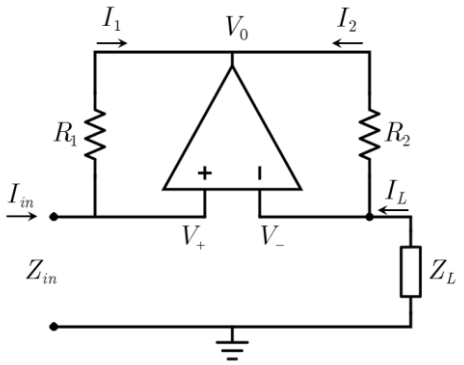

Fig. 2.20. Op-Amp based current inversion NIC circuit.

Since the op-amp based approach is based on the principle of current inversion. The node equation is given as

$$V_+ = V_- = I_L Z_L \tag{2.52}$$

The currents through the resistors R_1, R_2 are given as

$$I_1 = \frac{V_+ - V_0}{R_1} \tag{2.53a}$$

$$I_2 = \frac{V_- - V_0}{R_2} = \frac{I_1 R_1}{R_2} \tag{2.53b}$$

The input current relationship can be written as

$$I_{in} = I_1 = \frac{I_2 R_2}{R_1} \tag{2.54a}$$

Substituting the value of I_2 from (2.53b) yields

$$I_{in} = -\frac{I_L R_2}{R_1} \tag{2.54b}$$

Substituting the values of V_{in} and I_{in} from Eq. (2.52) and Eq. (2.54b) yields the input impedance as

$$Z_{in} = \frac{V_{in}}{I_{in}} = -\frac{R_1}{R_2} Z_L \tag{2.55}$$

The negative impedance achieved in this op-amp circuit is due to the inverted current through the load Z_L. A breadboard based design for the current inversion was implemented at 10 MHz frequency and analysed through an oscilloscope. The input and output voltage plot have been shown in Fig. 2.21.

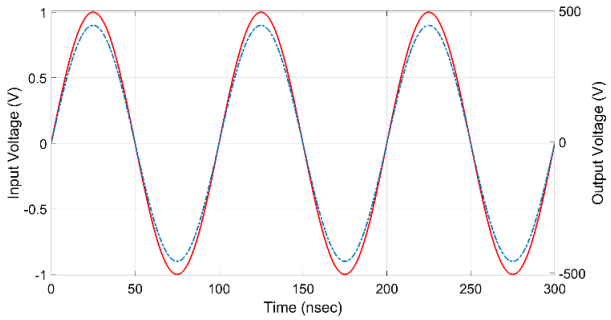

Fig. 2.21. Input voltage measurement across op-amp with a load of1000 Ω at 10 MHz.

The operational bandwidth is very limited in this case which restricts the usability of op-amps at higher frequency ranges. Fig. 2.22 shows the output voltage measurement and it can be seen that the current waveform went under inversion with a phase change of 180 degrees.

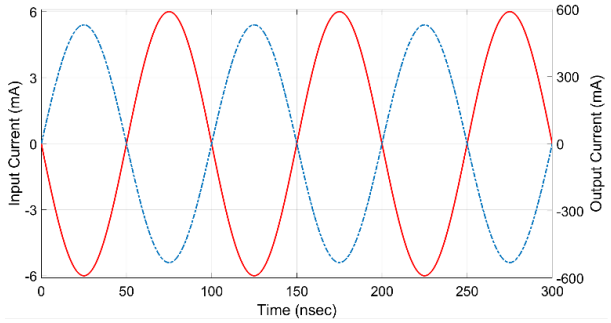

Fig. 2.22. The output current undergoes 180 degrees phase change resulting in negative impedance.

c) Tunnel Diode Based NIC

Tunnel diode is a semiconductor device which is based on the principle of quantum electron tunnelling and is capable of very fast switching operation with an operating frequency ranges of up to THz. It was first invented by Leo Esaki in 1957 [63]. A high conductivity, heavily doped two terminal P-N junction enables charge carriers to punch or tunnel through the junction by a process known as quantum tunnelling. With a small forward bias voltage, the current continues to increase until its peak value I_p and first positive differential region (PDR) is observed.

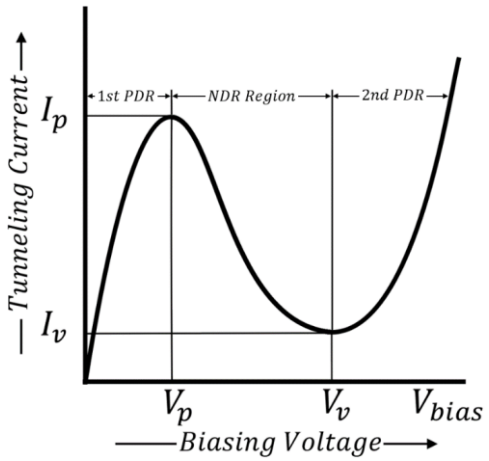

Fig. 2.23. Voltage-current behaviour of a tunnel diode. A small biasing voltage results in large tunnelling current exhibiting first positive differential resistance region. After reaching peak biasing voltage the tunnelling current rapidly falls resulting in NDR. After reaching valley voltage second positive differential resistance (PDR) region is observed.

When the tunnelling current reaches its maximum, very few unoccupied states are left in the p-type semiconductor and with a further increase in the biasing voltage, a reduced current and an inverse voltage-current

relationship is observed until the current reaches its lowest point known as valley current I_v at a valley voltage of V_v. This negative differential region results in negative impedance. Further increasing the voltage allows the normal current to flow and second PDR is observed. Fig. 2.23 shows general current-voltage characteristics of a tunnel diode.

A resonant tunnelling diode (RTD) is a variant of a tunnel diode based on double-barrier quantum-well (DBQW) structure. DBQW consists of a low band-gap quantum well material which is sandwiched between two high band-gap barriers. The barriers are the surrounded by emitter and collector as shown in Fig. 2.24.

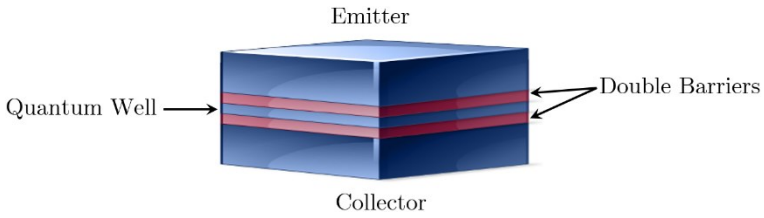

Fig. 2.24. RTD structure with the emitter, collector and double-barrier quantum-well. The resonant energy levels of the electrons enables them to tunnel through the double-barrier.

In the absence of forward bias on the collector, the current flow is zero because the electrons cannot tunnel through the double-barrier from the emitter to the collector side. With a small bias voltage, the electron from the emitter starts to accumulate near the barrier and only a small number are able to reach their first resonant energy level and hence tunnel through the double barriers. This results in a small current and as the biasing voltage is increased, the current increases. Further increasing the voltage results in a greatly reduced current which produces the negative differential region

(NDR). A study in [64] showed that a fabricated RTD sample L939F exhibits NDR up to a frequency of 7 GHz at a biasing voltage of 2.75 V. Fig. 2.25 shows the measured negative impedance of the aforementioned RTD.

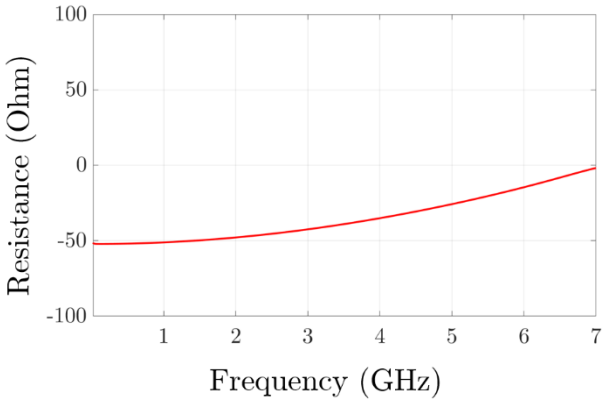

Fig. 2.25. Measured negative resistance of RTD L939F [64].

d) Modern NIC Design Approaches

Research advancements have accelerated the use of applications beyond the UHF and VHF frequency bands. Modern NIC design techniques are primarily based on the Linvil's proposed design and are implemented as surface mount transistors [65–68]. For instance, a NIC design was proposed and measured to provide negative resistance and inductance in VHF/UHF frequency range in [69]. The design was based on Linvill's open-circuit stable topology implemented as a CMOS integrated circuit utilizing a very low power of 5 mW.

A photograph of the micro-integrated circuit has been shown in Fig. 2.26, followed by measured and simulated results in Fig. 2.27.

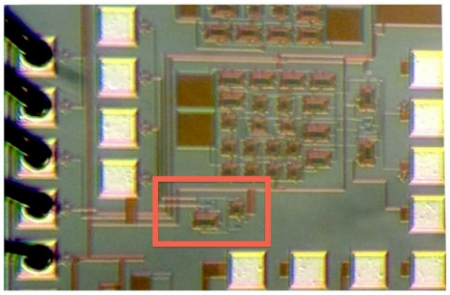

Fig. 2.26. Photograph of the fabricated NIC with the red box showing its location [69].

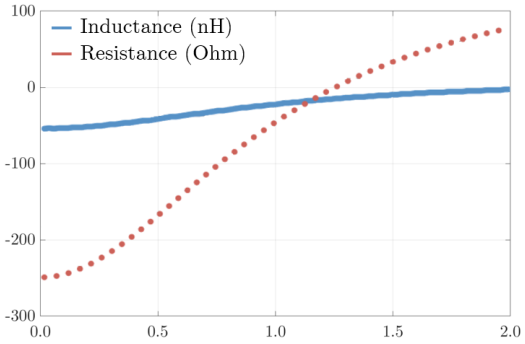

Fig. 2.27. Measured negative inductance and resistance of the NIC [69].

A comparison of various design implementation techniques for NIC circuits has been summarised in the table-1. It can be noticed that although BJT based NIC offers advantages in terms of cost and ease of fabrication, it suffers from stability issues which arise due to the feedback loop and nature of the design. Similarly, the op-amp based design is fairly simple and low profile with a low frequency range. A much modern and stable approach with a frequency support of up to THz range is based on resonant tunnel diode however the associated cost in terms of fabrication are high.

Considering the design of PT-symmetric systems at microwave frequency ranges and the thermal noise generated due to active NIC circuitry, the PT-symmetry can be rendered broken due to the increased noise figure of the system. The BJT based design has two active components that are a source

of thermal and shot noise. On the other hand, RTD or an op-amp based NIC would only have one active circuit component therefore a reduced noise figure. Further discussion has been made in the upcoming section where the primary noise sources of active and passive systems have been identified and the noise figure of the system has been estimated.

Table 2.2: Comparison between various design approaches for NIC.

	BJT	**Op-Amp**	**RTD**
Bandwidth	$0.1-1$ GHz	$<$40 MHz	$1-2$ GHz
Ease of Design	Complex	Simple	Simple
Stability Issues	High	Moderate	Low
Form Factor	Large	Small	Small
Power Consumption	High	Low	Very Low
Active Elements	2	1	1
Noise Figure	High	High	Low
Cost	Low	Low	High

2.3 Noise Fundamentals of Active and Passive Systems

Noise in any electronic system in unavoidable on all temperatures exceeding absolute zero. Noise originates due to the random flow of charge carriers resulting in the voltage and current fluctuation and the intensity of these random fluctuations varies from different electrical networks, devices and operating environments. The noise at the output of an electrical network is a superposition of various noise sources. In microwave networks, noise is passed on from the external or background sources or is generated within

the system itself due to active and passive circuit elements. The need to measure the noise figure of a system is to minimize the noise generated in the network and to ultimately determine the minimum performance threshold that a system can exhibit. An alternative approach to reduce the noise in a system could be an increase in the signal power. This would result in an improved signal-to-noise ratio (SNR) but such methods are complex and expensive and are therefore not very feasible. Hence, controlling the noise generated in the system itself is the most appropriate option.

The notable noise sources in active and passive systems are thermal noise, shot noise and flicker or $1/f$ noise. In order to minimize the noise of the system, it is important to develop equivalent noise models that contain dominant or all noise sources. These equivalent noise models are developed for a particular device type for instance, resistors, capacitors, inductors, BJTs, op-amps and diodes, and consist of a noise source in conjunction with ideal noiseless devices.

In this section, noise sources in a microwave system and circuit elements have been discussed. These include thermal noise, shot noise and flicker noise. In the later sections, equivalent noise models for basic circuit elements have been shown which include passive (loss) and active (gain) elements such as resistors, capacitors and inductors, BJTs, op-amps and diodes. Finally, the concept of noise figure and its measurements techniques have been discussed.

2.3.1 Thermal noise

Thermal noise is generated due to the random motion of charge or charge carriers above all temperatures exceeding absolute zero. This noise is also

known as Johnson noise because this was proved experimentally by J. B. Johnson in 1928 [70]. According to Johnson;

> *"Statistical fluctuation of electric charge exists in all conductors, producing a random variation of potential between the ends of the conductor. The electric charges in a conductor are found to be in a state of thermal agitation, in thermodynamic equilibrium with the heat motion of the atoms of the conductor. The manifestation of the phenomenon is a fluctuation of the potential difference between the terminals of the conductor".*

A non-ideal resistor at room temperature will have random voltage fluctuations across its terminals. The voltage exhibits zero average value however the root mean square (rms) value is non- zero. According to Plank's blackbody radiation equation [46]

$$\overline{v}_{resistor} = \sqrt{\frac{4hfBR}{e^{\frac{hf}{kT}} - 1}} \tag{2.56}$$

where,

h = Plank's constant.

k = Boltzmann's constant.

T = Room temperature in Kelvins (K).

B = Bandwidth in Hertz.

f = Frequency in Hertz.

R = Resistance in Ohms.

At microwave frequencies, the term $e^{\frac{hf}{kT}} - 1$ approaches to $e^{\frac{hf}{kT}}$ and the Eq. (2.56) can be written as

$$\overline{v}_{resistor} = \sqrt{4kTBR} \tag{2.57}$$

2.3.2 Shot Noise

The flow of electric current is not continuous, instead it is delivered to the electrical network in the form of small amounts which is equal to the charge on an electron. Shot noise originates through the current flow and is associated with random variations and fluctuations in the number of charge carriers passing over a junction or a boundary. The instantaneous current is limited by the smallest unit of charge available which is the charge on an electron. Shot noise exists in all active devices however it depends on various variables that are dependent on the type of devices such as transistors or amplifiers. Shot noise can be expressed in terms of current and can be written as [71]

$$v_{shot} = \sqrt{2eI_{DC}B} \tag{2.58}$$

where

$e =$ charge on an electron.

$I_{DC} =$ DC current.

$B =$ Bandwidth in Hertz.

2.3.3 Flicker Noise

Flicker noise or $1/f$ noise is dominant in the lower frequency range and it has a power spectral density equal to $1/f$. Flicker noise is present in all active devices which have DC biasing and is caused due to the imperfections during the fabrication processes and due to the fluctuation of the current flow. Research studies and analysis show that flicker noise exists in even very low frequencies such as up to 10^{-6} Hz with a frequency period spreading over several weeks.

Flicker noise is also used to model device fluctuation parameters with respect to time. Major models were developed by McWhorter [72] and Hooge [73] for surface and bulk structures respectively. The power spectral density of flicker noise can be written as

$$S(f) = \frac{K}{f} \tag{2.59}$$

Since the flicker noise has an inverse relationship with the frequency, there are certain application regions in which it dominates thermal and shot noise. A comparison of various dominant noise regions in contrast with flicker noise have been shown in Fig. 2.28.

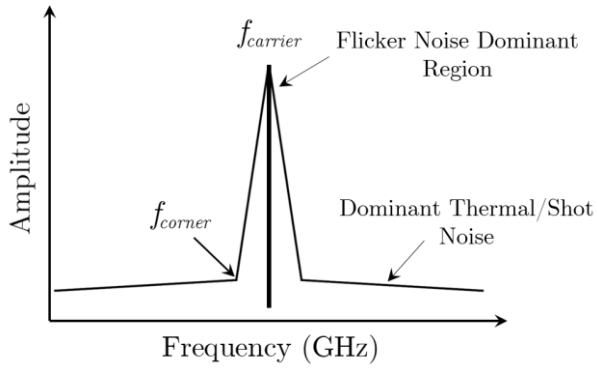

Fig. 2.28. Dominant noise sources in comparison with flicker noise.

2.3.4 Realisation of Noise Figure

The definition of noise figure came into use in 1940's when Harold Friis [74] defined the noise figure F of a network as a ratio of the SNR at the input to the SNR ratio at the output as

$$F = \frac{SNR_{in}}{SNR_{out}} \tag{2.60}$$

Therefore the noise figure of a network is the degradation of the input signal as it progresses through the network.

An ideal amplifier would not only amplify the input signal but also amplify the input noise along with the signal while maintaining the same signal-to-noise ratio at its input and output. However, a realistic amplifier would also include some extra noise that is generated from its own electronic components which degrades the signal-to-noise ratio.

Fig. 2.29(a) shows an input of an amplifier with a signal of 40 dB above the noise floor whereas Fig. 2.29(b) shows the output of the amplifier where the signal and noise floor have been amplified by 20 dB, with an additional 10 dB of amplifier internally generated noise. Now the output signal is at 30 dB above the noise floor level. This shows a degradation of the signal-to-noise ratio, therefore noise figure of the amplifier is 10 dB.

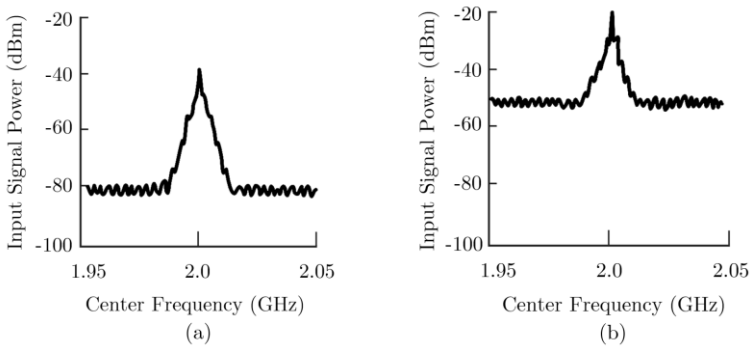

Fig. 2.29. (a) Signal level at the amplifier input. (b) The signal level at amplifier output with internal and amplified noise.

a) Noise Figure Measurement

The noise figure measurements are dependent upon the fundamental characteristic of two-port linear devices, i.e. noise linearity. The output noise power of a device is linearly dependent on the input noise power or

the noise temperature. Fig. 2.30 shows the linear behaviour with respect to the source noise temperature of a two-port device.

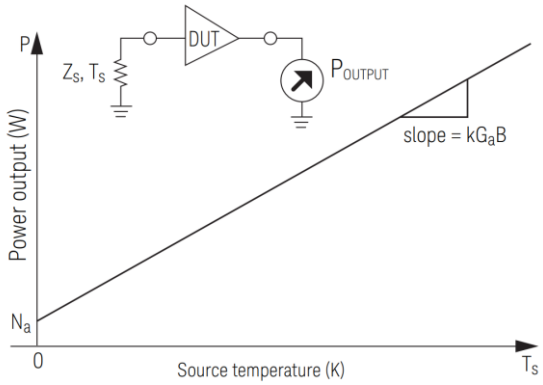

Fig. 2.30. Power output against source temperature characteristic of linear, two-port device. The output power is increased by thermal noise from the source and amplification by the gain parameter of the DUT.

If the slope kGB is known at a particular reference point, the input noise power and noise figure can be calculated. In order to determine the noise slope, a particular reference point must be specified. One way of doing that is to measure the change in the noise output while applying two different levels of input noise. This is achieved by a noise source device which consists of a low capacitance diode that generates the noise by biasing. When unbiased, the output noise is the thermal noise produced by the diode itself, however, when biased the noise is generated by the diode itself. The levels T_h and T_c refer to hot and cold noise temperatures respectively.

A noise source must have a calibrated output noise level which is determined by excess noise ratio (ENR) which is given as [46]

$$ENR_{dB} = 10\log\left(\frac{T_h - T_c}{T_0}\right) \tag{2.61}$$

Precise sources of noise are commercially available in order to reduce the mismatch errors during measurement. For instance, Fig. 2.31 shows the series noise generator 346CK01 by Keysight which is able to generate a noise temperature of 290 K when off and 10,000 K when on, with a matching frequency range of up to 50 GHz.

Fig. 2.31. Series noise source generator by Agilent. Photo by the courtesy of Peregrine Semiconductor, United Kingdom.

b) Noise Figure Measurement by Y-Factor Method

The Y-factor method is commonly used to make noise figure measurements. This method allows determining the internal noise temperature in the DUT. A noise source is connected to the DUT and the output power is measured corresponding to the noise source being switched off and switched on. The output noise power consists of the noise generated by the DUT and the noise generated by the noise source. The ratio of T_h (noise source switched on) and T_c (noise source switched off) is known as Y-factor and is written as [46]

$$N_1 = GkT_hB + GkT_eB \tag{2.62}$$

$$N_2 = GkT_cB + GkT_eB \tag{2.63}$$

Y-factor is given as

$$Y = \frac{N_1}{N_2} = \frac{T_h + T_e}{T_c + T_e} > 1 \tag{2.64}$$

$$T_e = \frac{T_h - YT_c}{Y - 1} \tag{2.65}$$

The setup diagram for the Y-factor method has been shown in Fig. 2.32.

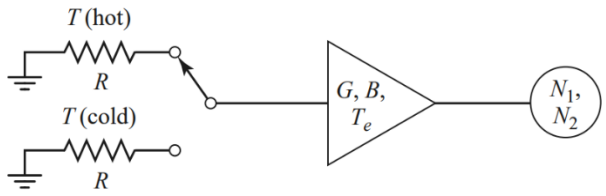

Fig. 2.32. Y-factor method using two noise sources at hot and cold noise temperatures.

c) Ultra-Fast Noise Figure Measurement

The device noise figure varies with a change in the source impedance, and this variation can be expressed in terms noise parameters which provide valuable information when designing low noise systems. These parameters can be mathematically related to each other as

$$F = F_{\min} + \frac{4R_n}{Z_0} \frac{\left[\left|\Gamma_s - \Gamma_{opt}\right|^2\right]}{(1 - \left|\Gamma_s\right|^2)\left|1 + \Gamma_{opt}\right|^2} \tag{2.66}$$

where,

R_n = Equivalent Noise Resistance

$F_{\min}$ = Minimum Noise Figure

$\left|S_{opt}\right|$ = Magnitude of the optimum noise reflection coefficient.

Γ_s = Source reflection coefficient

A general approach is to measure the noise figure F at various source impedance values i.e. Γ_s and then solve for the noise parameters by using Eq. (2.66) using simultaneous equation method. However, the noise measurements are very sensitive to small errors and therefore the measurements are repeated several times to estimate the noise figure by using least-mean-square algorithm [75–76].

Modern noise figure measurement is performed using automated impedance tuners to sweep the source impedance over the frequency band of interest at each state. The noise power measurement is also swept over the frequency range of interest such that the source impedance tuner moves to each source impedance only once. This method not only takes advantage of fast sweep times of modern instruments such as vector network analyzers but also maintains the impedance pattern at all frequencies and use non-uniform phase spacing to precisely evaluate the noise figure of the DUT. Fig. 2.33 and Fig. 2.34 show the block diagram and the noise parameter measurement setup by Maury Microwave respectively.

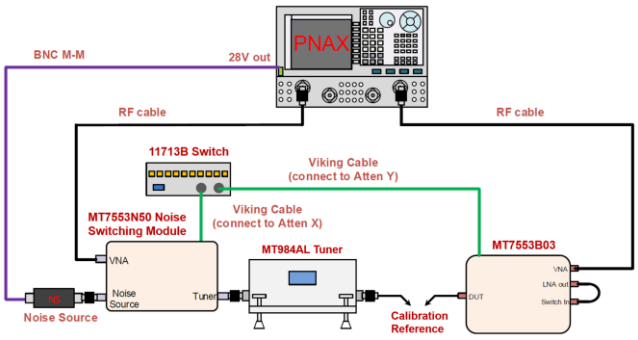

Fig. 2.33. Block diagram of the noise measurement setup.

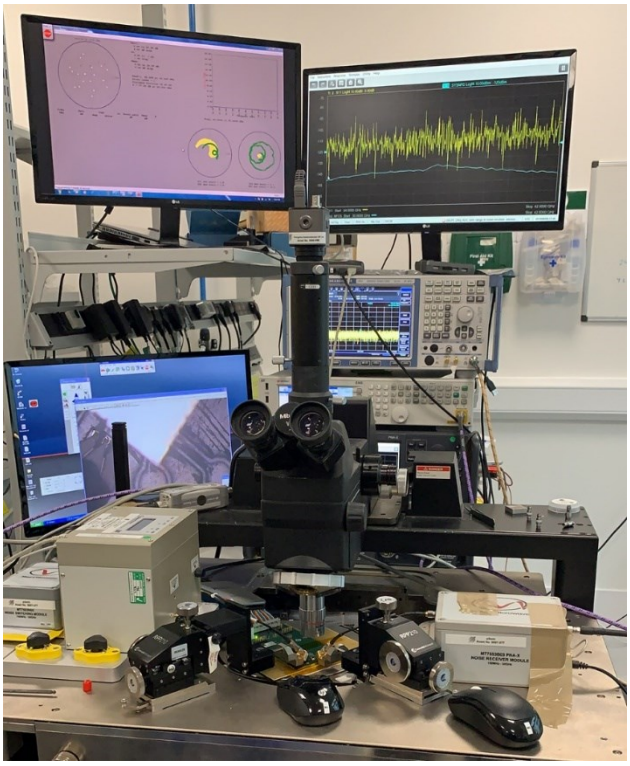

Fig. 2.34. Noise parameters measurement setup with load tuner and noise receiver on a probe station fixture with a DUT. Photograph taken on 9th September 2019 by the courtesy of Peregrine Semiconductor, UK.

2.3.5 Noise Characterisation of Active and Passive Devices

A microwave system is composed of various sub-circuit elements which can be classified into active and passive categories. Common passive circuit elements are resistors, capacitors and inductors whereas active elements are transistors, op-amps and diodes. In order to characterize the noise figure of the microwave system, it is important to express these elements into their equivalent noise models and then determine the overall system performance degradation due to noise. This section discusses the equivalent noise modelling and noise figure of basic circuit elements.

a) Resistors and Thermal Noise Figure

A non-ideal resistor at room temperature can be modelled as a noiseless resistor with an equivalent voltage or current noise source. A series noiseless resistor can be modelled as Thevenin equivalent with a noise voltage source generator given by Eq. (2.67). The schematic has been shown in Fig. 2.35.

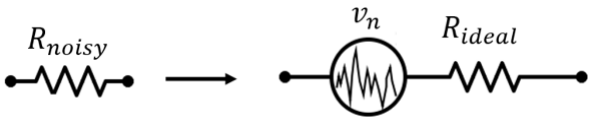

Fig. 2.35. Thevenin equivalent of a noisy resistor.

The rms noise voltage is given as

$$\overline{v}_{th}^2 = \sqrt{4kTBR} \tag{2.67}$$

The resistor can also be modelled as a Norton equivalent with an ideal noiseless resistor and an equivalent current noise source generator in shunt [46]. The Norton noise current equivalent is given by Eq. (2.68).

$$\overline{i}_{th}^2 = \sqrt{4kTB / R} \tag{2.68}$$

The equivalent circuit model can be seen in the Fig. 2.36.

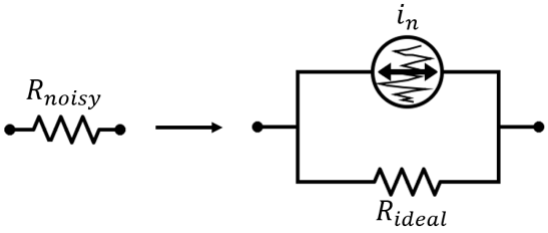

Fig. 2.36. Norton equivalent of a noisy resistor.

The power delivered to the load over a bandwidth of B is given as [46]

$$P_n = \left(\frac{V_n}{2R}\right)R = kTB \tag{2.69}$$

For a bandwidth of 1 Hz, the noise power would be estimated as -174 dBm/Hz. It is noted that the thermal noise power has a spectral density which remains constant with frequency, which means that the thermal noise power is frequency independent.

b) Capacitors

Ideal capacitors do not generate noise as is the case with all reactive elements. However, capacitors are composed of non-ideal conductors and dielectrics which have associated physical resistance that produces thermal noise. The noise voltage of a capacitor can be derived from equivalent circuit model of a capacitor which has been depicted in Fig. 2.37.

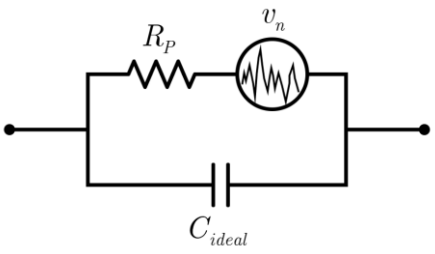

Fig. 2.37. Equivalent model of a capacitor with parallel resistance producing thermal noise.

The impedance of the equivalent circuit can be written as

$$Z = \frac{1/C}{j\omega + 1/R_P C} \tag{2.70}$$

Since thermal noise is produced due to the resistive part of impedance therefore we can write the noise voltage as

$$\overline{v}_n^2 = \sqrt{4kTB\,\mathrm{Re}(Z)} = \frac{4kTB}{R_P C^2}\frac{1}{\omega^2 + \left(1/R_P C\right)^2} \tag{2.71}$$

With some mathematical simplification, we can yield [77–79]

$$\overline{v}_n^2 = \frac{kT}{C} \tag{2.72}$$

This concludes that the noise voltage generated by a non-ideal capacitor is only dependent on the temperature and capacitance value. It is also important to realize the amount of noise power that a non-ideal capacitor would deliver to the load. For this purpose, consider the schematic shown in Fig. 2.38 where a capacitor is connected to the resistive load.

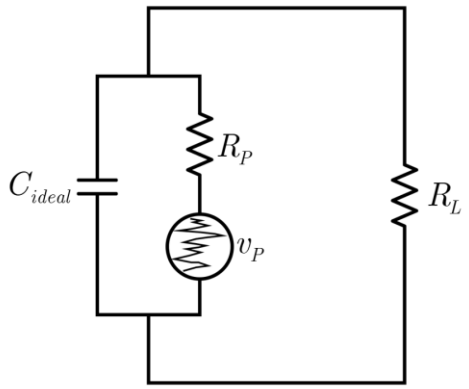

Fig. 2.38. A non-ideal capacitor with thermal noise source, delivering power to resistive load.

If the effective parallel resistance of the capacitor $R_P \gg$ then the voltage delivered to the load can be written as

$$V_C = \overline{v}_n \frac{1}{1 + 1 / j\omega R_L C} \tag{2.73}$$

The power delivered to the load is given by

$$P_n = \frac{V_C^2}{R_L} \tag{2.74}$$

Substituting Eq. (2.73) into Eq. (2.74) and simplifying yields

$$P_n = \frac{4kTB}{R_L R_P C^2} \frac{1}{\omega^2 + 1 / R_L^2 C^2} \tag{2.75}$$

If $\omega \ll$ then the noise power is given as

$$P_n = 4kTB\frac{R_L}{R_P} \tag{2.76}$$

The ratio of R_L / R_P is less than 1 therefore the Eq. (2.76) concludes that the thermal noise power from the capacitors is usually negligible because the noise power delivered to the load is much smaller than kTB.

c) Inductors

Real inductors exhibit thermal noise due to resistive losses. A non-ideal inductor can be modelled as an ideal inductor with an equivalent series resistance with thermal noise voltage source. The thermal losses in inductors are due to the losses in the inductor winding and the magnetic cores. A non-ideal inductor model is given in Fig. 2.39.

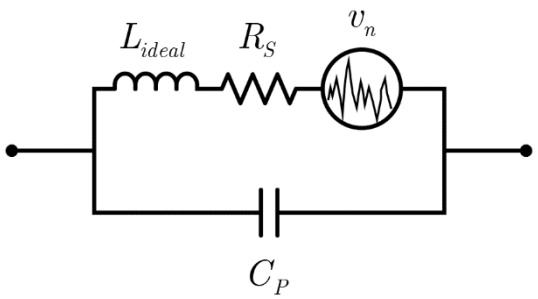

Fig. 2.39. Equivalent model of a non-ideal inductor with series resistance producing thermal noise voltage.

The noise voltage produced by a non-ideal inductor is written as

$$\overline{v}_n = \sqrt{4kTBR_S} \tag{2.77}$$

The noise power delivered to the load is

$$P_n = 4kTBR_S\frac{R_L}{\omega^2 L^2 + (R_S + R_L)^2} \tag{2.78}$$

If $\omega \ll$ and $R_S \ll$, above expression reduces to [79]

$$P_n = 4kTBR\frac{R_S}{R_L} \tag{2.79}$$

Eq. (2.79) concludes that the noise from inductors is always below the kTB threshold, where

$$kTB = -174 \text{ dBm/Hz}$$

d) Transistors

The dominant noise type in BJT's are commonly thermal noise, shot noise and flicker noise. The charge carrier arrival process at base and collector is random hence they exhibit shot noise. The terminals of the transistor have physical resistances r_b, r_c, r_e which can be modelled as noiseless resistors with equivalent noise voltage sources in series as v_b, v_c and v_e respectively. The base-emitter junction in transistor also exhibits flicker noise which can be modelled as their equivalent current generator sources. A noisy transistor can be modelled as a noiseless transistor with equivalent aforementioned noise sources. The equivalent noise model of a BJT has been depicted in Fig. 2.40.

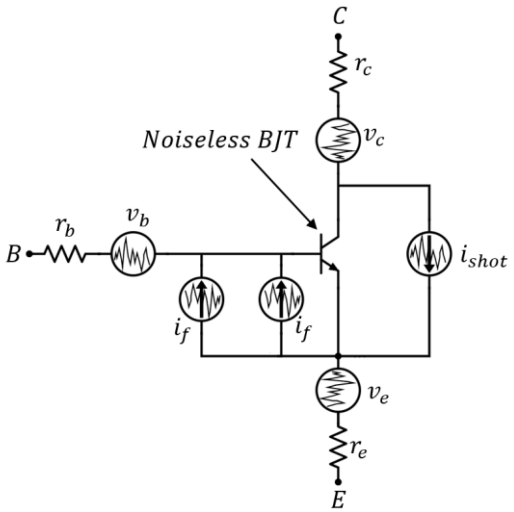

Fig. 2.40. Equivalent BJT circuit model of noisy BJT with noise sources.

$$v_b = \sqrt{4kTr_bB} \tag{2.80a}$$

$$v_c = \sqrt{4kTr_cB} \tag{2.80b}$$

$$v_e = \sqrt{4kTr_eB} \tag{2.80c}$$

Similarly, the shot noise for the base and collector current can be written as [79]

$$i_b = \sqrt{2qI_bB} \tag{2.81a}$$

$$i_c = \sqrt{2qI_cB} \tag{2.81b}$$

The total noise present in the transistor is the superposition of all the individual noise sources.

e) Operational Amplifiers

Op-amps exhibit thermal noise, shot noise and flicker noise contributions. Resistive elements contribute towards the thermal noise whereas biasing current contribute to shot noise and flicker noise. Noise modelling in op-amps is done by replacing the noisy op-amp with a noiseless amplifier and modelling the individual resistive components by replacing them with a noiseless resistor and equivalent noise voltage source. Similarly, shot noise and flicker noise is modelled by their appropriate noise current source. A non-ideal op-amp model with noise sources is shown in Fig. 2.41.

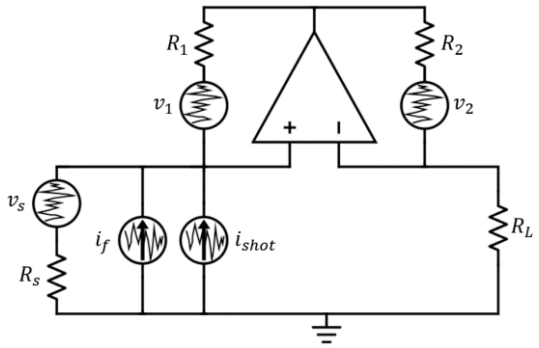

Fig. 2.41. Equivalent circuit model of a noisy operational amplifier. The thermal noise sources, shot noise, and flicker noise sources have been modelled.

f) Diodes

Diodes are active devices therefore they exhibit thermal and shot noise. The diode exhibits series resistance R_s, series inductance L_s and a pure negative resistance $-R_d$ and a junction capacitance C_d. The shot noise power depends on the current flowing through the diode and is given as [79]

$$\overline{v}_{shot} = \sqrt{2eI_{DC}B} \tag{2.82}$$

where,

e = charge on an electron.

I_{DC} = DC current.

B = Bandwidth in Hertz.

Since the diode exhibits physical resistance R_s, the thermal noise is also a dominant noise source which is given as

$$\overline{v}_{thermal} = \sqrt{4KTBR} \tag{2.83}$$

The equivalent small signal model of the tunnel diode has been shown in Fig. 2.42.

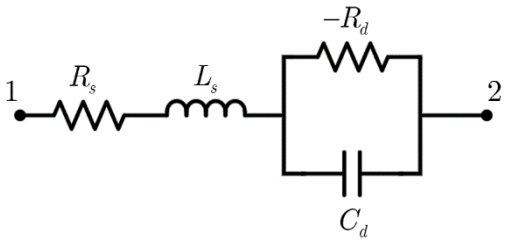

Fig. 2.42. A two-port small-signal equivalent model of a tunnel diode.

2.4 Summary

This chapter outlined the fundamental theory of wave-electromagnetics, Maxwell's equations and boundary conditions. It then explained the concepts of parity-time symmetry and its realisation in microwave electronic circuits in terms of loss and gain impedances coupled together through a transmission line. The chapter then discussed the scattering matrix formulism in PT-symmetric systems and discussed the conditions for reflectionless transmission at the exceptional points. The chapter presented that when the forward and reverse transmission become unitary in a two-port PT-symmetric system, the reflection coefficient at either port becomes zero. At this point, the system exhibits zero reflections and this condition is known as unidirectional transparency.

The chapter discussed the realisation of gain or negative impedance through negative impedance converters which can be incorporated in PT-symmetric system with loss and gain. These can be based on the technique of voltage or current inversion, implemented through BJTs or op-amps respectively. The chapter highlighted the common noise sources in practical electromagnetic systems such as thermal noise, shot noise and flicker noise. The chapter investigated the noise modelling in active and passive devices and discussed that the most dominant noise source in a PT-symmetric microwave system is thermal noise. Finally, the chapter discussed the concept of noise figure, its measurement techniques, and the equivalent noise models of basic active and passive circuit elements.

Chapter 3

PT-Symmetric Circuit Design

In section 2.2.4 it was discussed that PT-symmetric systems may yield unidirectional transparency at the exceptional points where the loss and gain are balanced. The input reflection coefficient vanishes, transmission becomes unity and output reflection coefficient becomes enhanced. However, it is of great important that a PT-symmetric system exhibits the ability to manipulate its reflection and transmission properties while sustaining PT-symmetry. In order to have such control over reflection and transmission behavior of PT-symmetric systems, an imaginary impedance can be included such that the parity and time-reversal postulates still hold and the system remains invariant under combined PT-transformation. Section 2.2 has previously presented the design postulates that can be followed to realize PT-symmetry in microwave electronics.

This chapter discusses the design of PT-symmetric systems using ideal resistive and reactive circuit elements connected through lossless transmission line. Each of the aforementioned design configuration offers unique application advantages and design flexibility. The ideal circuit design by using lumped elements enables to understand the reflection and transmission behaviour in the absence of noise. However, later chapters will discuss the implementation of practical PT-symmetric systems by using realistic active and passive circuit elements with equivalent noise models. The study performed in this chapter has been supported by analytical methods which have been further validated through circuit level and full-wave electromagnetic modelling and simulation techniques.

3.1 PT-Symmetric Circuits in Series Configuration

Consider the two-port network with its schematic shown in Fig. 3.01 which consists of two series resistors R_1, R_2 connected by a lossless transmission line of electrical length x with a propagation constant k, physical length d and a characteristic impedance of Z_0. In order to employ time-reversal symmetry, the resistors have opposite values such that $R_1 = rZ_0$ and $R_2 = -rZ_0$ where r is defined as a dimensionless, non-Hermiticity parameter which is normalized with respect to the characteristic line impedance of the transmission line. The series reactive element X has a complex impedance which can be given as $X = 1/j\omega C$ or $X = j\omega L$ for a capacitor or an inductor respectively.

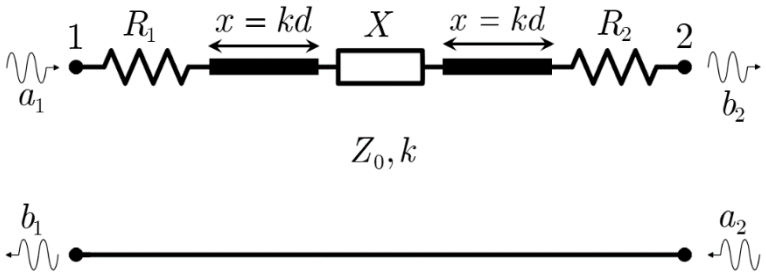

Fig. 3.01. A two-port PT-Symmetric circuit in series configuration with resistors R_1, R_2 connected together by a tranmission line of length $x = kd$ and an imaginary impedance given by a capacitive or inductive element. The time-reversal symmetry is applied through negative resistor R_2 with equal magnitude as positive resistor R_1.

From the definition of Parity-Time symmetry we conclude that the network is PT-symmetric because it is invariant under combined parity (P) and time-reversal (T) operators. The conditions are readily satisfied because interchanging the spatial coordinates of the two resistors and applying time-

reversal transformation does not effects the circuit and it remains invariant under such transformations. The positive resistor R_1 is a power sink that dissipates energy over time and its time-reversed version would correspond to a power source or amplification element which is a negative resistor R_2. Hence, the time-reversal symmetry is also satisfied because the system possesses R_1 (loss) and R_2 (gain) [13–14]. The point of interest is to investigate the system exceptional points which correspond to the system transitioning from an unbroken PT-symmetric phase to exact PT-symmetric phase.

3.1.1 Scattering Parameters

A microwave network could be described by scattering parameters or scattering matrix that define the incident and reflected signals at the specific ports. The point of interest is to compute the s-parameters and find the system exceptional point where the loss and gain are exactly balanced, and the system exhibits real eigenvalues. This is achieved by cascading the transmission or ABCD matrix of individual circuit elements and then computing the scattering parameters by following the notation described in [46].

The ABCD matrix of individual circuit element is calculated as

$$M_{R_1} = \begin{pmatrix} 1 & rZ_0 \\ 0 & 1 \end{pmatrix} \tag{3.1a}$$

$$M_{R_2} = \begin{pmatrix} 1 & -rZ_0 \\ 0 & 1 \end{pmatrix} \tag{3.1b}$$

$$M_X = \begin{pmatrix} 1 & X \\ 0 & 1 \end{pmatrix} \tag{3.1c}$$

$$M_{TL} = \begin{pmatrix} \cos x & iZ_0 \sin x \\ i \sin x / Z_0 & \cos x \end{pmatrix} \tag{3.1d}$$

where M_{R_1}, M_{R_2}, M_X and M_{TL} are transmission matrices for resistors R_1 R_2 the series reactance and the transmission line respectively. The overall ABCD parameters of the system are then found by cascading the individual matrices as

$$M_{ABCD} = M_{R_1} M_{TL} M_X M_{TL} M_{R_2} \tag{3.2a}$$

$$M_{ABCD} = \begin{pmatrix} A & B \\ C & D \end{pmatrix} = M_{R_1} M_{TL} M_X M_{TL} M_{R_2} \tag{3.2b}$$

With some mathematical simplifications, the transmission matrix elements are computed as

$$A = 2\cos^2 x + \frac{Xr(\cos^2 x - 1)}{Z_0} + \frac{\sin 2x(2rZ_0 + X)}{2Z_0} - 1 \tag{3.3a}$$

$$B = X + X \sin^2 x(r^2 - 1) + iZ_0 \sin 2x(1 - r^2) \tag{3.3b}$$

$$C = \frac{X(\cos^2 x - 1)}{Z_0^2} + \frac{iZ_0 \sin 2x}{Z_0} \tag{3.3c}$$

$$D = 1 - 2\sin^2 x - ir \sin 2x + \frac{Xr \sin^2 x}{Z_0} + \frac{iX \sin 2x}{2Z_0} \tag{3.3d}$$

The scattering matrix notation in terms of ABCD parameters and characteristic line impedance Z_0 a be followed from [46] where the scattering matrix is given as

$$S = \begin{pmatrix} S_{11} & S_{12} \\ S_{21} & S_{22} \end{pmatrix} \tag{3.4}$$

Substituting Eqs. (3.3a)-(3.3d) into Eq. (3.4) yields the individual scattering parameter element of the two-port PT-symmetric system as

$$S_{11} = \frac{A + B / Z_0 - CZ_0 - D}{A + B / Z_0 + CZ_0 + D} \tag{3.5a}$$

$$S_{12} = \frac{2(AD - BC)}{A + B / Z_0 + CZ_0 + D} \tag{3.5b}$$

$$S_{21} = \frac{2}{A + B / Z_0 + CZ_0 + D} \tag{3.5c}$$

$$S_{22} = \frac{-A + B / Z_0 - CZ_0 + D}{A + B / Z_0 + CZ_0 + D} \tag{3.5d}$$

For an electrical line length of $x = n\pi / 2$ where n=1, 3, 5..., the scattering parameters given through Eqs. (3.5a)–(3.5d), can be simplified as

$$S_{11} = \frac{X(r-1)^2}{Xr^2 - X - 2Z_0} \tag{3.6a}$$

$$S_{12} = S_{21} = \frac{2Z_0}{Xr^2 - X - 2Z_0} \tag{3.6b}$$

$$S_{22} = \frac{X(r+1)^2}{Xr^2 - X - 2Z_0} \tag{3.6c}$$

From Eqs. (3.6a)–(3.6c), it is evident that the scattering parameters of the PT-symmetric system are dependent on the non-Hermiticity parameter r, which itself depends on the resistors R_1, R_2 and the characteristic line impedance Z_0. The scattering parameters also depend on the electrical line length and the imaginary impedance originating through the series reactive element connecting the two transmission lines and the resistor pair.

Formulating the results from Eqs. (3.6a)–(3.6c), the four scattering parameters can be graphically visualized as shown in Fig. 3.02, as a function of electrical length and capacitive reactance.

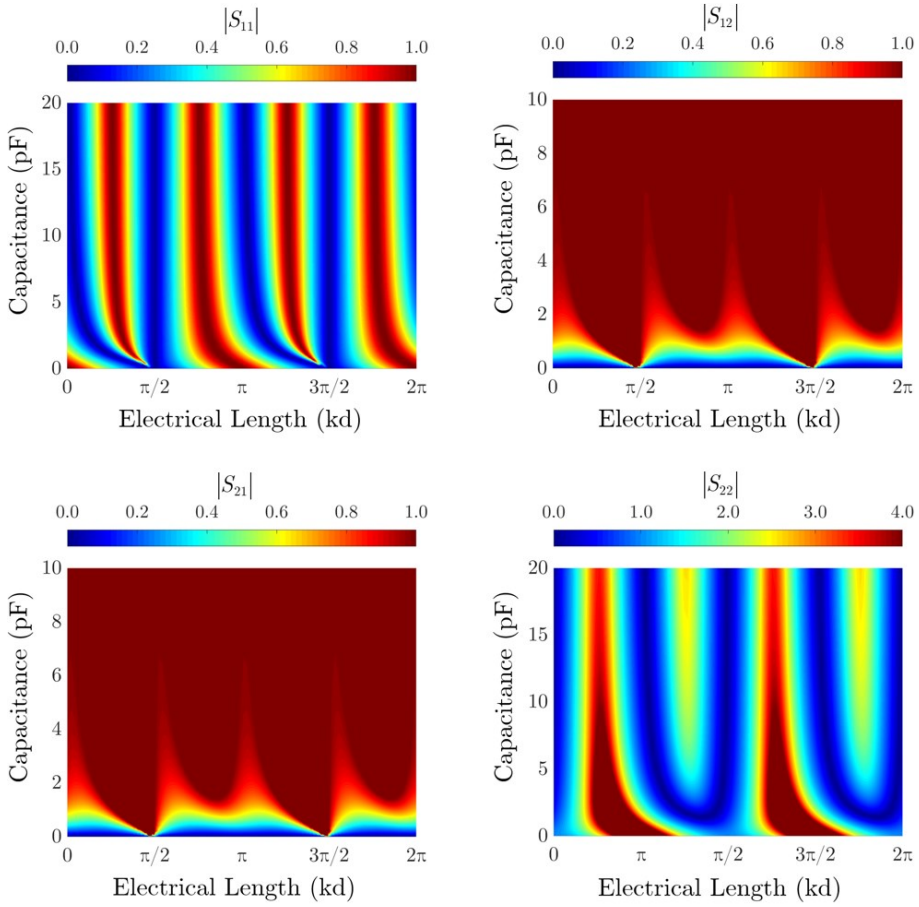

Fig. 3.02. Scattering parameters of the PT-symmetric circuit as a function of electrical length and capacitive reactance in series configuration at an exceptional point of $r = 1$. The schematic diagram has been shown in Fig. 3.01.

We can note from Fig. 3.02 that an electrical length of $x = n\pi / 2$, the system reaches its exceptional point and the reflection coefficient at the input port vanishes and the transmission becomes unity regardless of the

capacitive reactance. At this point, only the output reflection coefficient is a function of capacitive impedance and can be readily manipulated. The exceptional point periodically occurs at n=1, 3, 5....

Similar results are achievable through a series inductive reactance inclusion in the PT-symmetric circuit. Fig. 3.03 shows the scattering parameters as a function of series inductance and the electrical length of the transmission line.

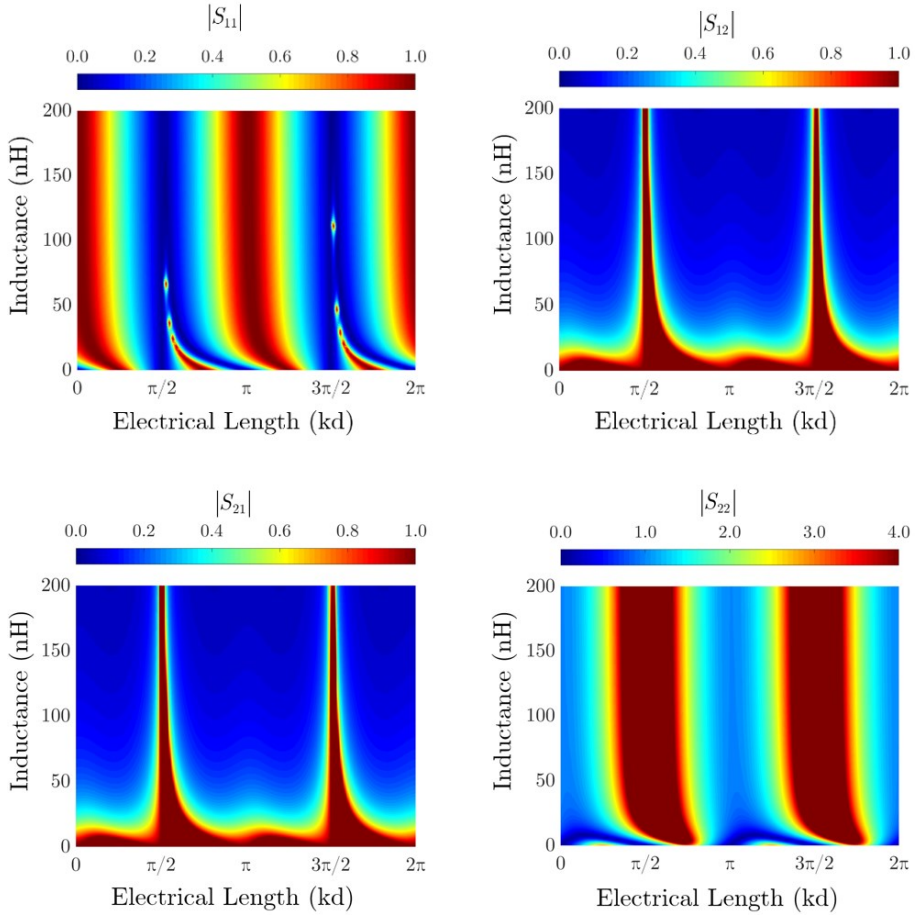

Fig. 3.03. Scattering parameters of the series PT-symmetric circuit as a function of electrical length and inductive reactance at an exceptional point of $r = 1$. The schematic diagram has been shown in Fig. 3.01.

3.1.2 Eigenvalues and Exceptional Points

PT-symmetric systems undergo phase transition at exceptional points where the eigenvalues become real from complex. The scattering matrix described in Eqs. (3.6a)–(3.6c) satisfy the following PT-symmetric condition [55].

$$PTS(\omega^*)PT = S^{-1}(\omega) \tag{3.7}$$

The eigenvalues of the series PT-symmetric system are computed through Eqs. (3.6a)–(3.6c) and have been depicted in Fig. 3.04.

$$\lambda_1 = \frac{X(r^2+1) + 2\sqrt{X^2r^2 + Z_0^2}}{X(r^2-1) - 2Z_0} \tag{3.8a}$$

$$\lambda_2 = \frac{X(r^2+1) - 2\sqrt{X^2r^2 + Z_0^2}}{X(r^2-1) - 2Z_0} \tag{3.8b}$$

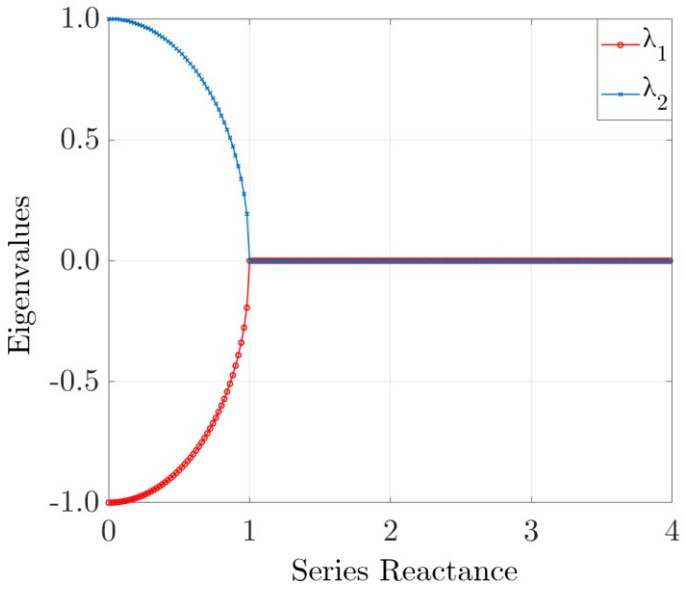

Fig. 3.04. Eigenvalues of the series PT-symmetric circuit as a function of reactance and non-Hermiticity parameter r. The exceptional point occurs at $r = 1$, showing a phase transition of the system.

3.1.3 Reflectionless Transmission at Exceptional Points

From the scattering parameters, we can notice that when the two resistors are equal to the transmission line impedance, i.e. at $r = 1$ and for electrical line length $x = n\pi / 2$ where n=1, 3, 5..., the reflection coefficient at port-1 vanishes and the magnitude of the transmission coefficient becomes unity, regardless of the imaginary impedance originating through capacitor or an inductor. The point $r = 1$ at an electrical length of $x = n\pi / 2$ is an exceptional point in the PT-symmetric system at which loss and gain are balanced. By following Eq. (2.40) from section 2.2.5, we can write

$$1 - |S_{21}|^2 = S_{11}S_{22}^*$$

which follows that when the transmission is unity, either of the reflection coefficient at port-1 or port-2 should disappear, resulting in full transmission. We can note that this is indeed the case here and the reflection coefficient at port-1 is zero. An exciting phenomenon here, is that the imaginary impedance from a series capacitance or inductance can only manipulate the output reflection coefficient S_{22} of the PT-symmetric system as suggested from the S_{22} plot in Fig. 3.02 and Fig. 3.03.

The scattering parameters in the complex plane with a varied range of non-Hermiticity parameter r have been depicted in Fig. 3.05 for various capacitive or inductive impedances in the PT-symmetric circuit to yield a broad range of output reflection coefficient at the exceptional point.

From a practical implementation perspective, one can also notice that the characteristic line impedance Z_0 and the electrical length x are constant in any fabricated microwave circuit and therefore cannot be varied conveniently as discussed in section 2.2.6. However, the PT-symmetric

circuit presented here utilizes imaginary impedance to achieve particular value of reflection coefficient at the output while sustaining PT-symmetry.

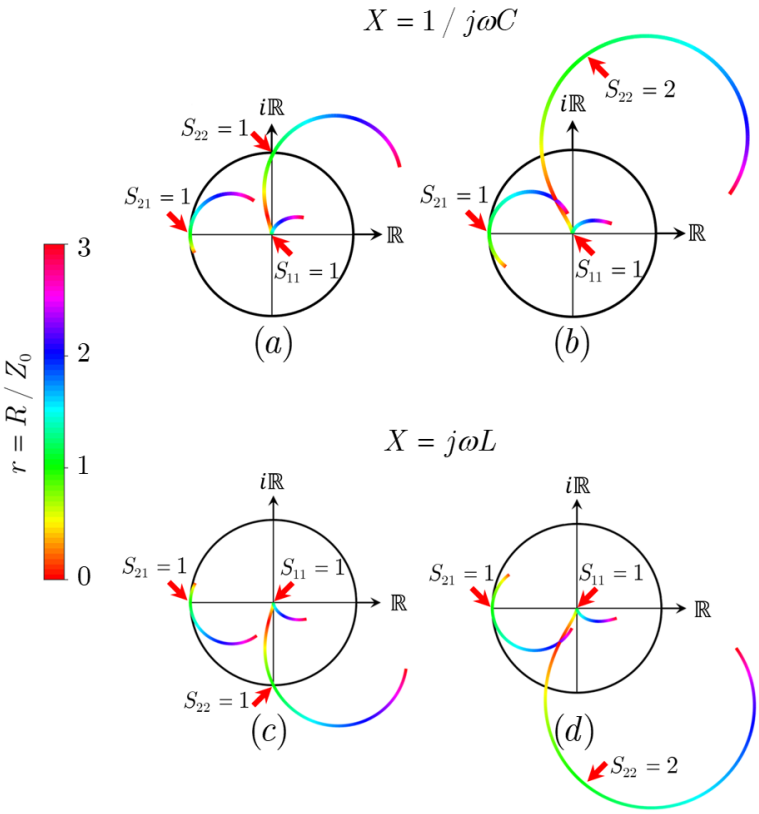

Fig. 3.05. Scattering parameters in complex plane as a function of reactance and non-Hermiticy parameter r. The system always exhibits zero reflection coeffecient at port-1 and unitary tranmission to port-2, regardless of the reactance. However, the output reflection is described by the selection of reactance. Two cases have been shown at 1.5 GHz. (a) At a capacitance of 4.45 pF the system shows unitary output reflection. (b) At a capacitance of 2.12 pF, the output reflection coeffecient magnitude increases to two. (c) At an inductance of 2.65 nH the output reflection coeffecient is 1. (d) At and inductance of 5.3 nH the output reflection magnitude increases to twice. The red arrows correspond to exceptional point of the PT-symmetric circuit.

In order to develop further understanding and to validate the concept, circuit level simulation can be performed by using ideal lumped elements

and lossless transmission line by using a commercial microwave circuit simulator.

Utilizing a series reactive element by following the circuit schematic shown in Fig. 3.01, it can be verified that the output reflection coefficient can be manipulated while other reflection and transmission parameters remain unaffected. Fig. 3.06 shows the simulated scattering parameters of the PT-symmetric circuit as a function of capacitive and inductive reactance at the exceptional point of $r = 1$ and the results coincide with the analytical results shown in Fig. 3.05.

However, it can be noticed that a series inductance offers a linear response in manipulating the output reflection coefficient. For instance, a small inductance change can broadly vary the output reflection response of the PT-symmetric circuit and while the input reflection is zero, a zero output reflection is also achievable through a small inductance inclusion in the system. On the contrary, a capacitive reactance shows an asymptotic behaviour.

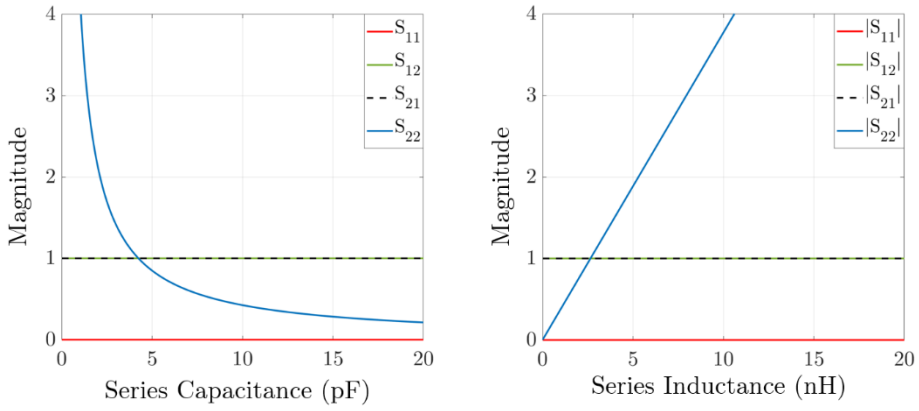

Fig. 3.06. Scattering parameters of a PT-symmetric circuit as a function of series reactance through a capacitor and inductor at an exceptional point of $r = 1$.

3.2 PT-Symmetric Circuits in Shunt Configuration

The design of PT-symmetric circuits in series or shunt topologies offers unique advantages in terms of application design perspective which will be discussed in subsequent chapters. The PT symmetric circuit shown in Fig. 3.01 can also be described in shunt configuration. Consider the two port network schematic in Fig. 3.07 where the resistors R_1, R_2 and the reactive element X have now been placed in a shunt configuration. Following PT-symmetry postulates described in [13–14] the system is PT-symmetric. The parity and time-reversal invariance hold because interchanging the spatial coordinates of resistor R_1 and R_2 , and further applying time-reversal transformation by replacing loss with gain and vice versa, the system remains invariant.

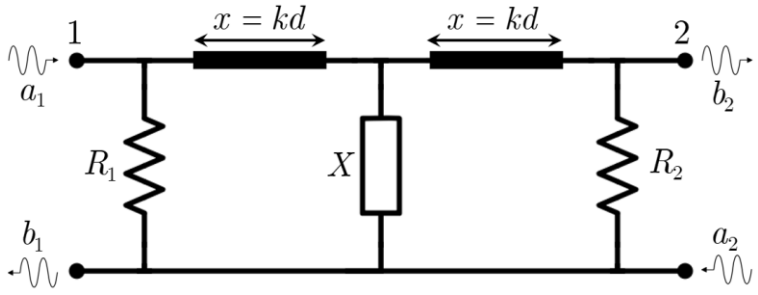

Fig. 3.07. A two-port PT-Symmetric circuit in shunt configuration with loss and gain resistors R_1, R_2 are connected together by a transmission line and an imaginary impedance X which may be given by a capacitor or inductor. The time-reversal symmetry is applied through negative resistor with equal magnitude as positive resistor.

3.2.1 Scattering Parameters

The scattering parameters for the shunt configuration can be obtained by following the ABCD and scattering matrix notation by following [46] and the formulation explained in the earlier section. The scattering parameters

of the PT-symmetric system in shunt configuration at an electrical length of $x = n\pi / 2$ where n=1, 3, 5... are computed as follows

$$S_{11} = \frac{Z_0(r-1)^2}{r^2(2X + Z_0) - Z_0} \tag{3.9a}$$

$$S_{12} = S_{21} = \frac{2ir^2X}{r^2(2X + Z_0) - Z_0} \tag{3.9b}$$

$$S_{22} = \frac{Z_0(r+1)^2}{r^2(2X + Z_0) - Z_0} \tag{3.9c}$$

The scattering parameters in Fig. 3.08 have been shown as a function of electrical length and capacitive reactance.

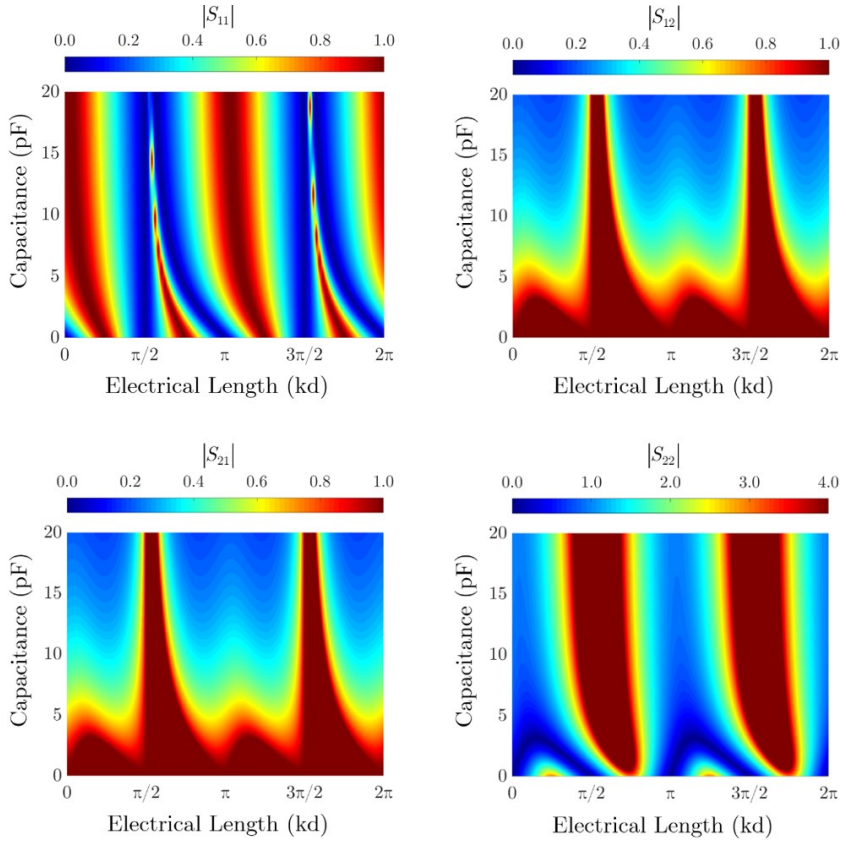

Fig. 3.08. Scattering parameters of the shunt PT-symmetric circuit as a function of electrical length and capacitive reactance at an exceptional point of $r = 1$. The schematic diagram has been shown in Fig. 3.07.

Similarly, the scattering parameters for the shunt PT-symmetric circuit as a function of electrical length and shunt inductance have been shown in Fig. 3.09.

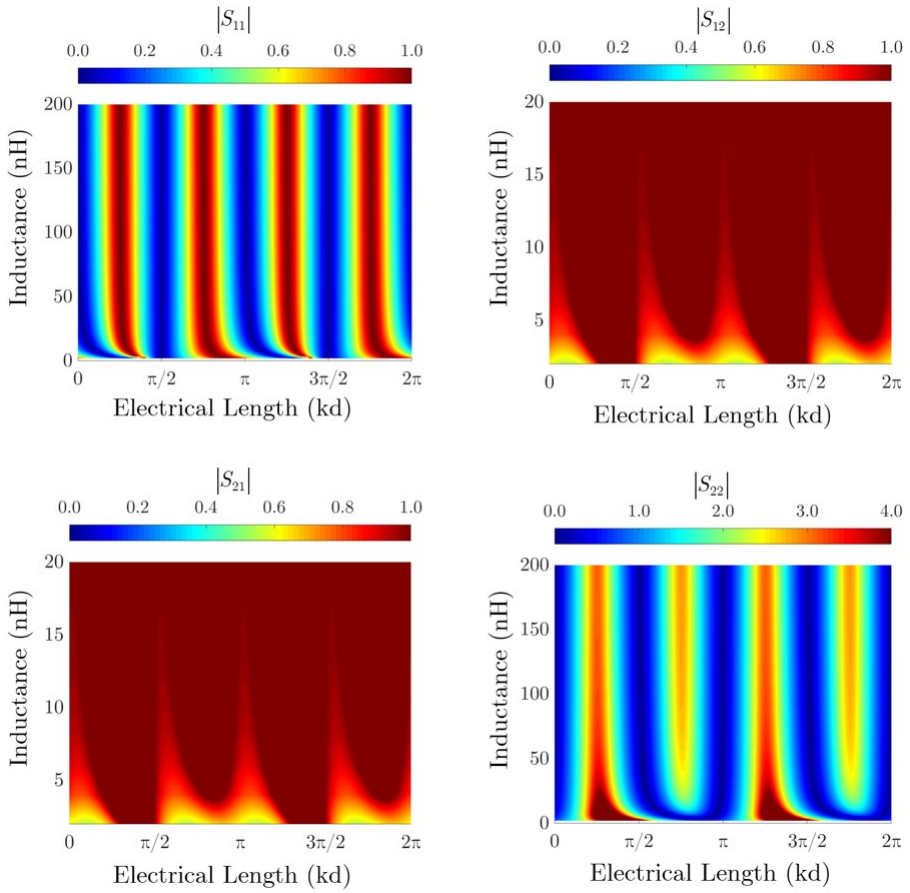

Fig. 3.09. Scattering parameters of the shunt PT-symmetric circuit as a function of electrical length and inductive reactance at an exceptional point of $r = 1$. The schematic has been shown in Fig. 3.07.

We can note from Fig. 3.08 and Fig. 3.09 that with an inclusion of a shunt reactance, the reflection and transmission parameters can be effectively manipulated. In the upcoming sections, we will discuss the exceptional points of PT-symmetric circuits in shunt configuration and conditions for reflectionless transmission along with analytical and simulated validations.

3.2.2 Eigenvalues and Exceptional Points

The eigenvalues of the PT-symmetric circuit in shunt are calculated from the scattering parameters given by Eqs. (3.9a)–(3.9c) and are given as

$$\lambda_1 = \frac{Z_0 + r^2 Z_0 + 2r\sqrt{X^2 r^2 + Z_0^2}}{r^2(2X + Z_0) - Z_0} \tag{3.10a}$$

$$\lambda_2 = \frac{Z_0 + r^2 Z_0 - 2r\sqrt{X^2 r^2 + Z_0^2}}{r^2(2X + Z_0) - Z_0} \tag{3.10b}$$

The exceptional point occurs at $r = 1$, showing the system transisioning state. Fig. 3.10 shows the two eigenvalues for the scattering matrix for shunt configuration described in Eq. (3.10a) and Eq. (3.10b).

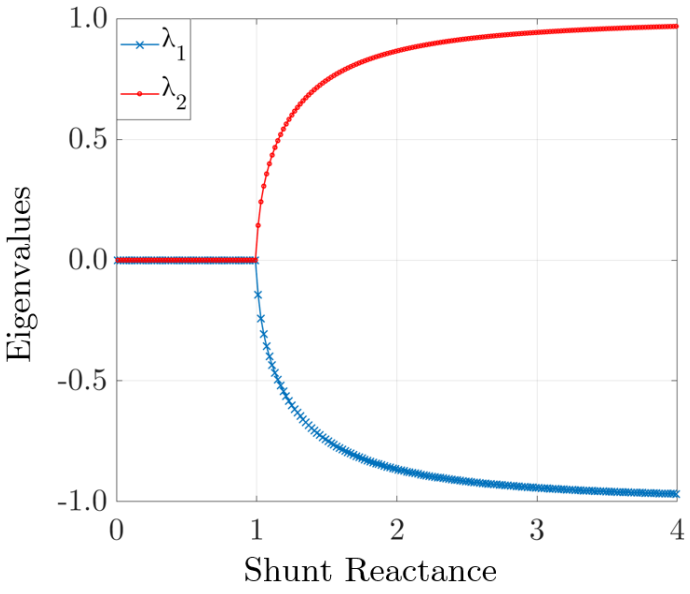

Fig. 3.10. Eigenvalues of the shunt PT-symmetric circuit as a function of reactance and non-Hermiticity parameter r. The exceptional point occurs at $r = 1$, showing a phase transition of the system.

3.2.3 Reflectionless Transmission at Exceptional Points

From Eqs. (3.9a)–(3.9c), we can identify the symmetry breaking or exceptional point at $r = 1$. The scattering parameters for the PT-symmetric circuit shown in in shunt configuration are shown in Fig. 3.11 in a complex plane where the origin of unit circle marks zero reflection whereas a radius of 1 represents full reflection.

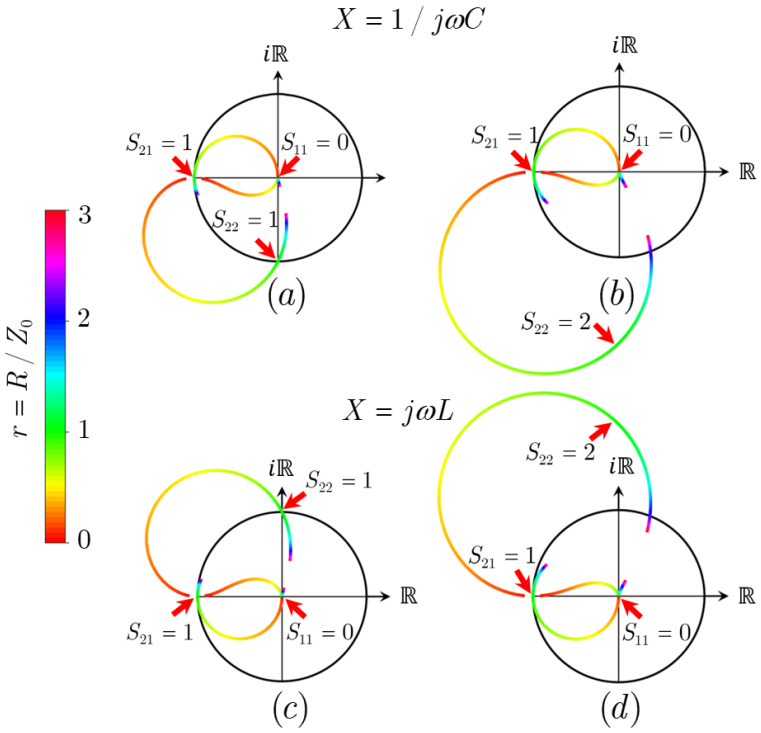

Fig. 3.11. Scattering parameters in complex plane as a function of capacitive or inductive reactance, and the non-Hermiticy parameter r at an electrical length of $n\pi / 2$. The two-port system is matched from port-1 with unity transmission regardless of the reactance. However, the output reflection is described by the selection of reactance. (a),(c) Capacitance of 1.1 pF or an inductance of 10.6 nH yields $S_{22} = 1$. (b),(d) Capacitance of 2.12 pF or an inductance of 5.3 nH, the output reflection coeffecient increases to twice.

It can be observed that the PT symmetric circuit designed in shunt configuration now necessitates a capacitance of 1.1 pF or an inductance of 10.6 nH to render a unity output reflection magnitude. Similarly, a capacitance of 2.12 pF or an inductance of 5.3 nH is able to achieve an output reflection magnitude of 2. This concludes that PT-symmetric circuit designed in shunt configuration require lower capacitance to achieve a particular value of reflection at the output. This is favorable in terms of a practical circuit design perspective. For instance a varactor diode in shunt can provide an appropriate variable junction capacitance in a small range at design frequencies hence resulting in a broader variance of reflection magnitude. However, the tradeoff comes at an increased noise figure of the system. Further discussion on the noise performance of PT-symmetric systems has been explored in later chapters of this thesis where the noise figure of series and shunt systems have been discussed.

In order to validate the analytical findings, a circuit level simulation has been performed by using a commercial circuit simulator such as Keysight ADS. It can be noticed from the scattering parameters shown in Fig. 3.12 that the inductor choice in shunt is not quite favorable in terms of transmission and reflection manipulation. For instance, at an electrical length of $x = n\pi / 2$, the inductor is not able to achieve a zero output reflection coefficient. The primary reason for this behavior occurs due to the asymptotic response of the shunt inductor in the PT-symmetric circuit. Therefore, it can be concluded that capacitor is a better choice in designing shunt PT-symmetric circuits whereas inductor is a better choice in series PT-symmetric circuit design. This has been shown in Fig. 3.12 where the scattering parameters of the PT-symmetric system have been shown in shunt configuration as a function of capacitive and inductive reactance.

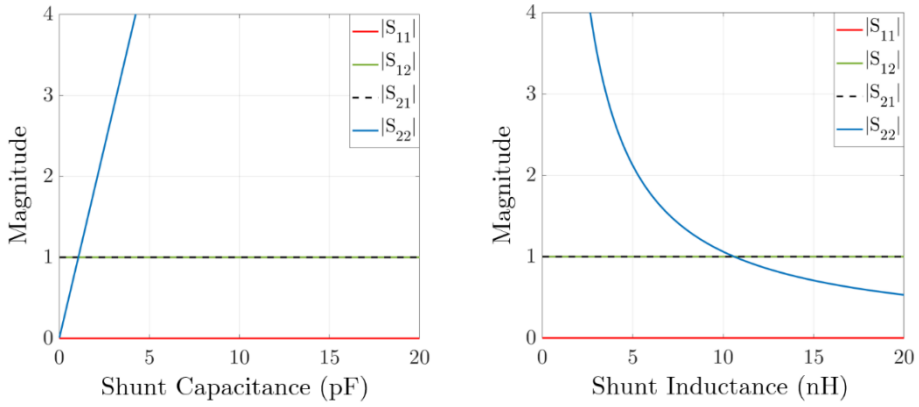

Fig. 3.12. Scattering parameters of a PT-symmetric circuit in shunt configuration as a function of shunt reactance through a capacitor and inductor at an exceptional point of $r = 1$. The capacitor offers a linear response in manipulating output reflection whereas an inductor shows asymptotic behaviour.

To develop a deeper understanding of the explained concept, we have performed full-wave electromagnetic simulations for an incident electromagnetic wave on the PT-symmetric system at its exceptional point using COMSOL Multiphysics. The incident plane wave with an arbitrary microwave frequency of 1.5 GHz is launched from the loss side of the system depicted in schematic shown in Fig. 3.01 and Fig. 3.07. The capacitive/inductive reactance has been modelled as an ultrathin uniform metasurface, sandwiched between loss and gain metasurfaces with an electrical length seperation of $x = n\pi / 2$ where n is an odd integer multiplier. The geometric setup for the COMSOL Multiphysics simulation has been shown in Fig. 3.13. The resistive metasurfaces with loss and gain are defined as

$$R_1 = rZ_0 = 50\ \Omega$$

$$R_2 = -rZ_0 = -50\ \Omega$$

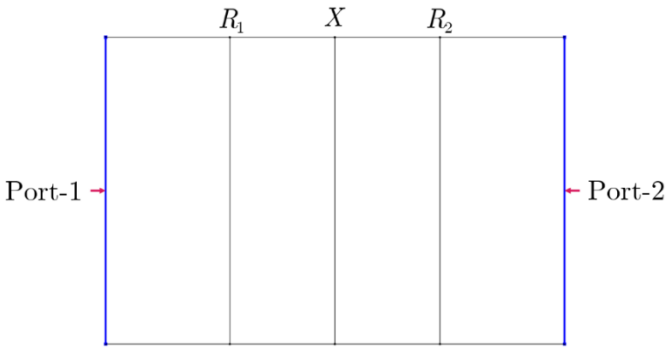

Fig. 3.13. Geometric setup of the PT-symmetric circuit with loss, gain and reactive elements modelled as a uniform ultrathin respective impedances.

Fig. 3.14 shows the full-wave simulation for the PT-symmetric system with a plane wave with a magnitude of 1 V/m is incident from the loss side through port-1. At the exceptional point of $r = 1$, the incident wave experiences zero input reflection coefficient and gets fully transmitted towards port-2 with forward and reverse transmission coefficients equal to unity. The simulated results coincide with the analytical results previously discussed in section 3.2.3.

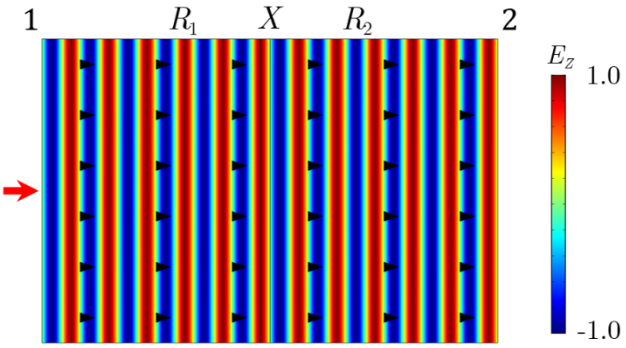

Fig. 3.14. Time snapshot of full-wave simulation for the PT-symmetric circuit in shunt configuration at 1.5 GHz. When the system is excited from port-1, the incident EM wave is transmitted through the structure without any perturbation with a forward tranmission coeffecient of unity. The black arrows represent average power flow in the system also known as Poynting vector.

However, if the wave is incident at port-2, it experiences the gain metasurface as a first plane of incidence which results in enhanced reflection whose magnitude is given by the selection of capacitive or inductive impedance in the PT-symmetric system. The scattering matrix is developed as

$$S = \begin{pmatrix} 0 & 1 \\ 1 & 2Z_0 / X \end{pmatrix} \tag{3.11}$$

where $X = 1/j\omega C$ for a capacitive impedance, and $X = j\omega L$ for an inductive impedance in the system.

For instance, utilizing a shunt PT-symmetric circuit configuration and including a capacitance of 1.1 pF or an inductance 10.6 nH yields a reflection coefficient of unit magnitude at port-2 which corresponds to a full reflection of the incident wave with equal magnitude as shown in Fig. 3.15. Alternatively, a broader range of output reflection coefficients can be obtained by varying the shunt capacitance in a small range as discussed earlier in section 3.2.3. It is also to be noted that the imaginary impedance discussed here only affects the output reflection coefficient i.e. S_{22}. Whereas S_{11} remains zero and forward and reverse transmission coefficients remain unitary.

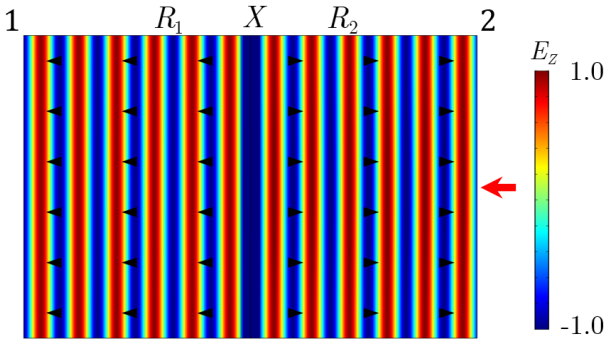

Fig. 3.15. Time snapshot of full-wave simulation for the PT-symmetric circuit with an incident wave at port-2. A capacitance of 1.1 pF or an inductance of 10.6 nH yields $S_{22} = 1$.

Similarly, the system excitation from port-2 with a capacitance of 2.12 pF or an inductance of 5.3 nH yields enhanced reflection with twice the magnitude of the incident wave. Fig. 3.16 shows the full-wave simulation snapshot of the described phenomenon.

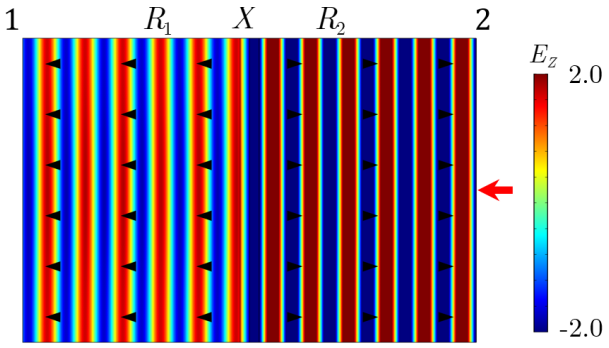

Fig. 3.16. Time snapshot of a full-wave simulation with an excitation from port-2 and a capacitance of 2.12 pF or an inductance of 5.3 nH. The output reflection coefficient is increased to a magnitude of 2.

3.3 Cascaded PT-Symmetric Systems

So far we have discussed the design of PT-symmetric circuits in series and shunt circuit configurations. However, circuit configurations are also possible if PT-symmetry condition is valid. In other words, loss and gain resistances must occur in parity pairs which may be in series, shunt, or a hybrid configurations.

In order to realize loss and gain coupling, a simple approach by using a transmission line can be incorporated. However, more complex approaches such as a mutually coupled transformer with mutual inductance can also be utilised.

An illustration of a generalized PT-symmetric system in microwave electronics has been shown in Fig. 3.17 which is composed of gain and loss

resistors with incident and reflected waves to describe the scattering parameters.

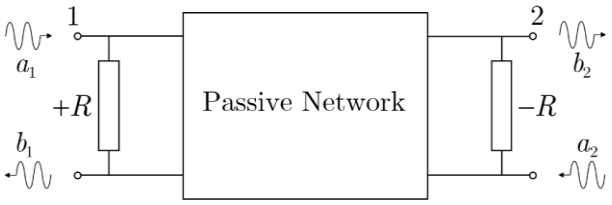

Fig. 3.17. An illustration of a PT-symmetric system with balanced loss and gain modelled as positive and negatives resistor connected together through a transmission line or a complex passive network.

For instance, consider the arbitrary schematic given in Fig. 3.18 where two individual PT-symmetric systems composed of loss and gain have been cascaded together through a coupling reactive element. It can be noticed that the system is PT-symmetric because interchanging the spatial coordinates of gain-loss resistors and applying time-reversal symmetry, the system invariance still holds. The point of interest is to approach the exceptional point of the PT-symmetric system so that the loss-gain balance can be reached to realize a stable system.

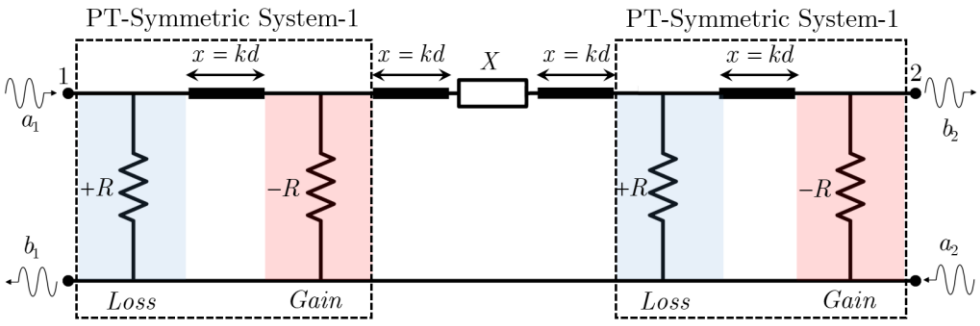

Fig. 3.18. Two cascaded PT-symmetric systems coupled together with an imaginary impedance. Each individual PT-symmetric system is composed of loss and gain resistors with satisfied parity and time-reversal symmetry conditions. The cascaded system also holds PT-symmetry.

The scattering matrix of the aforementioned cascaded PT-symmetric system is calculated by following similar formulation as explained in section 3.1.1. The scattering matrix elements are given as

$$S_{11} = \frac{X(r-1)^2}{Xr^2 - X - 2Z_0} \tag{3.12a}$$

$$S_{12} = S_{21} = \frac{2Z_0}{Xr^2 - X - 2Z_0} \tag{3.12b}$$

$$S_{22} = \frac{X(r+1)^2}{Xr^2 - X - 2Z_0} \tag{3.12c}$$

We can realize that the scattering matrix of the cascaded PT-symmetric system are similar to that of the series PT-symmetric system shown in Fig. 3.01. However, it must be taken into consideration that the higher number of elements in a PT-symmetric system would result in an increased noise figure of the system. Therefore, the design of PT-symmetric system depends on the application requirements. For instance, a particular unidirectional cloaking or RCS reduction applications, a high noise figure would result in degraded performance of the PT-symmetric cloak. Further studies have been performed in the next section where application design of a PT-symmetry has been shown as a unidirectional cloak and RCS approximation has been performed.

3.4 Summary

This chapter showed that an imaginary impedance originating through a capacitor or an inductor can effectively manipulate reflection and

transmission behavior in PT-symmetric systems while sustaining parity and time-reversal symmetry. Circuit configuration in series and shunt has been studied to provide broad range of reflection and transmission magnitudes by the inclusive capacitive and inductive impedances. The chapter further showed that the electrical line length plays a crucial role in PT-symmetric application design. For instance, at an electrical length of $n\pi / 2$ where n is an odd multiplier, the output reflection coefficient magnitude of the PT-symmetric circuit is defined by the capacitive or inductive impedances. Similarly, at an electrical length of $n\pi$ where n is an integer multiplier, both the reflection and transmission coefficients of PT-symmetric system can be manipulated through the capacitive or inductive impedances. The aforementioned studies have been verified analytically and the transmission and reflection behavior is validated and visualized by a full-wave simulation models for series and shunt configurations.

Contribution Overview

- Presented a transmission line model of PT-symmetric circuits in series and shunt topologies and evaluated the associated scattering parameters and eigenvalues.

- Presented a non-invasive technique to manipulate the transmission and reflection properties of aforementioned PT-symmetric circuits. For instance, a capacitive or inductive element can be incorporated in the PT-symmetric circuit with satisfied PT-symmetry postulates.

- Presented and discussed the transmission line and equivalent full-wave simulation models for the aforementioned PT-symmetric circuits and validated the analytical results.

Chapter 4

Noise Characterisation of PT-Symmetric Circuits

In chapter 3 we have investigated the design of PT-symmetric systems using ideal lumped elements. This provides a useful insight in understanding the behaviour of such systems in terms of reflection and transmission properties under ideal loss and noise free domains. Although such systems can be designed to minimize overall losses by compensating loss with equivalent gain proportions, noise in a practical RF system with loss (passive) and gain (active) components, is unavoidable.

Studies have suggested that the primary bottlenecks in designing and implementing PT-symmetric systems at microwave frequency ranges are noise and instability that can weakly break PT-symmetry resulting in system performance degradation [17]. Practical implementation of such systems and devices require significant level of control and stability and it is crucial to characterise the fundamental noise sources in terms of noise figure and signal-to-noise ratio. In realistic domains, PT-symmetric systems employ non-ideal active and passive circuit elements that generate various types of noise. Primary noise contributions originate through lossy resistor $+R$, which is a source of Johnson-Nyquist or thermal noise, and through the gain resistor $-R$. The negative resistor does not occur as a standalone circuit element and hence it is implemented through operational amplifiers and negative impedance converters (NIC) at low frequencies or a resonant

tunnel diode (RTD) at microwave frequencies, hence exhibiting thermal noise, shot noise and flicker noise contributions. In this chapter, we have considered a tunnel diode to provide negative resistance at the frequency of interest to realise gain element in PT-symmetric circuits. The primary reason for this choice is that a tunnel diode not only supports frequency ranges up to THz but also has the least active element count which favours least possible noise contribution and greater stability as compared to other NIC techniques such as BJT or op-amp therefore allowing best performance.

In this chapter, we first present equivalent noise models of PT-symmetric circuits in series and shunt configurations. We then calculate the noise figure of aforementioned systems using analytical methods and further validate the analytical results using simulation techniques.

4.1 Noise Figure of PT-Symmetric Circuit in Series

In section 3 we have discussed an ideal, lumped element PT-symmetric circuit model in series configuration where loss and gain resistors are connected together through a transmission line and separated by an imaginary impedance. The circuit schematic from Fig. 3.01 has been shown here for convenience.

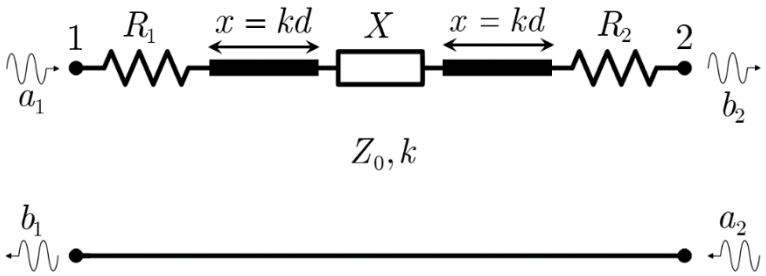

Fig. 4.01. Schematic from section-3 of series PT-symmetric circuit with ideal lumped elements. The system is free from any associated noise and system losses.

By following the schematic we can identify that the conventional resistor $+R$ is the primary source of thermal noise. The series reactive element can be a capacitor or an inductor whose generated noise current or voltage is much less than kTB as discussed in section 2.3.5, hence for the purpose of brevity, the associated noise contribution has been be neglected.

Similarly, the negative resistor R_2 is realized using a tunnel diode of sample L939F to give a negative resistance of -49.77 Ω at 1.5 GHz and hence can be replaced by its equivalent circuit model as followed from section 2.29(c). The overall system noise figure can then be estimated using analytical methods and can be further validated through circuit level simulations. The equivalent circuit model of a non-ideal PT-symmetric circuit has been shown in Fig. 4.02.

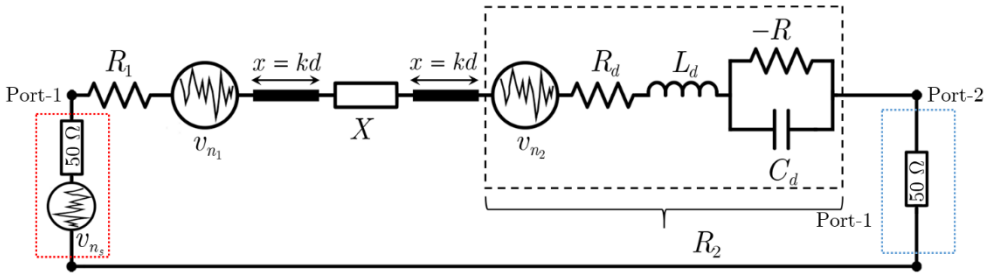

Fig. 4.02. Equivalent noise circuit model of the series PT-symmetric circuit. The ideal negative resistance originates through the tunnel diode and therefore has been replaced by its equivalent noise circuit model.

The loss resistor R_1 and the internal resistance of the tunnel diode R_d are primary sources of the thermal noise voltage. The source port consists of a matched resistance and hence exhibits thermal noise. The noise power at the port-2 of the series PT-symmetric system is given as

$$\overline{v}_{port-2} = \sqrt{4ktB(R_s + R_1 + R_d)}\,\frac{R_{port-2}}{R_1 + R_d + R_{port-2}} \tag{4.1a}$$

Similarly, the noise power at the input port-1 is given as

$$\overline{v}_{port-1} = \sqrt{4ktBR_s}\,\frac{R_{port-2}}{R_1 + R_d + R_{port-2}} \tag{4.1b}$$

The noise figure is the degradation of signal to noise ratio at the output and input, and therefore it can be calculated as

$$F = 10\log_{10}\left(\frac{v_{port-2}}{v_{port-1}}\right) \tag{4.2}$$

For a bandwidth of 1 Hz, solving Eqs. (4.1a), (4.1b) and (4.2) at the exceptional point for $R_1 = R_{port-1} = R_{port-2} = 50\ \Omega$ and $R_d = 7\ \Omega$, the noise figure of the series PT-symmetric system is calculated as 3.31 dB/Hz. The noise figure of the series PT-symmetric circuit can be validated by using a

microwave circuit simulator such as Cadence or Keysight ADS. Fig. 4.03 shows the comparison between simulated and analytical noise figure.

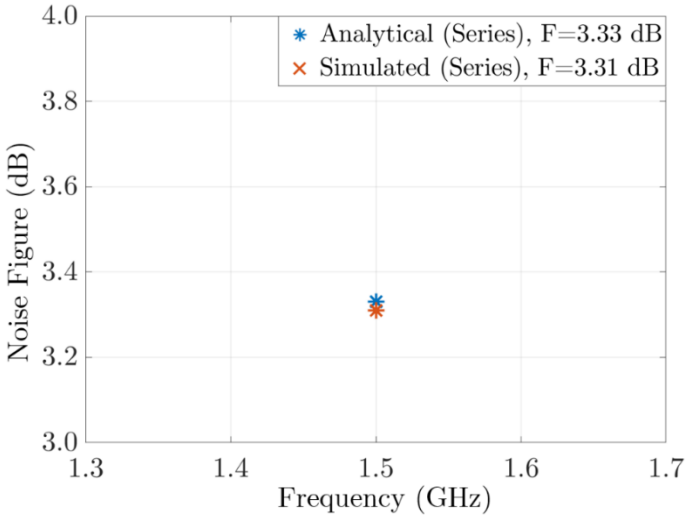

Fig. 4.03. Analytical and simulated noise figure of the PT-symmetric system in series at the exceptional point of $r = 1$. The characteristic line impedance Z_0 is 50 Ω.

4.2 Noise Figure of PT-Symmetric Circuit in Shunt

The noise figure for the shunt circuit topology can be estimated by identifying thermal noise sources in the PT-symmetric circuit. The schematic for an ideal and loss free PT-symmetric circuit from section 3.2 is given as.

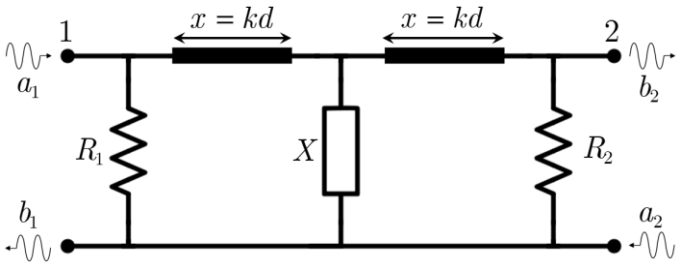

Fig. 4.04. Schematic from section 3.2 of shunt PT-symmetric circuit with ideal lumped elements. The system is assumed to be free from any associated noise and system losses.

We can readily identify and model the thermal noise sources of the system for the conventional resistor $+R$ and the internal resistance of the tunnel diode of sample L939F, which provides negative resistance to reach the exceptional point of the shunt PT-symmetric circuit. It is important to notice that the analytical noise figure estimated here only takes thermal noise voltage into consideration. The overall system noise figure is a superposition of all the noise sources such as thermal, shot and flicker noise originating through active and passive circuit elements.

$$F_{total} = F_{active} + F_{passive} \tag{4.3}$$

However, due to the purpose of brevity, we have only considered the thermal noise in our studies since it is the most dominant noise source in any microwave system.

The equivalent circuit model of a non-ideal PT-symmetric circuit in shunt has been shown in Fig. 4.05.

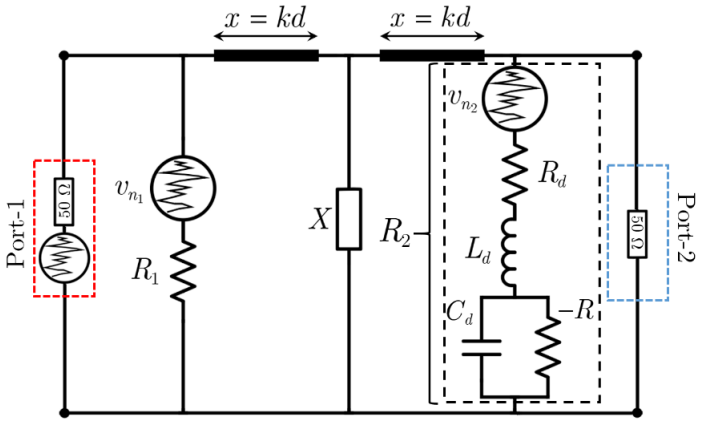

Fig. 4.05. Equivalent noise model of the shunt PT-symmetric circuit. The thermal noise originates through the loss resistor and internal resistance of the tunnel diode which provides a negative resistance of -49.77 Ω.

Since the circuit elements are now in a shunt configuration, the noise voltages at the output and input port are given as

$$\overline{v}_{port-2} = \sqrt{4ktB\left(\frac{1}{R_{port-1}} + \frac{1}{R_1} + \frac{1}{R_d}\right)} \frac{R_{port-2}}{R_{port-1} + R_1 + R_d + R_{port-2}} \tag{4.4a}$$

$$\overline{v}_{port-1} = \sqrt{4ktB \,/\, R_s} \frac{R_{port-2}}{R_{port-1} + R_1 + R_d + R_{port-2}} \tag{4.4b}$$

The noise figure is the degradation of signal to noise ratio at the output and input, and therefore it can be calculated as

$$F = 10\log_{10}\left(\frac{v_{port-2}}{v_{port-1}}\right) \tag{4.5}$$

For a bandwidth of 1 Hz, solving Eqs. (4.4a), (4.4b) and Eq. (4.5) at the exceptional point for $R_1 = R_{port-1} = R_{port-2} = 50\ \Omega$ and $R_d = 7\ \Omega$, the noise figure of the shunt PT-symmetric system is calculated as 9.63 dB/Hz.

The noise figure of the shunt PT-symmetric circuit can be validated by using a microwave circuit simulator such as Cadence or Keysight ADS. Fig. 4.06 shows the simulation and analytical comparison of the noise figure.

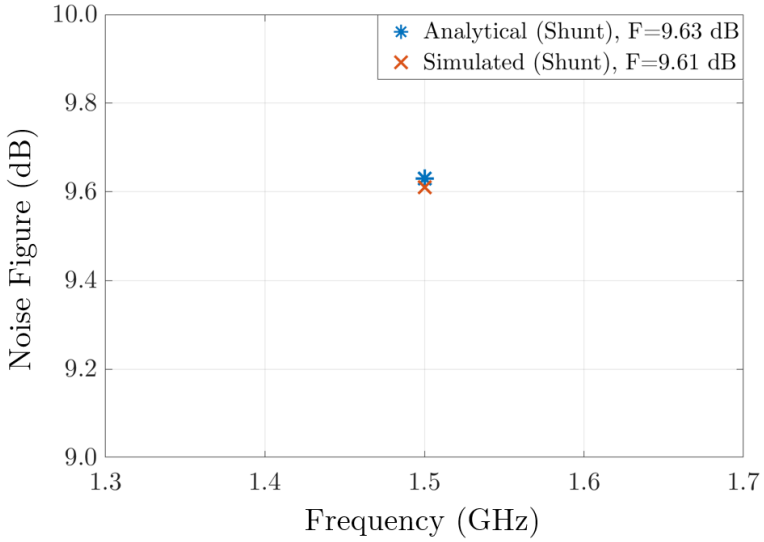

Fig. 4.06. Analytical and simulated noise figure of the PT-symmetric system in shunt configuration at the exceptional point of $r = 1$. The characteristic line impedance Z_0 is 50 Ω.

The above results conclude that the PT-symmetric systems designed in shunt configurations exhibit higher noise figure as compared to the series circuit design. The comparison results provide a valuable insight in designing and implementing functional PT-symmetric devices where the performance is bottlenecked due to high noise figure levels such as RCS reduction and unidirectional invisibility cloaks.

4.3 Summary

PT-symmetric systems are composed of loss (passive) and gain (active) elements that are not ideal and therefore generate noise. Studies have found that noise can weakly break PT-symmetry which results in a system performance degradation. Therefore it is important to characterize such systems in terms of noise figure. The chapter discussed and presented the dominant noise source of PT-symmetric system in series and shunt design configuration. In order to achieve a figure-of-merit, tunnel diode was chosen to provide negative resistance due to the least number of active components and low power consumption, therefore resulting in minimum possible noise figure estimation. The noise characterisation of PT-symmetric system in series and shunt has been performed by considering the most dominant noise source i.e. thermal noise. The noise figure of aforementioned circuit design configurations was performed by using analytical methods whereas further validation was performed using simulation techniques. The chapter showed that PT-symmetric systems and applications designed in series configuration are prone to lower noise figure levels as compared to the shunt variant. The results are particularly useful for PT-symmetric applications where the performance bottlenecked by noise levels. For instance, unidirectional cloaks, sensors, circulators and isolators. Further detailed on the performance of PT-symmetric applications and devices has been performed in the next chapter where the performance of a noisy PT-symmetric cloak has been discussed.

Contribution Overview

- Presented an equivalent noise model of PT-symmetric circuits in series and shunt topologies and evaluated the noise figure in each case using analytical and simulation techniques.

- Investigated and performed a noise figure comparison between series and shunt PT-symmetric circuit configuration.

- Investigated that PT-symmetric circuits designed in series configuration exhibit lower noise figure levels in comparison with shunt design variants. Therefore, PT-symmetric applications such as unidirectional or bidirectional invisibility cloaks that are bottlenecked by high noise figure levels can be designed in series configuration for better performance.

Chapter 5

Noise Performance of PT-Symmetric Applications

5.1 Cloaking and Invisibility Based on PT-Symmetry

Cloaking an object and rendering it undetectable to the incoming waves is among one of the exotic applications of PT-symmetry which has been briefly discussed earlier section of this thesis. Eq. (2.40) from section 2.2.5 presents an important condition which suggests that at the exceptional point, when the transmission is unity, the reflection coefficient from either side of a two-port system should be zero. We can write the condition as

$$S_{11}S_{22}^{*} = 1 - \left|S_{21}\right|^{2}$$

The above condition has been exploited in [26–33] to provide a proof of concept to realize unidirectional invisibility and cloaking by incorporating conjugate PT-symmetric metasurfaces with loss and gain respectively.

In this chapter, we will first review and discuss a unidirectional PT-symmetric cloak under ideal, loss-free conditions which has been studied in [29] to realize a perfect invisibility. We then present a reconfigurable metasurface cloak based on PT-symmetry which can be configured to provide unidirectional or bidirectional cloaking. We then discuss and evaluate the performance of the cloak by estimating the radar cross-section (RCS) of a cloaked target in the presence of various noise levels. In the later part of the chapter, a solid state switch has been presented which can also

be realized as a selective attenuator. The studies performed in this chapter have been validated by using analytical methods and further verified through circuit and full-wave simulation models.

5.1.1 An Ideal Unidirectional PT-Symmetric Cloak

In reference [29] it was proposed that an ideal unidirectional cloak can be realized by loss and gain metasurfaces. The absorbing lossy metasurface intercepts the incoming signal with zero reflections from the incident side whereas the gain metasurface transmits the same signal with equal amplitude and phase on the output.

Consider the schematic shown in Fig. 5.01 where a PEC cylinder has been covered by an ultrathin metasurface with loss and gain respectively. The metasurface is composed of discrete ideal loss (conventional) and gain (negative) resistors connected together through a portion of transmission line. The magnitude of loss and gain resistors are defined in terms of characteristic line impedance Z_0 and the non-Hermiticity parameter r such that

$$R_{loss} = +rZ_0$$

$$R_{gain} = -rZ_0$$

The metasurface is constructed using discrete combination of positive and negative resistors connected together by a transmission line of length $x = kd$ with satisfied PT-symmetry. We also assume that the impedance if the incoming wave is exactly matched with the surface impedance of the lossy metasurface such that there is no scattering or diffraction.

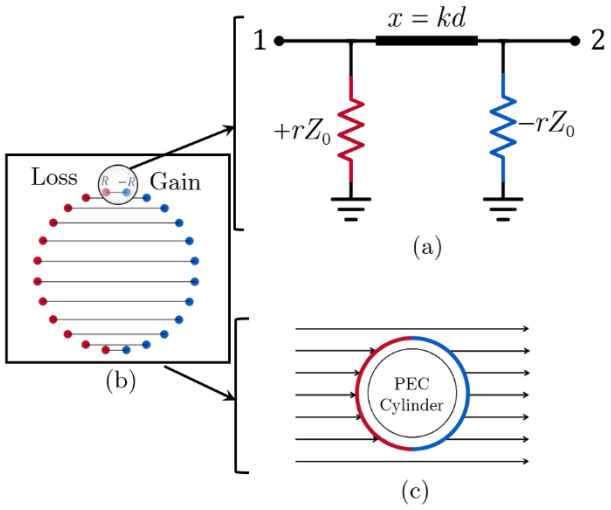

Fig. 5.01. (a) A simple two-port transmission line model of an ideal unidirectional PT-symmetric cloak. (b) The lossy part of metasurface is composed of conventional positive resistors whereas the gain metasurface is composed of negative resistors. The horizontal lines show the connecting transmission lines of different length between the loss and gain resistors with satisfied PT-symmetry at the exception point of $r = 0.5$ (c) The incoming plane wave is transmitted through the PT-symmetric structure rendering it invisible to incoming waves.

The scattering matrix of the schematic shown in Fig. 5.01 is given as

$$S_{11} = \frac{(2r-1)\sin x}{\sin x - 2ir^2 e^{-ix}} \tag{5.1a}$$

$$S_{12} = S_{21} = -\frac{2ir^2 \sin x}{\sin x - 2ir^2 e^{-ix}} \tag{5.1b}$$

$$S_{22} = -\frac{(2r+1)\sin x}{\sin x - 2ir^2 e^{-ix}} \tag{5.1c}$$

Regardless of the electrical line length, the scattering matrix at the exceptional point of $r = 0.5$, can be constructed as

$$S = \begin{pmatrix} 0 & 1 \\ 1 & 4 \end{pmatrix} \tag{5.2}$$

Which shows that any incoming signal impinging at the lossy metasurface will be fully absorbed and transmitted towards gain side. However, an incident signal incident at the gain metasurface is reflected back and amplified by a factor of four. This also means that a radar beam illuminating the metasurface from the loss side will be suppressed to give an overall 99.9% RCS reduction. However, the RCS estimation will be very high if the cloaked target is illuminated from the gain part of the metasurface. The large scattering energy originates from the active metasurface resulting in a high RCS. Since the aforementioned cloak exhibits unidirectional properties, it is primarily useful in monostatic radar applications. The analysis shows that the unidirectional behaviour of the PT-symmetric cloak is based on loss and gain metasurfaces because the reflection coefficient is zero from the lossy side of the structure whereas enhanced reflection and scattering is observed from the gain side.

5.1.2 A Reconfigurable Cloak Based on PT-Symmetry

In previous chapter, we have discussed the properties of a unidirectional cloak and its equivalent circuit model. In this section we will discuss an ideal reconfigurable cloak based on PT-symmetric metasurfaces. The metasurface cloak has been presented in terms of its equivalent circuit model and full-wave electromagnetic simulation studies.

Consider Fig. 5.02 where an uncloaked target is being illuminated by the incident electromagnetic wave. We assume that the target is in the far-field region where the incoming wave from a radar antenna can be assumed as a plane wave through plane wave approximation expression [80–81].

$$R = \frac{2D^2}{\lambda} \tag{5.3}$$

Here, R is the distance where the spherical wave can be considered as a plane wave, D is the maximum effective diameter of the antenna and λ is the wavelength.

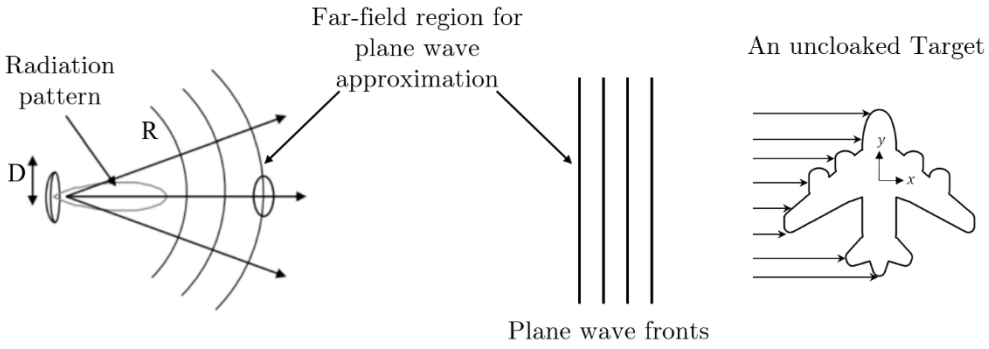

Fig. 5.02. An uncloaked target being illuminated by incident waves from a radar antenna. The target gets reflects the incident electromagnetic waves and gets detected by its radar cross-section approximation.

When an object is illuminated by an electromagnetic wave, it disperses the impinging electromagnetic energy in all directions which is commonly known as scattering. The resulting field distribution in space is dependent upon the object size, shape, composite materials, incident waveform and direction-of-arrival of the incident wave. The spatial distribution of the scattered energy is known as radar cross-section.

The RCS is given in terms of incident and scattered energy from the target calculated as [80]

$$\sigma = \lim_{r\to\infty} 4\pi r^2 \frac{\left|E_s\right|^2}{\left|E_i\right|^2} \tag{5.4}$$

where,

σ = Radar cross-section in [dB/m^2].

E_s = Scattered electric field intensity in [V/m].

E_i = Incident electric field intensity in [V/m].

In order to have an insight of this phenomenon, we have performed a full-wave electromagnetic simulation using COMSOL Multiphysics RF module, the geometric simulation setup has been shown in Fig. 5.03. The simulation domain dimensions are chosen carefully such that they are not too large to cause out-of-memory errors or long computation times, neither too small to cause inaccuracy of the results.

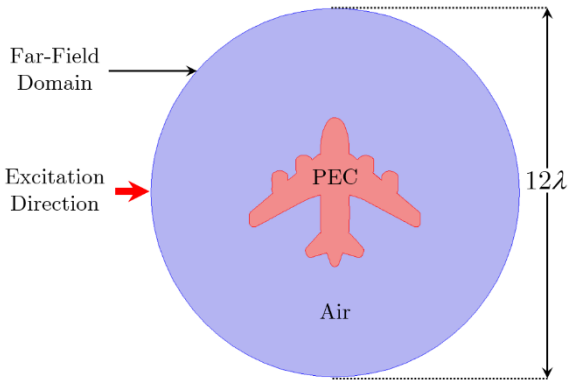

Fig. 5.03. Full-wave simulation setup for system shown in Fig. 5.02. The red arrow represents the excitation direction.

Fig. 5.04 shows the time-snapshot of the full-wave electromagnetic simulation of a plane wave with a magnitude of 1 V/m, incident at the uncloaked target along with its RCS approximation normalized to unit length.

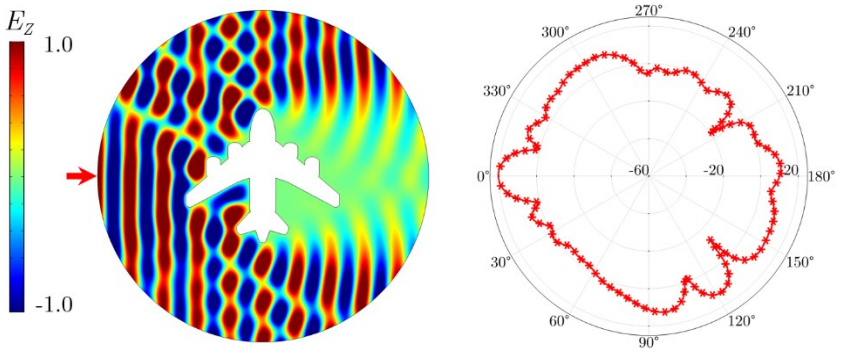

Fig. 5.04. An uncloaked target being illuminated by a plane wave incident from the left. The detection is caused due to the large RCS approximation caused by the scattered electric field distribution and the target's shadow on the right. The red arrow represents the direction of the incident wave. The electric field shown is a time snapshot whereas the RCS calculation is an average value.

We have discussed in section 3 and section 3.2 that the inclusion of an imaginary impedance in series or shunt configurations offers a unique manipulation of the reflection coefficient from the gain side provided that the electrical length is selected such that $x = n\pi / 2$ where n=1, 3, 5.... The scattering matrix of such PT-symmetric circuits in series and shunt were calculated as shown in Eq. (5.5) and Eq. (5.6) respectively.

$$S = \begin{pmatrix} 0 & 1 \\ 1 & 2Z_0 / X \end{pmatrix} \tag{5.5}$$

$$S = \begin{pmatrix} 0 & 1 \\ 1 & 2X / Z_0 \end{pmatrix} \tag{5.6}$$

where X is the imaginary impedance originating through capacitive or inductive element.

Using results from section 3 and section 3.2, PT-symmetric cloak is constructed as an ultrathin metasurface layer as shown in Fig. 5.5. The metasurfaces are modelled as positive (loss) and negative (gain) resistors

connected through a transmission line and separated by a reactive element as followed by the schematic shown in Fig. 3.01.

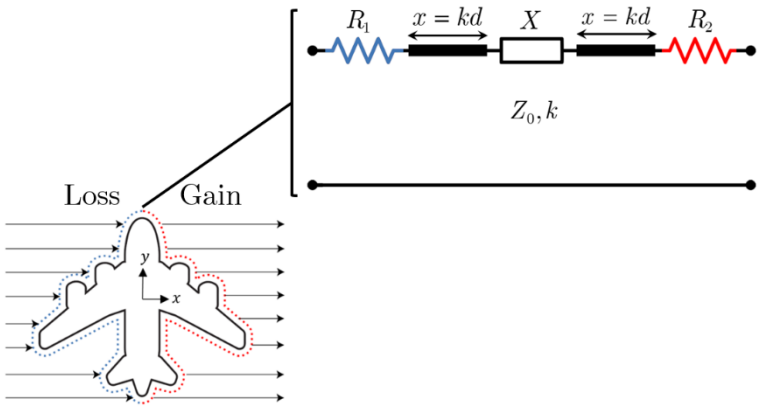

Fig. 5.5. PT-symmetric metasurface constructed from a series PT-symmetric circuit configuration. The reactive element X has a complex impedance originating through a capacitor or an inductor.

The PT-symmetric metasurface can also be constructed by using shunt PT-symmetric configuration by following results from section 3.2 and Fig. 3.07. This schematic has been shown in Fig. 5.6.

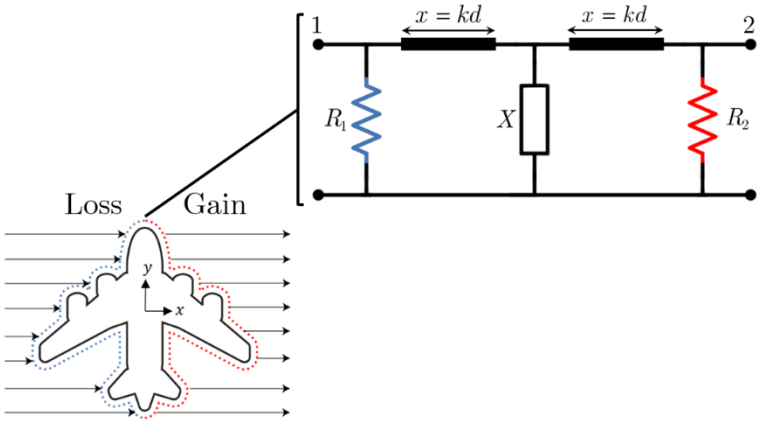

Fig. 5.6. PT-symmetric metasurface constructed from a shunt PT-symmetric circuit configuration.

In order to have further understanding of the concept, we have performed full-wave electromagnetic simulations for an incident plane wave on the PT-symmetric cloaking metasurfaces. Fig. 5.07 shows the setup configuration.

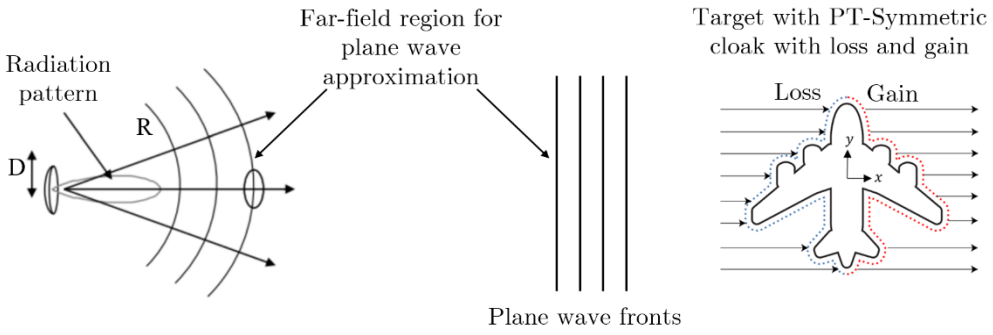

Fig. 5.07. A PT-symmetric cloaked target with loss (blue) and gain (red) is been shown which is at a sufficient distance from the radar antenna such that the incoming wave can be considered as a plane wave.

The geometric setup for the full-wave simulation has been shown below in Fig. 5.08.

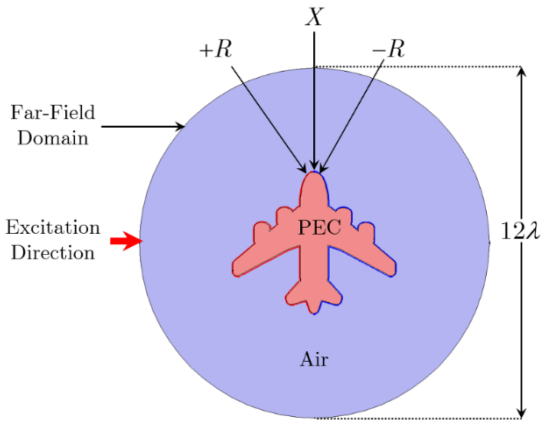

Fig. 5.08. Simulation setup for the full-wave electromagnetic simulation for the system shown in Fig. 5.07.

The structure is excited by a plane wave, incident from the left on the loss metasurface connected in series with the lumped reactance and the gain metasurface. The magnitude of the loss resistance, reactance and the gain resistance is given as

$$R_1 = +rZ_0$$

$$R_2 = -rZ_0$$

And $X = 1/j\omega C$ or $X = 1/j\omega C$ for a series capacitive or series inductive element respectively.

The radar cross-section scattering is evaluated in the far-field domain and is an average value of scattered electric-field measured at various angles over 360 degrees. Similar procedures is to be followed for an excitation from the gain side with an appropriate capacitance or inductance value. The equivalent transmission line schematic has been shown in Fig. 5.5 Fig. 5.6 for series and shunt configuration respectively.

Fig. 5.09(a) shows that perfect invisibility is observed when the structure is illuminated from the loss side and the targets RCS is suppressed by a factor of 99.9% which approximates to -60 dB per unit length. The lossy metasurface resistors absorbs the incoming signal with zero reflection, whereas the gain metasurface transmits the incident signal with similar amplitude and phase on the output.

Similarly, by illuminating the structure from the gain side and utilizing a series capacitance of 200 pF or series inductance of 1 pH, bidirectional performance of the metasurface cloak is observed. Similar results can be obtained by using shunt PT-symmetric circuit topology with a capacitance of 1 fF or an inductance of 200 nH.

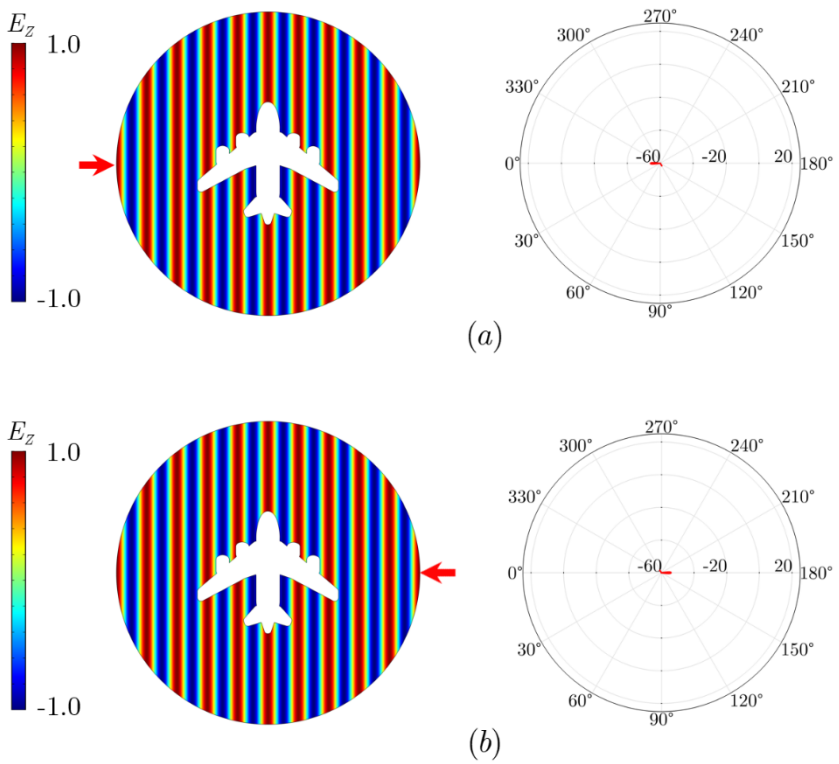

Fig. 5.09. (a) Time snapshot of the PT-symmetric metasurface showing that an illumination from the loss side exhibits perfect invisibility under ideal, loss-free conditions. (b) Time snapshot of the PT-Symmetric metasurface showing that the structure illumination from the gain side with an appropriate series or shunt reactance results in bidirectional invisibility. The RCS is an independent value with respect to time and is averaged for incident and scattered electric fields over 360 degrees.

5.2 Noise Performance and Detection of a PT-Symmetric Cloak

Inclusion of noise in any RF system not only degrades the performance but can also causes system instabilities and can render it internally or externally noise limited. A study in [17, 37, 82] found that thermal noise inclusions in

a PT-symmetric system results in a weakly broken PT-symmetry hence degrading the cloaking performance and resulting in an increased RCS of the target. Since PT-symmetric systems utilize active and passive circuit elements that generate various noise types due to which the cloaking achieved by such a metasurface cannot be noise free.

In section 5.1.1 we have discussed and visualized that a PT-symmetric cloak with balanced loss and gain metasurfaces can potentially achieve perfect unidirectional or bidirectional invisibility under ideal loss-free and noiseless conditions. The lossy metasurface fully absorbs the incoming signal by the concept of impedance matching and the gain surface emits the signal with similar amplitude and phase rendering the object undetected. The RCS of a cloaked target was found to be reduced by a factor of 99.9% to that of uncloaked target.

We have presented equivalent noise circuit models of PT-symmetric systems and calculated the noise figure levels of series and shunt configurations in chapter 4. Here, we will utilize these results and benchmark the performance of a PT-symmetric cloak in realistic domains such as in the presence of noise. A realistic PT-symmetric cloak cannot be implemented as noise free. This is because the cloaking metasurfaces are composed of non-ideal active and passive circuit elements, therefore the cloaking structure exhibits thermal, shot and flicker noise contributions. The research studies presented in this chapter only accounts for the thermal noise in the cloaking performance estimation because it is the most dominant noise source. For the gain metasurface noise calculations, we have chosen a tunnel diode because not only it exhibits the least amount of active circuit elements but also consumes very low power.

The lossy part of metasurface is realized through passive resistive elements that are a source of added thermal noise. The noisy surface current density of the lossy metasurface can be written as a sum of noiseless surface current density and equivalent noise current density as

$$J_{loss} = J_{noiseless} + J_{n(passive)} \tag{5.5a}$$

Similarly, the gain metasurface is realized through RTD which will have active noise and the surface current density of a noisy gain metasurface can be written as

$$J_{gain} = J_{noiseless} + J_{n(active)} \tag{5.5b}$$

where $J_{n(passive)}$ and $J_{n(active)}$ are the noise current densities of loss and gain metasurface respectively.

The equivalent noise current densities are calculated from thermal noise current which is given by [46]

$$\overline{i}_{rms}^{2} = 4kTB / R \tag{5.6}$$

It is to be noted that Eq. (5.6) provides the root mean square (rms) noise current, and because the thermal noise current is random and exhibits a Gaussian distribution therefore instantaneous peak noise current would be within six times the rms value for more than 99% of the time. The noise current waveform in time-domain with its statistical distribution has been shown in Fig. 5.10. For the purpose of brevity, we have considered only the thermal noise sources in our calculations since it is the most dominant noise source present in the system. However, modelling of other noise sources such as shot noise and flicker noise requires further consideration and the noise figure is expected to increase with inclusion of such sources.

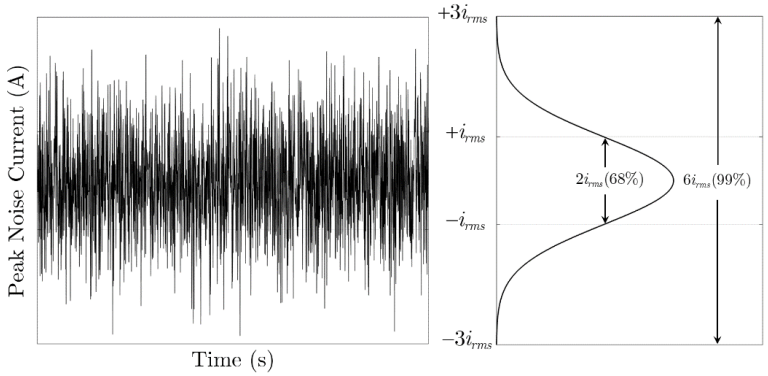

Fig. 5.10. The thermal noise current has random Gaussian distribution with a range equal to peak noise current. The probability of finding the peak noise current at any instance of time would be 99% if it is six times of root mean square noise current. Therefore $i_p = 6i_{rms}$.

The noise current density is then found by following Eq. (5.7).

$$J_n(t) = \frac{1}{i_p\sqrt{2\pi l}} \exp\left(-\frac{t^2}{2i_p^2}\right) \tag{5.7}$$

where l is the length of the individual metasurface and i_p is the peak noise current given by $i_p = 6i_{rms}$.

Using results from section 4.2 and utilizing shunt configuration from schematic shown in Fig. 4.04, the noise figure of the cloaking metasurface was estimated to be 9.61 dB/Hz. Similarly, following a series configuration, the noise figure of the metasurface was estimated to be 3.31 dB/Hz.
Fig. 5.11 shows a comparison of the simulated noise figure by following shunt and series PT-symmetric circuit configuration.

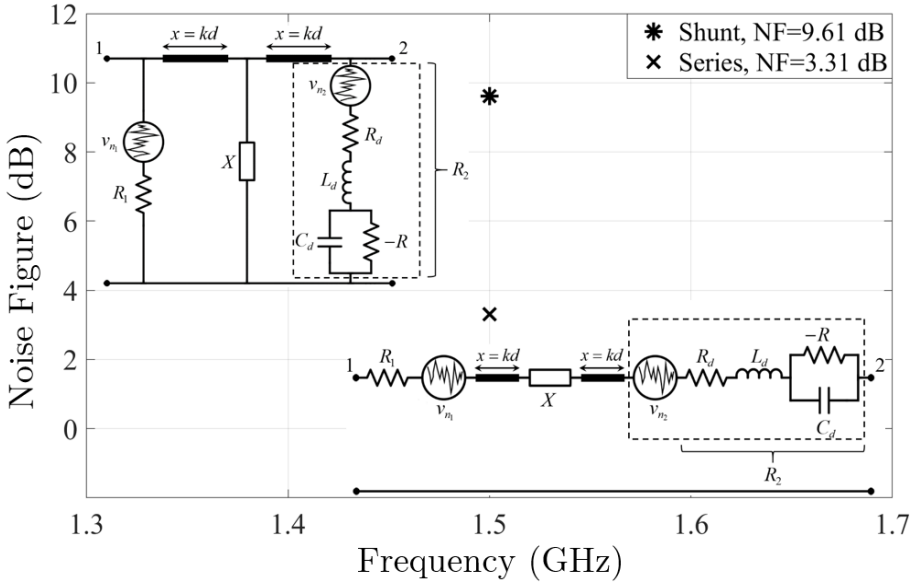

Fig. 5.11. Noise figure for PT-symetric circuits in both shunt and series configurations. The negative resistor of -49.77 Ω originates through resonant tunnel diode of sample L939F with an internal resistance of 7 Ω at a biasing voltage of 2.65 volts at 1.5 GHz.

Formulating the above results and including a noise figure of 3.31 dB per Hz of bandwidth, the RCS of the cloaked target was found to be at -30 dB/m which is 30 dB higher as compared with an ideal and noise-free cloak. Fig. 5.12(c) and Fig. 5.12(f) show the cloaking performance of a cloak with 3.31 dB of noise figure. Similarly, utilizing a shunt circuit configuration with a noise figure of 9.61 dB the performance of the metasurface cloak was found to be further degraded with RCS approximation of -10 dB/m. The effect has been shown in Fig. 5.12(d) and Fig. 5.12(f). A further increase in noise levels with a high noise figure of 20 dB, the cloaking performance is severely degraded and the RCS is further increased to 20 dB/m.

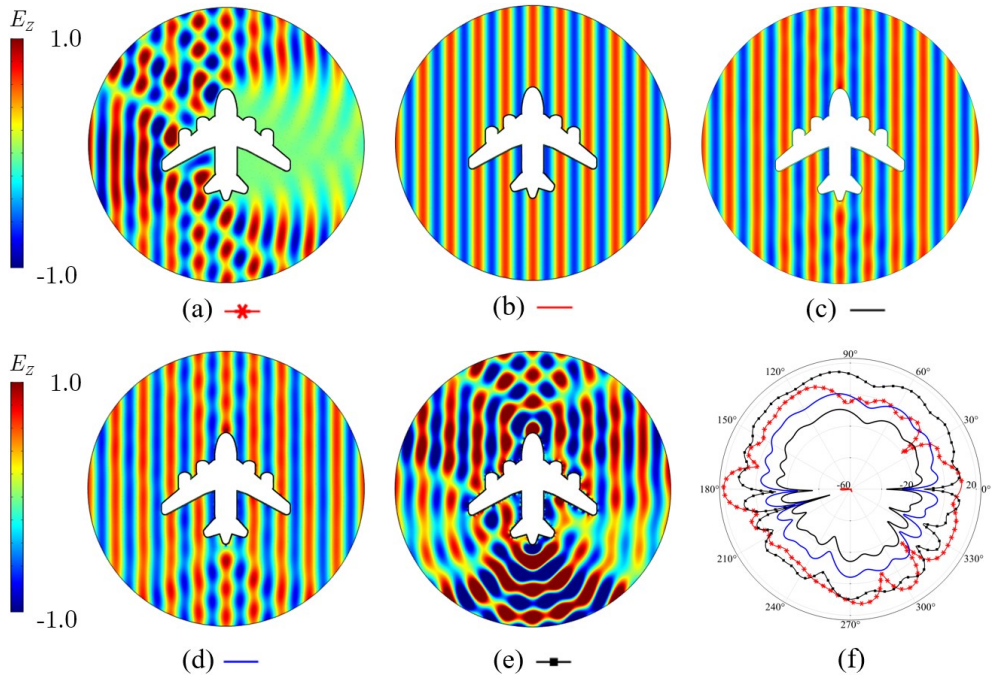

Fig. 5.12. Time snapshot for; (a) An uncloaked target being detected by its RCS approximation and scattered field distribution. (b) A noise-free PT-symmetric metasurface cloak renders the target invisible by reducing its RCS to an extremely low value of -60 dB per unit length under ideal conditions. (c) Using a metasurface cloak with series PT-symmetric circuit topology exhibits a noise figure level of 3.31 dB, the RCS is increased to -30 dB per unit length. (d) Using a metasurface cloak by following shunt circuit configuration the noise figure approximates to 9.7 dB with an RCS of -10 dB/m. (e) A noise figure level of 20 dB significantly degrades the cloaking performance to a level where the RCS estimation from an uncloaked and cloaked target are comparable. The RCS approximation is an time-independent value which is averaged for 360 degrees incident and scattered electric fields.

Our research studies have explained that the cloaking achieved by such a noisy cloak is imperfect and it is evident that while a PT-symmetric cloak

is be able to reduce the RCS of the target, a perfect invisibility is never achieved. Further, the receiver sensitivity is also important because it will ultimately determine the minimum detection threshold. For instance, a receiver sensitivity may be low enough to a certain level where 9.6 dB of noise figure does not potentially causes detection. On the contrary, a receiver with high receive sensitivity may cause detection at same noise figure.

The noise in PT-symmetric metasurface primarily originates through loss and gain resistors. Thermal noise from the passive lossy resistor is fixed however the gain resistor requires further attention. The noise originating through the gain resistor depends on the implementation technique such as by the means of operational amplifier, resonant tunnel diode (RTD) or a transistor based negative impedance converter. For the purpose of simplicity, we have considered the equivalent RTD noise model and thermal noise to calculate the overall noise figure of the metasurface in series and shunt design configurations. However, with the inclusion of other noise sources such as shot noise or flicker noise and complex NIC models with greater number of active and passive components, the noise figure is expected to increase. The noise analysis of NIC and non-Foster loaded metamaterials was studied in [83] where noise figure of an actively loaded loop was estimated. However, the noise figure can be significantly reduced by using careful circuit design considerations. For instance, by utilizing the series circuit topology, the noise figure can be greatly reduced in comparison with shunt circuit design configuration.

5.3 An Electromagnetic Switch Based on PT-Symmetry

The PT-symmetric systems explained in Fig. 3.01 and Fig. 3 in series and shunt domains showed that a capacitive or inductive impedance can yield broad range of output reflection magnitude at an electrical length of $x = n\pi / 2$ where n is an odd integer multiplier. This is potentially favorable for the design applications of reconfigurable unidirectional cloaks or unidirectional transmission devices where the input port is perfectly matched with zero reflection and unity transmission towards port-2 with an output reflection coefficient defined by specific capacitance or inductance.

However, it is noticeable that if an electrical line length is chosen such that $x = n\pi$ where $n = 1,\ 2,\ 3...$ the scattering parameters for the series PT-symmetric system shown in Fig. 3.01 are now given as

$$S_{11} = S_{22} = \frac{1}{1 + \dfrac{2Z_0}{X}} \tag{5.8a}$$

$$S_{12} = S_{21} = \frac{1}{1 + \dfrac{X}{2Z_0}} \tag{5.8b}$$

Similarly, the scattering parameters for the shunt PT-symmetric circuit are now given as

$$S_{11} = S_{22} = \frac{1}{1 + \dfrac{2X}{Z_0}} \tag{5.9a}$$

$$S_{11} = S_{21} = \frac{1}{1 + \dfrac{Z_0}{2X}} \tag{5.9b}$$

Following Eqs. (5.8a)-(5.9b), it implies that each scattering parameter of the PT-symmetric circuits in series and shunt can be manipulated through the choice of an appropriate imaginary impedance through a capacitive or inductive element. The proposed PT-symmetric circuits in series and shunt can behave as an attenuator or a switch which are useful in applications in which signal transmission is required to be manipulated.

For instance, with a small capacitance of 0.1 pF, the PT-symmetric system in series exhibits full reflection at input and output port with approximately zero transmission at a frequency of 1.5 GHz. The scattering matrix obtained with an electrical length of $x = n\pi$ and a series capacitance of 0.1 pF or a series inductance of 113 nH is constructed as follows for an OFF state of the switch.

$$S = \begin{pmatrix} 0.996 & 0.094 \\ 0.094 & 0.996 \end{pmatrix} \tag{5.10a}$$

Similarly, at a series capacitance of 20 pF or a series inductance of 0.56 nH, the PT-symmetric system shows near unity transmission to port-2 and zero input and output reflection magnitude showing an ON state. The scattering matrix obtained is given as

$$S = \begin{pmatrix} 0.053 & 0.999 \\ 0.999 & 0.053 \end{pmatrix} \tag{5.10b}$$

Similarly, by following a shunt PT-symmetric circuit design configuration and having a capacitance of 45 pF or an inductance of 0.23 nH the OFF state is observed with scattering matrix given as

$$S = \begin{pmatrix} 0.996 & 0.094 \\ 0.094 & 0.996 \end{pmatrix} \tag{5.11a}$$

For an ON state, the shunt capacitance and inductance are given as 0.1 pF and 50 nH respectively, with a scattering matrix given as

$$S = \begin{pmatrix} 0.053 & 0.999 \\ 0.999 & 0.053 \end{pmatrix} \tag{5.11b}$$

A full-wave electromagnetic simulation using COMSOL Multiphysics 5.4 validates the potential of the PT-symmetric circuits to behave as switching or an attenuating device. For instance, Fig. 5.13 shows the incident electromagnetic wave on the PT-symmetric system designed in shunt configuration showing a full-transmission to port-2 with zero input reflections. The positive, negative and imaginary impedances have been modelled as an ultrathin metasurfaces.

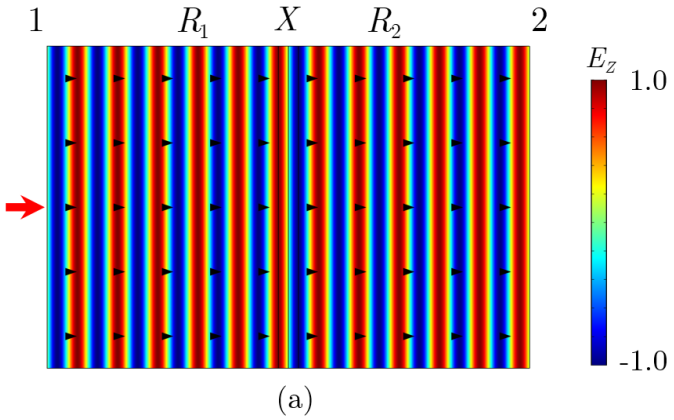

(a)

Fig. 5.13. Time snapshot of the full-wave electromagnetic simulation in ON state. A capacitance of 0.01 pF the system experiences zero reflections at input and output ports and a unity transmission towards port-2. The red arrow shows the excitation direction whereas the black arrows represent the average power flow in the system towards port-2.

On the contrary, Fig. 5.14 shows that at a selected capacitance of 20 pF, the system shows full reflection at port-1 with a transmission magnitude of 0, therefore representing an OFF state. Since PT-symmetric systems are invariant under combined parity and time-reversal operations, the following energy conservation relationship is satisfied [84].

$$S_{11}S_{22}^{*} = 1 - \left|S_{21}\right|^{2} \tag{5.12}$$

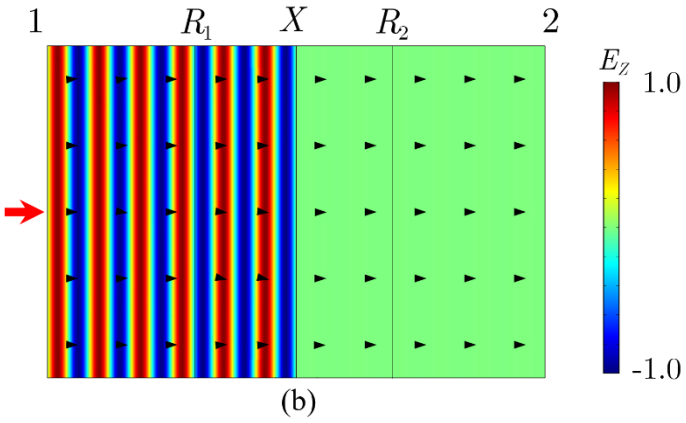

Fig. 5.14. Time snapshot of a full-wave electromagnetic simulation in OFF state. At a capacitance of 20 pF the system experiences unity input reflection and zero transmission towards port-2. The system has been configured using a shunt configuration however similar results can be obtained by following a series design or appropriate inductance range.

5.4 Summary

The chapter first reviewed the performance of an ideal metasurface cloak based on loss and gain which is able to provide ideal unidirectional invisibility under loss and noise-free domains. The chapter then presents a reconfigurable cloaking model based on loss, gain and an imaginary

impedance metasurface. The cloaking model can be configured to provide unidirectional or bidirectional invisibility, based on the choice of imaginary impedance, in series and shunt circuit design topology. The chapter further elaborates that an ideal cloaking performance is never achieved in the presence of dominant noise source such as thermal noise. For this purpose, the performance of a unidirectional cloak was simulated in the presence of various noise figure levels and RCS was calculated and compared with ideal noise-free scenario.

Further studies showed that the electrical line length plays a crucial role in PT-symmetric application design. For instance, an electrical length of $n\pi/2$ where n is an odd multiplier, the output reflection coefficient magnitude of the PT-symmetric circuit is defined by the imaginary capacitive or inductive impedance. The application is particularly useful for unidirectional or bidirectional cloaking purposes where output reflection is required to be maintained.

Similarly, at an electrical length of $n\pi$ where n is an integer multiplier, both the reflection and transmission properties of PT-symmetric system can be manipulated through the capacitive or inductive impedances. This is particularly useful for applications that require switching, filtering or attenuation. The aforementioned studies have been verified analytically and the transmission and reflection behavior is visualized by a full-wave circuit simulation models in both series and shunt configurations. Further, we have shown that the PT-symmetric systems are prone to high noise figure levels however careful design techniques can reduce the noise figure with some application limitations. For instance, a unidirectional cloak in shunt circuit configuration has higher noise figure as compared to series variant. Finally, we have performed noise modeling of the cloaking metasurface and discussed

the performance of a noisy PT-symmetric cloak and concluded that the noise degrades the cloaking performance and effectively increases the scattering cross-section of the cloaked object and in such circumstances where noise figure is sufficiently high, the system may get internally noise limited.

Contribution Overview

- Estimated the performance of an ideal metasurface cloak based on loss and gain which is able to provide ideal unidirectional invisibility under loss and noise-free domains.
- Presented an ideal reconfigurable cloaking model with bidirectional cloaking properties and investigated its performance in terms of radar cross-section under loss and noise-free domains.
- Proposed the equivalent noise model of the metasurface cloak and estimated the performance of a noisy cloak under realistic domains with various noise figure levels, and estimated the radar cross-section in each case. Also described the minimum receiver's threshold that may cause detection of the cloaked target in the presence of noise.
- Proposed an electromagnetic switch with high isolation, based on PT-symmetry and estimated the noise figure in series and shunt configurations.

Chapter 6

Gain Implementation in PT-Symmetric Circuits and Potential Applications of Negative Impedance Structures

6.1 Experimental Model of a PT-Symmetric Circuit

Practical and stable negative impedance converter is the key requirement in the realisation of a practical PT-symmetric system. A negative impedance may originate through the BJTs or operational amplifiers which incorporate a feedback loop hence stability can be a potential constraint. Another way to realise negative impedance with least number of active elements, is through a tunnel diode. By keeping a specified forward biasing voltage, the tunnel diode can be driven within the negative differential region to provide a negative resistance.

Since the primary purpose of this research study is to have clear understanding of the practical PT-symmetric systems operating at microwave frequency ranges and the associated noise performance, the tunnel diode and operational-amplifier based NIC techniques are most suitable. The primary reason for this choice is that a resonant tunnel diode is capable of operating at frequency ranges of up to several GHz while sustaining stability and utilising very low power. This choice enables to

develop an experimental figure of merit in terms of achieving minimum possible noise figure in PT-symmetric systems due to low thermal and shot noise contributions. Similarly, modern operational amplifiers are capable of maintaining fixed gain at wide microwave frequency ranges, therefore practical design of a wide band PT-symmetric system may be possible [85]. In this section, we have outlined the ongoing research efforts and practical experimentation to realise a functional gain element to be incorporated in a PT-symmetric system operating at microwave frequency ranges.

6.1.1 Gain Element by Using a Tunnel Diode

The working principle of a tunnel diode has been previously discussed in section 2.2.9(c). The current (I) and voltage (V) relationship of the tunnel diode otherwise known as I-V characteristics, is an important first step that can be further explored for the magnitude and stability of the negative impedance. An equivalent circuit model of a tunnel diode has been shown in Fig. 6.01. For this purpose, we have used General Electric's TD261A tunnel diode which exhibits a series resistance $R_s = 7\ \Omega$, series inductance $L_s = 1.5$ nH, shunt capacitance $C_d = 0.65$ pF and a pure negative resistance R_d which is dependent on the biasing conditions.

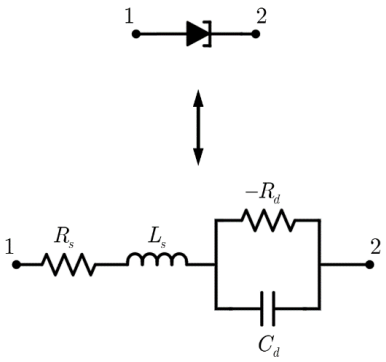

Fig. 6.01. An equivalent circuit model of a tunnel diode with parasitics and a pure negative resistance provided by the diode itself in the negative differential region.

We can follow from Fig. 6.01 that the negative resistance is an internal parameter of the tunnel diode and therefore it is not possible to have a direct measurement of its magnitude. For this purpose, an accurate and precise DC characteristic relationship between voltage and current must be measured. For this purpose we have used Keysight B2912A high precision source measurement unit (SMU) which is capable to source as well as measure current and voltages with a precision accuracy of 10 fA and 100 nV respectively [86]. The measurement setup block diagram has been shown in Fig. 6.02.

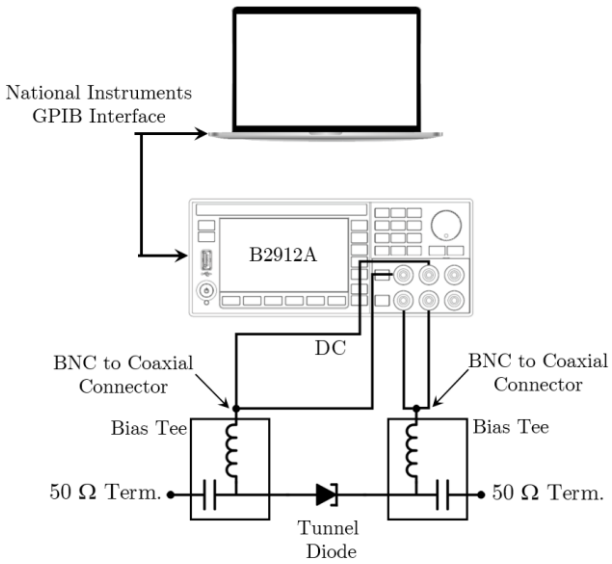

Fig. 6.02. Tunnel diode IV characteristics measurement setup using Keysight B2912A commanded through MATLAB. The diode bias voltage is precisely swept and the current measurement is recorded. The input and output RF ports have been terminated to 50 Ω.

The B2912A can be configured to take automated measurements through MATLAB equipment automation and control toolbox and control script through National Instruments GPIB interface to obtain voltage-current relationship of the tunnel diode. The tunnel diode is connected through a

bias-tee and the RF input and output ports are terminated to 50 Ohms. The DC voltage is then swept in small iterations to obtain the voltage derivate with respect to the current to achieve the biasing point at the resistance of -50 Ohms.

The biasing voltage is swept within an operating range of the tunnel diode i.e. between $0 - 0.6$ volts and by recording the current across the diode, the negative resistance region is determined with an accuracy of up to 100 nV. Fig. 6.03 shows the actual photograph of the measurement setup for tunnel diode DC characteristics.

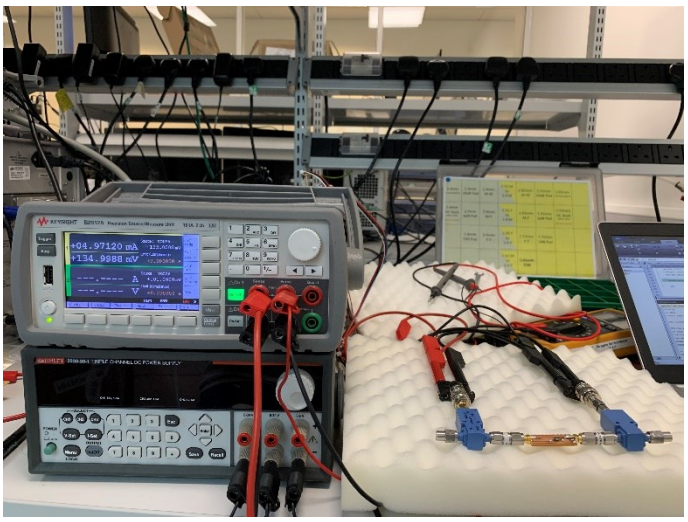

Fig. 6.03. Photograph of the actual measurement setup for DC characteristics of the tunnel diode by using Keysight B2912A and MATLAB.

When the diode is forward biased, the forward current through it increases as the biasing voltage is increased until the peak current is reached to a value of 5.22 mA at a biasing voltage of 0.08 mV. By further increasing the biasing voltage the forward current decreases rapidly and the negative differential region is observed. By calculating the slope at a specific voltage-

current point, negative resistance can be calculated. The diode provides a negative resistance of 50.1 Ω at a biasing voltage of 0.191 mV which is very close to reach the exceptional point of $r = 1$ as discussed in the section 3 and 3.2 for series and shunt PT-symmetric system implementation. The measured DC curve for the tunnel diode has been shown in Fig. 6.04.

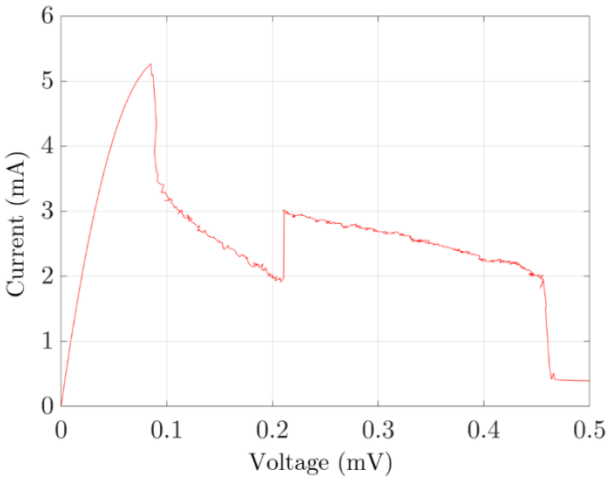

Fig. 6.04. The measured voltage-current curve of the diode. The diode provides a negative resistance of -50.1 Ω at a biasing voltage of 0.191 mV.

6.1.2 Gain Element by Using Operational Amplifier

Another way of realizing negative impedance is through the current inversion technique by using low cost, off-the-shelf operational amplifiers. The working principle of the operational amplifiers based negative impedance converters have been discussed in detail in section 2.2.9(b). The Texas Instruments THS4303 is a wide-band operational amplifier exhibiting fixed gain with low noise at an operating frequency range of up to 10 GHz [85]. The schematic diagram and pin configuration of the aforementioned op-amp has been shown in Fig. 6.05.

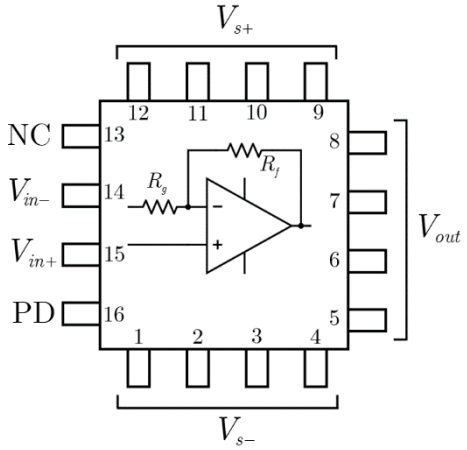

Fig. 6.05. Schematic diagram for Texas Instruments THS4303 wideband operational amplifier.

The PT-symmetric circuit in shunt shown in Fig. 3.07 has a grounded 1-port negative resistor. The equivalent configuration for a grounded negative resistor using the aforementioned op-amp has been shown in Fig. 6.06.

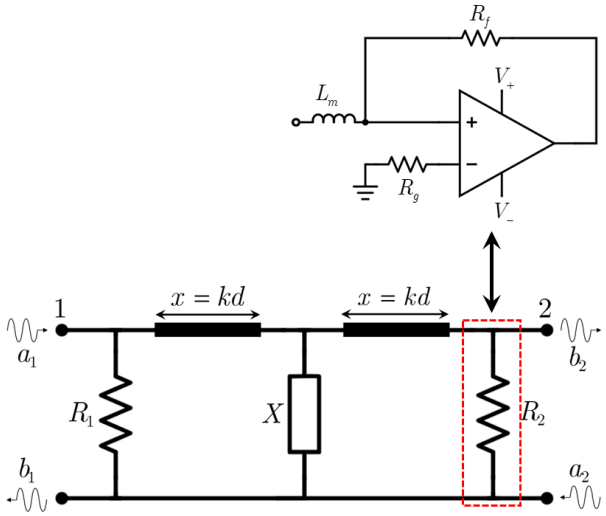

Fig. 6.06. One-port grounded negative resistance using THS4303 operational amplifier. This op-amp based design is suitable for PT-symmetric circuits designed in shunt configurations.

An external feedback network is added such that impedance of -50 Ω is realised at the frequency of 1.5 GHz, whereas the series inductor is included in the system to cancel the imaginary part of the input impedance provided

by the op-amp such that the magnitude of the negative impedance is purely real. The input impedance of a one-port grounded negative impedance converter by using THS4303 can be simulated from the measured data by using a commercial microwave circuit simulator such as Keysight ADS. The simulation setup has been shown in Fig. 6.07 with the input impedance plot being shown in Fig. 6.08. The operational amplifier provides a resistance of approximately -50 Ω at matching frequency of 1.5 GHz.

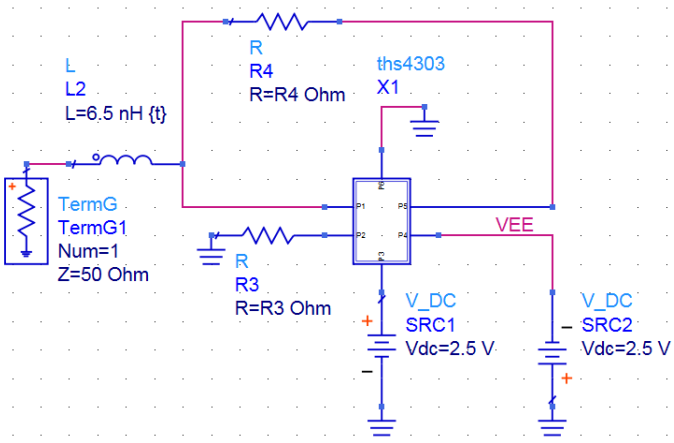

Fig. 6.07. Simulation setup of a one-port grounded negative resistor using Texas Instruments THS4303 operational amplifier.

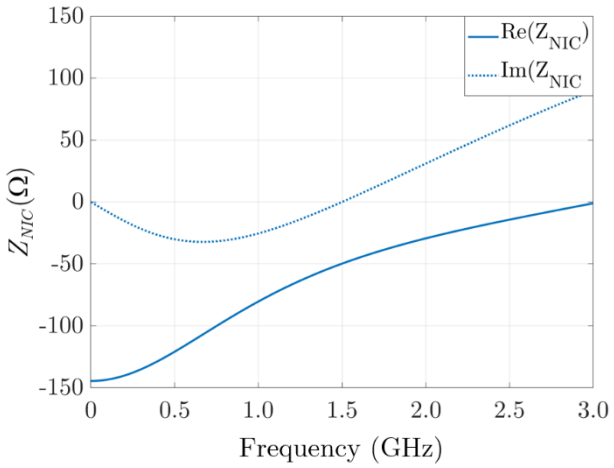

Fig. 6.08. Input impedance of the one-port grounded negative resistance using THS4303 operational amplifier.

Similarly, the design of a floating two-port negative resistor is obtained by cross-coupling the operational amplifiers inverting inputs. Fig. 6.09 shows the schematic diagram of a floating two-port negative resistor.

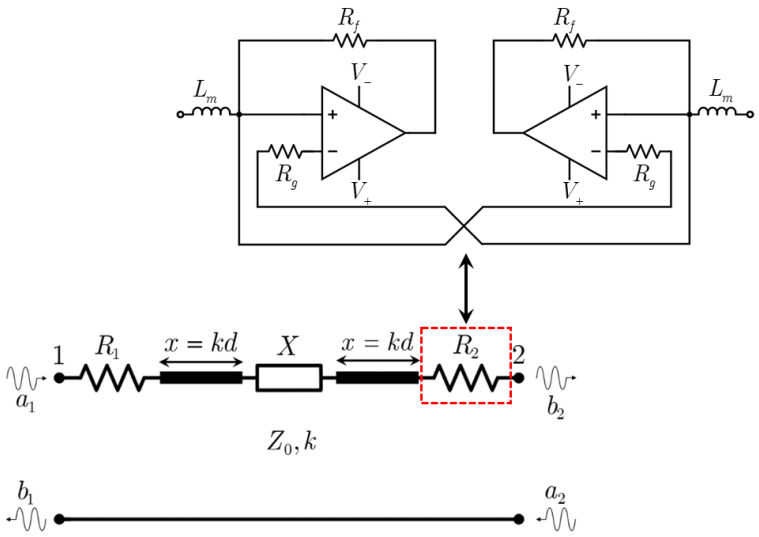

Fig. 6.09. Schematic of a floating two-port negative impedance converter circuit using two cross-coupled THS4303 operational amplifiers. The inductors at the two terminals are responsible to negate the imaginary part of the input impedance given by the NIC.

The two-port floating negative resistor design is well-suited for the PT-symmetric systems designed in series configurations because it satisfies the following reciprocity condition [46].

$$\mathrm{Re}\left(-\frac{1}{Y(2,1)}\right) = \mathrm{Re}\left(-\frac{1}{Y(1,2)}\right) \tag{6.1}$$

The two-port floating negative resistor based on operational-amplifier was simulated using Keysight ADS. The schematic setup of the aforementioned NIC design simulation using the THS4303 operational amplifier has been

shown in Fig. 6.10. The two inductors at the input and output terminals negate the imaginary part of the NIC to effectively provide a real negative impedance across the floating terminals between port-1 and port-2 at broadband microwave frequency ranges. The impedance provided by the floating NIC design has been shown in Fig. 6.11.

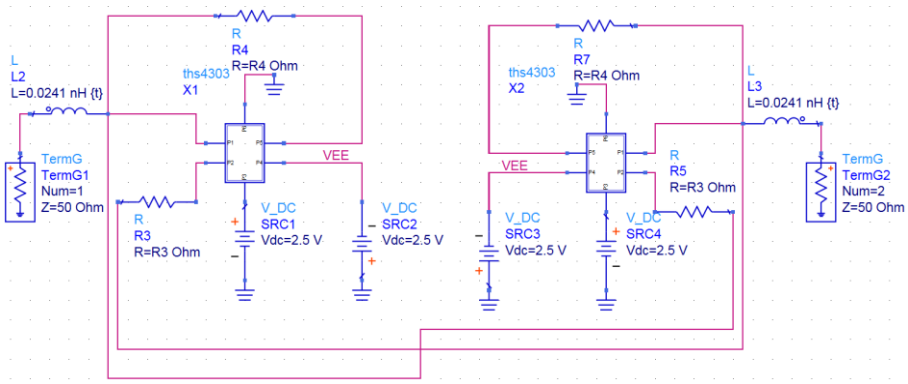

Fig. 6.10. Simulation setup of the two-port floating negative impedance converter using cross-coupled Texas Instruments THS4303.

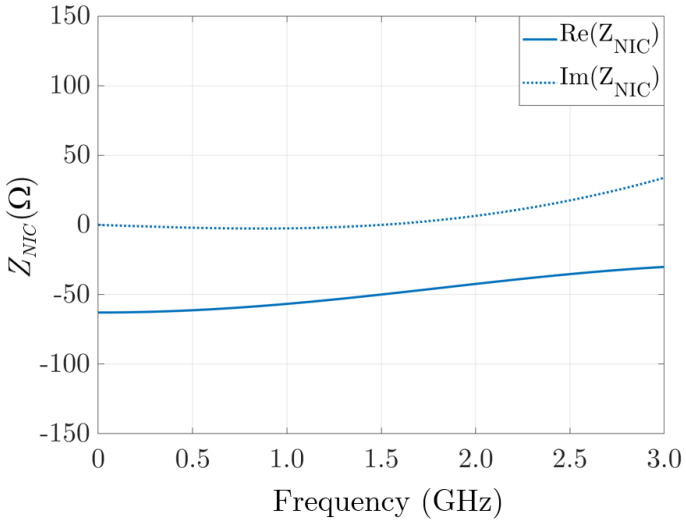

Fig. 6.11. Simulated results for the two-port floating negative resistance using THS4303.

6.2 Sensitivity Analysis of Exceptional Points

The design of gain element to implement realistic PT-symmetric circuits have been discussed in the previous section. The negative resistance may originate through the tunnel diode or the operational amplifier. Further, we discussed the ideal design of PT-symmetric circuit in series and shunt configurations at the exceptional point. We also estimated the noise figure of PT-symmetric system in chapter 3 and discussed the performance degradation at various noise levels. In this section, we will discuss another factor that can potentially degrade the PT-symmetric performance.

Although a practical and stable negative impedance converter is able to provide negative resistance at the particular frequency of interest, the magnitude of the negative resistor will not be able to exactly meet the following condition given by Eq. (6.2) at the exceptional point and will fluctuate depending on biasing and other circuit element uncertainties and component tolerances.

$$r = -R \,/\, Z_0 \tag{6.2}$$

The fluctuations in the magnitude of the gain resistor will cause the exceptional point of the PT-symmetric system to shift from its ideal location. This unwanted shift will degrade the PT-symmetric system performance depending on the uncertainty in the magnitude of the gain resistor which can be written as

$$r = \frac{1}{Z_0}(-R \pm \Delta) \tag{6.3}$$

where $-R$ is the gain resistor, Z_0 is the characteristic line impedance and Δ is the uncertainty in the magnitude of the gain resistor.

Considering the scattering parameters of the series PT-symmetric circuit designed in series and shunt configurations, given by Eqs. (3.6a)-(3.6c) and Eqs. (3.9a)-(3.9c), we can estimate the performance degradation in terms of fluctuating reflection and transmission coefficient in percentage expressed as a function of Δ which represents the uncertainty in the magnitude of the gain resistor.

For instance, a PT-symmetric system with zero gain resistor uncertainty, designed in series or shunt configuration with a capacitance of 4.45 pF and 1.1 pF respectively will exhibit following scattering matrix.

$$S = \begin{pmatrix} 0 & 1 \\ 1 & 1 \end{pmatrix}$$

However, with a gain resistor magnitude uncertainty, the reflection and transmission coefficients will increase or decrease depending on the design configuration as shown in Fig. 6.12.

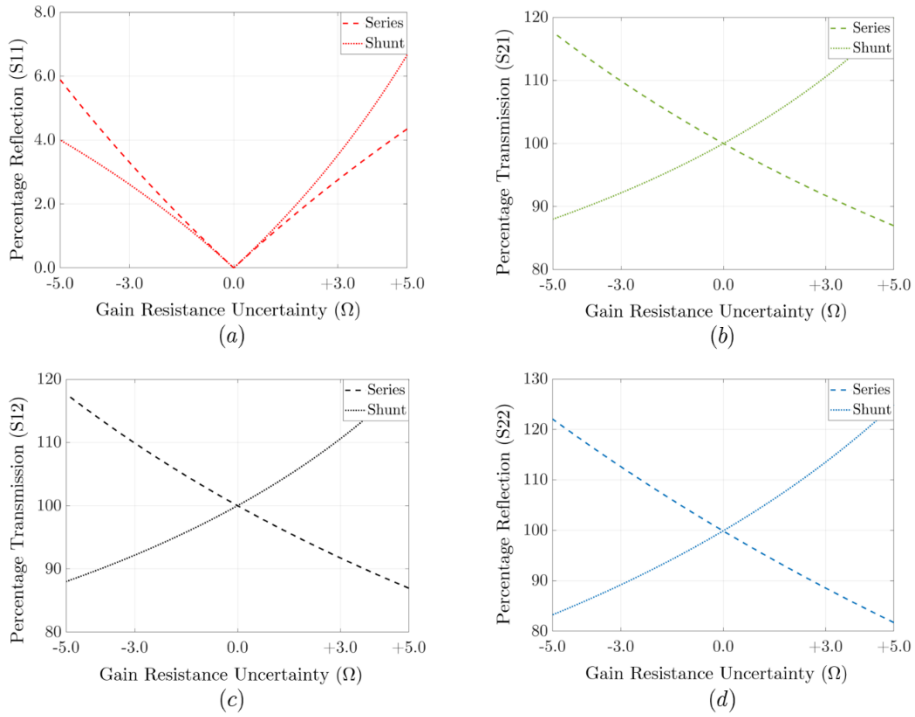

Fig. 6.12. Effect of an uncertain magnitude of the gain resistor on the performance of a PT-symmetric system.

Fig. 6.12(a) shows that with an increase or decrease in the magnitude of gain resistor, the reflection coefficient at the input port increases showing an impedance mismatch at the input port. The change is more noticeable for the PT-symmetric systems designed in series configuration which further concludes the robustness of the shunt design configuration.

Similarly, Fig. 6.12(b), Fig. 6.12(c) and Fig. 6.12(d) show the performance degradation of the forward transmission coefficient, reverse transmission coefficient and the output reflection coefficient respectively as the magnitude of gain resistor varies. The primary cause of this behaviour is the relocation of the exceptional point due to the imbalance of the loss and gain in the system. The results also conclude that the uncertainty in the magnitude of the negative resistance can cause weakly broken PT-symmetry resulting in system performance degradation.

6.3 Potential Applications of Negative Impedance Structures

We have discussed the realisation of negative resistance to be utilised as a time-reversed gain element in PT-symmetry through a NIC. PT-symmetric devices rely on purely real negative resistance to functional at exceptional points. However, NIC is also able to provide a negative imaginary impedances such as $-L$ or $-C$ that can be realised for interesting applications in communication and microwave electronics.

For instance, electrically small antennas are attractive solutions to the problem of space limitation but due to high reactance and fundamental gain-bandwidth limitations, they possess poor gain, low bandwidth and limited efficiency performance. Additionally, Fundamental limitations place

a maximum cap on passive matching bandwidths of small antenna [87–92]. Conventional matching techniques negate the reactance of ESAs only over a limited bandwidth by deploying inductors or capacitors, also known as Foster elements with positive reactance with increasing frequency [93]. However, non-Foster components such as negative inductors and capacitors, implemented through NIC are capable of cancelling the ESA reactance over broadband frequency ranges resulting in smaller antenna dimensions. A comparison between conventional and NIC based matching techniques for an electrically small antenna is shown in Fig. 6.13.

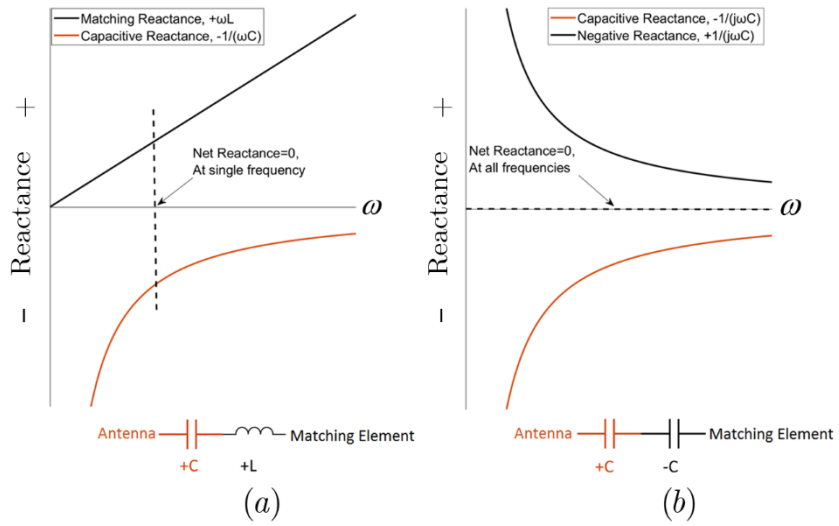

Fig. 6.13. Antenna impedance matching: a) conventional matching with an inductive reactance to cancel out a capacitive antenna at a single frequency; b) non-Foster element, -C to negate the capacitive reactance over a wider frequency range.

Fig. 6.13(a) shows that by using conventional antenna matching technique, the reactance of a small antenna is negated by an inductor at a single frequency. This is because the reactance of a conventional inductor is

frequency dependent property and as the frequency deviates from its original matching frequency, the matching quality or return loss degrades. This fundamental constraint limits the matching bandwidth of electrically small antennas [87-92].

Fig. 6.13(b) shows that a negative capacitance generated through a NIC is able to cancel the capacitive reactance of an electrically small antenna over wider frequencies ranges. Effectively, the fundamental bandwidth limitation has been overcome by the NIC resulting in a broad band electrically small antenna design which provides an attractive solution to space limited applications.

6.3.1 Non-Foster Antenna Arrays for Navigation Platforms

An important application that has received much attention is angle-of-arrival (AOA) or direction-of-arrival (DOA) estimation and radio localization of small autonomous systems such as UAVs and aerial vehicles where physical space is limited and high precision is required. The precision of such devices is dependent on various factors such as number of antenna elements, signal-to-noise ratio and signal processing algorithms. Fig. 6.14 shows a general setup for a direction-finding system.

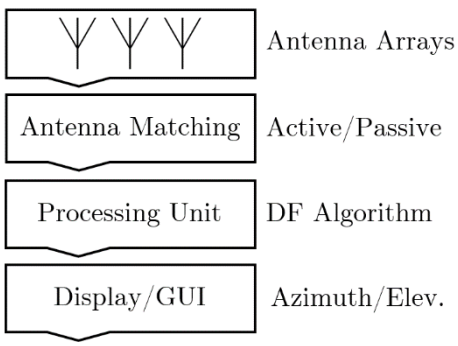

Fig. 6.14. A general setup for a direction-finding system.

We describe and propose an approach that combines the non-Foster matched broadband ESA techniques to achieve accurate theoretical localization and navigation of small radio platforms. In comparison with passive matching systems, non-Foster matching techniques for ESA arrays can provide advantages such as smaller size and wider bandwidth for radio direction-finding and localization applications.

a) Accuracy in Angle-of-Arrival Based Approaches

The Cramer-Rao lower bound (CRLB) is an important metric which provides the lower threshold of achievable theoretical accuracy of a direction-finding system [94–95]. Assuming a uniform circular antenna array geometry with N number of receiving elements for an AOA case, the relationship between minimum bearing variance θ and signal-to-noise ratio (SNR) can be derived through the Cramer-Rao relationship as [94–95]

$$\sigma_{CRLB}^2(\theta) \geq \frac{\lambda^2}{\pi^2 K D^2 \cos^2\phi}\left(\frac{1}{NSNR} + \frac{1}{N^2 SNR^2}\right) \tag{6.4}$$

Here, λ is the wavelength, K is the number of measurements taken, D is the diameter of the antenna array and ϕ is the elevation angle of the array element which is zero for a uniformly place antenna elements.

This important result concludes that given a constant physical space, greater number of antenna elements can be deployed with non-Foster matching networks such that the required SNR can be kept to minimum while maintaining the bearing angle estimates. Fig. 6.15 shows the required input SNR and the number of array elements necessary for bearing angle fluctuations of 2° and 0.5°respectively.

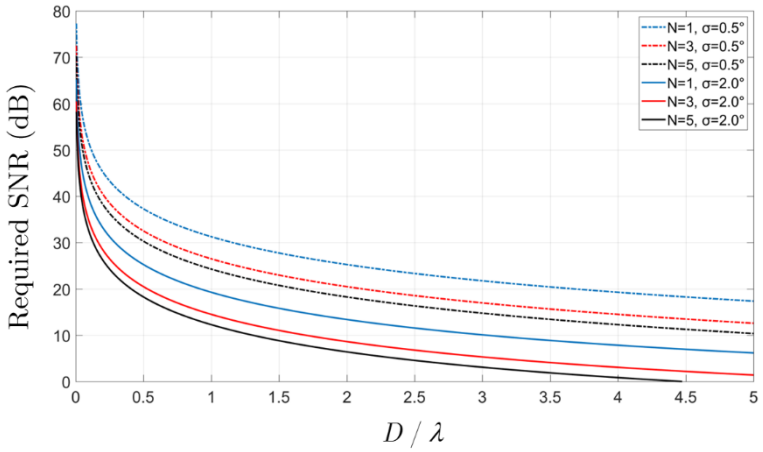

Fig. 6.15. Required SNR for N Electrically small antenna elements and specific angle precision σ; showing that for a specific array size D/λ, a dense array with more elements will require a lower SNR.

This important result concludes that given a constant physical space, greater number of antenna elements can be deployed with non-Foster matching networks such that the required SNR and bearing angle estimates can be kept to a minimum.

b) Accuracy in Time-of-Arrival Based Approaches

Non-Foster antenna matching techniques are also favourable in terms of ESA bandwidth enhancement, which is suitable in wideband localization as increased bandwidth is not only beneficial in terms of greater signal reliability, but also because it may contain more frequency components thus providing a better ranging estimate. The Cramer-Rao bound gives a lower bound on the estimation of the time delay under ideal conditions, which can be expressed in terms of Signal-to-Noise ratio and bandwidth to give ranging accuracy in terms of distance [94–95]. The expression for the time-delay is given as

$$\sigma^2_{CRLB}(t) = \frac{1}{8\pi^2 SNR}\frac{1}{B^2} \tag{6.5}$$

where B is the signal bandwidth. The expression can further be modified to give a lower bound variance on distance accuracy of a direction finding system as [94–95]

$$\mathrm{var}^2_{CRLB}(d) = \frac{c^2}{8\pi^2 SNR}\frac{1}{B^2} \tag{6.6}$$

Above expression shows that increased bandwidth yields a lower error in distance estimation which results in an increased precision in the ranging systems. For instance, a theoretical ranging error variance of a few centimetres is achievable for large bandwidths which are given through ESA elements. We assume here that the SNR is sufficiently high such that the Cramer-Rao bound remains valid. For lower SNR cases, other performance bounds such as Ziv-Zakai lower bound are more applicable [96].

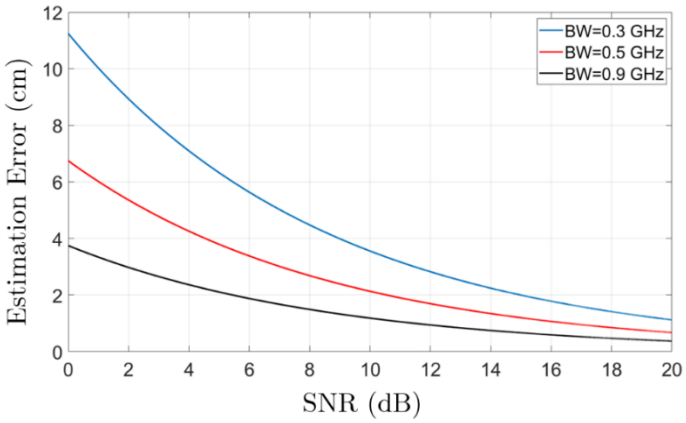

Fig. 6.16. Cramer-Rao lower bound for range estimation with various bandwidths

In a limited physical space, only specific numbers of passive array elements can be employed which results in fundamental bandwidth restriction. Non-Foster networks for ESAs yield wider bandwidth that favours high direction-finding accuracy for airborne or UAV applications with AOA and TOA direction-finding algorithms. Fig. 6.17 provides a visual comparison

between conventional antenna array with passive matching and electrically small antenna array, matched using non-Foster elements, offering improvement in terms of greater array elements and bandwidth.

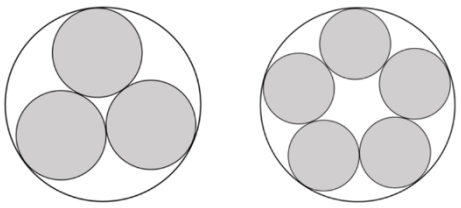

Fig. 6.17. ESA arrays in a constant physical space with (a) N=3 passive elements with fundamental size limit and; (b) N=5 non-Foster elements, which for the same bandwidth, can be smaller in size.

6.4 Summary

This chapter presented and discussed the ongoing simulation and experimental efforts to practically realise a functional gain element at microwave frequency ranges. The experimental setup using a tunnel diode and Keysight high precision SMU was performed to precisely record the DC characteristics of the diode. Further, the design of a grounded one-port negative resistor was shown by using Texas Instruments THS4303 operational amplifier. The one-port grounded NIC design is suitable for the PT-symmetric circuits designed in shunt configurations. Further, the design of a floating two-port negative resistor was also shown by using two cross-coupled operational amplifiers. The grounded one-port and floating two-port negative impedance was simulated through the measured data to provide a wide band negative resistance across microwave frequency range. Finally, the chapter discussed that the magnitude of a negative resistance provided by NIC is prone to uncertainties which can break the loss-gain balance in the PT-symmetric system. For this purpose, sensitivity analysis

of the gain resistor was performed which concluded that the uncertainty in the magnitude of the gain resistor results in a weakly broken PT-symmetry resulting in system performance degradation.

In addition, the chapter discussed that the real part of the negative impedance is favourable for designing gain element in PT-symmetric applications, whereas the imaginary part can be utilised to cancel the reactance of small antennas. For instance, electrically small antenna array design is possible through NIC impedance matching techniques. Potential applications of such arrays are direction-finding and navigation of small platforms where space limitation is a severe constraint.

Contribution Overview

- Presented the techniques to realise and implement gain element in PT-symmetry. Also described a highly accurate measurement setup with a precision of 100 nV to define the IV characteristics of a tunnel diode which can be incorporated as a gain element in PT-symmetric applications.

- Presented the design of a grounded, one-port negative impedance converter design at 1.5 GHz using an operational amplifier that is well suited for PT-symmetric circuits designed in shunt configurations.

- Presented the design of a floating, two-port negative impedance converter design at broadband microwave frequency ranges with a center frequency of 1.5 GHz. The NIC design is well suited for PT-symmetric circuits designed in both series and shunt circuit configurations.

Chapter 7

Discussion and Summary

7.1 Summary of the Work Presented in This Thesis

Parity-time (PT) symmetric systems are composed of balanced distributions of loss and gain which have been studied to propose exotic electromagnetic wave-manipulation and scattering. These include non-linear wave propagation, negative refraction, cloaking and invisibility, acoustic isolators, acoustic circulators, sensors and more. In RF and microwave electronics, loss originates through a conventional positive resistor whereas the gain is realized as a negative resistor which is artificially engineered through negative impedance converters (NIC) designed using BJT, op-amp and tunnel diodes. The design of a stable NIC at microwave frequency ranges is itself a provocative task to achieve. In order to design and transition the theoretical knowledge into functional PT-symmetric devices, significant level of control and stability is required over the loss and gain elements. The primary bottlenecks in designing and implementing PT-symmetric devices at microwave frequency ranges are noise and instability which can break the balance of loss and gain eventually causing a fluctuation in the location of exceptional points. Although stability is potentially achievable through careful system design, thermal noise is a fundamental property of systems exhibiting loss and gain and hence cannot be avoided. Therefore noise characterisation and the performance study of PT-symmetric systems in realistic scenarios is crucial prior to any design considerations.

The work presented in this thesis investigates the design of PT-symmetric systems and proposes a convenient technique to manipulate the associated reflection and transmission behavior. The analytical, simulated and measurement studies of PT-symmetric systems in terms of their design configurations, noise figure and signal-to-noise (SNR) ratio is presented.

Chapter 1 provided an overview and motivation that compelled to the choice of the topic and studies presented in the thesis. It also presented and highlighted the novel contributions which relate the noise performance of PT-symmetric applications to PT-symmetry in microwave electronics. The second chapter presented the underlying theoretical and physical concepts that underlay the foundation of the research work performed in this thesis. It described the fundamentals of parity (P), time-reversal (T) and combined parity-time (PT) postulates in RF electronics.

The design of two-port, ideal PT-symmetric systems using lumped elements in series and shunt configurations was presented in chapter 3. It was shown that an imaginary impedance combining loss and gain enables the manipulation of the output reflection coefficient at the exceptional point where the loss and gain are exactly balanced. At this point the system exhibits unidirectional properties at an electrical length of $x = n\pi / 2$, where the magnitude of the input reflection coefficient (S_{11}) is zero whereas the forward (S_{21}) and reverse (S_{12}) transmission coefficients are unity due to reciprocity. However, the output reflection coefficient (S_{22}) magnitude is defined by the choice of imaginary impedance in the PT-symmetric system which may originate through an inductive and capacitive element in the system. The studies showed the scattering notation of a PT-symmetric in series and shunt configurations and then presented the scattering properties as a function of electrical length and capacitive or inductive impedances.

Chapter 4 presented the noise characterisation equivalent noise models of the PT-symmetric systems in series and shunt configurations. Since PT-symmetric systems are implemented as loss and gain resistors in microwave electronic systems, the most dominant noise source originate through the loss (passive) and gain (active) elements. The lossy passive resistor is a source of thermal noise modelled as a noiseless resistor with equivalent voltage noise source whereas the gain resistor was realized through a tunnel diode. The choice of a tunnel diode in the realisation of a negative resistor was because it consumes very low power and exhibits least number of active elements that favor stability and minimum overall noise figure. The chapter presented the equivalent noise models of the PT-symmetric systems described in Chapter 3, and compared the analytical and simulated noise figure in each aforementioned circuit design at 1.5 GHz.

Chapter 5 reviewed and discussed an ideal unidirectional PT-symmetric cloak with balanced loss and gain under ideal, loss and noise-free conditions to realize perfect unidirectional invisibility from the loss side. Following the results from chapter 3, the chapter proposed a bidirectional metasurface cloak where the input and output reflection coefficient from loss and gain side incidence are vanished, allowing unitary transmission and structural transparency. The proposed cloaking model provides unidirectional and bidirectional cloaking depending on the capacitive or inductive impedances.. The chapter then evaluated the performance of the proposed PT-symmetric cloak in series and shunt design configurations and computed the radar cross-section (RCS) of a cloaked target in the presence of various noise figure levels. The chapter formulated that the cloaking circuit model in series design configuration offers a reduced noise figure in comparison with shunt topology. The chapter finally discussed the design of an electromagnetic switch based on PT-symmetry, where the transmission and

reflection can be manipulated through the choice of capacitive and inductive impedance. The studies performed and presented in this chapter were validated using analytical techniques whereas circuit level and full-wave electromagnetic simulations were carried out using commercially available software simulation packages.

Chapter 6 showed the experimental and simulation techniques to realise a negative impedance converter at microwave frequencies. The negative impedance can originate through a tunnel diode or an operational amplifier at microwave frequency ranges. For this purpose, the experimental setup to measure current-voltage relationship of the tunnel diode has been described using high precision source measurement unit (SMU) with an accuracy of 100 nV. The SMU was configured through National Instruments GPIB interface using MATLAB equipment control toolbox. The DC biasing voltage across the diode was then swept and the current across the diode was recorded. By computing the derivative of the voltage with respect to the current, the negative differential biasing region is determined. The diode showed a purely negative resistance of -50 Ω at a biasing voltage of 0.191 mV which is well suited for PT-symmetric circuit design in series and shunt configurations.

The chapter also discussed the design of a negative impedance converter through an operational amplifier. The design of a grounded one-port NIC was demonstrated through simulation techniques and measured data of Texas Instruments THS4303 wideband, fixed gain operational amplifier. The aforementioned one-port design was configured in a negative feedback loop to provide a purely negative resistance of -50 Ω which is favorable for the PT-symmetric circuits designed in shunt configurations.

Similarly, the design of a floating two-port negative resistor was demonstrated by using two cross-coupled THS4303 operational amplifiers to provide a flat negative resistance of -50 Ω at broad range of microwave frequencies. In addition, the chapter discussed that uncertainty in the magnitude of negative resistance provided by NIC may break the loss-gain balance in the PT-symmetric system. Finally, the chapter discussed additional applications of a negative impedance converters such as electrically small antenna arrays for navigation of small platforms.

7.2 Future Research Work

PT-symmetry in electromagnetics and RF electronics is relatively young research concept. Despite its origination in quantum mechanics in 1998, the research has been widely spread to optics, optical waveguides, sensors, medical applications and electronics leading to exciting engineering applications. Specifically in RF and microwave electronics, the concept is still evolving in terms of practical applications. Although, researchers have proposed theoretical studies of PT-symmetric applications such as invisibility cloaks and sensors at low frequency ranges, practical implementation at radio frequency ranges is much challenging task to accomplish. This is primarily due to high losses, NIC design, stability and increase noise figure levels.

The purpose of the studies presented in this thesis was to pave the way in terms of practical implementation and the performance of PT-symmetric devices operating at microwave frequency ranges. Practical implementation of functional PT-symmetric devices such as wide-band invisibility cloaks requires further modelling and research experimentations, all of which is beyond the scope of this thesis. The studies presented in this research thesis

provides an insight to the challenges and constraints in implementing PT-symmetric applications and the performance levels under realistic environment such as in the presence of noise and system uncertainties. However, further work in the subject of PT-symmetry at microwave electronics has sufficient potential that could lead to further applications and engineering publications.

References

1. C. Bender and S. Boettcher, "Real Spectra in Non-Hermitian Hamiltonians Having PT Symmetry," Phys. Rev. Lett. 80, 5243-5246 (1998).
2. C. M. Bender, D.C. Brody and H. F. Jones, "Complex Extension of Quantum Mechanics," Phys. Rev. Lett. 89, 270401 (2002).
3. C. M. Bender, "Introduction to PT -symmetric quantum theory," Contemp. Phys. 46, 277 (2005).
4. C. M. Bender, Making sense of non-Hermitian Hamiltonians. Rep. Prog. Phys. 70, 947 (2007).
5. C. M. Bender, S. Boettcher, and P. N. Meisinger, "PT-symmetric quantum mechanics," J. Math. Phys. 40, 2201 (1999).
6. A. Mostafazadeh, "Pseudo-Hermiticity versus PT Symmetry: The Necessary Condition for the Reality of the Spectrum of a Non-Hermitian Hamiltonian," J. Math. Phys. (N.Y.) 43, 205 (2002).
7. G. Le´vai and M. Znojil, "Systematic Search for PT-Symmetric Potentials with Real Energy Spectra," J. Phys. A 33, 7165 (2000).
8. R. El-Ganainy, K.G. Makris, D. N. Christodoulides, and Z. H. Musslimani, "Theory of Coupled Optical PT-Symmetric Structures," Opt. Lett. 32, 2632 (2007).
9. K. G. Makris, R. El-Ganainy, D. N. Christodoulides, and Z. H. Musslimani, "Beam Dynamics in PT Symmetric Optical Lattices," Phys. Rev. Lett. 100, 103904 (2008).
10. X. Zhu, H. Ramezani, C. Shi, J. Zhu, and X. Zhang, "PT-Symmetric Acoustics," Phys. Rev. X 4, 031042 (2014).
11. R. Fleury, D. Sounas, and A. Alu, "An invisible acoustic sensor based on parity-time symmetry," Nat. Commun. 6, 5905 (2015).

12. F. Bagarello, "Linear pseudo-fermions," J. Phys. A, 45, 444002, (2012).
13. J. Schindler, Z. Lin, J. M. Lee, H. Ramezani, F. M. Ellis, and T. Kottos, "PT-symmetric electronics" J. Phys. A Math. Theor. 45, 444029 (2012).
14. J. Schindler, A. Li, M. C. Zheng, F. M. Ellis, and T. Kottos, "Experimental study of active LRC circuits with PT symmetries" Phys. Rev. A 84, 040101 (2011).
15. C. Poli, M. Bellec, U. Kuhl, F. Mortessagne, and H. Schomerus, "Selective enhancement of topologically induced interface states in a dielectric resonator chain," Nat. Commun. 6, 6710 (2015).
16. S. Bittner, B. Dietz, U. Gunther, H. L. Harney, M. Miski-Oglu, A. Richter, and F. Schafer, "PT symmetry and spontaneous symmetry breaking in a microwave billiard," Phys. Rev. Lett. 108, 024101 (2012).
17. Hassan Farooq, Khalid Z. Rajab, and Yang Hao, "Noise figure of electromagnetic systems with parity and time-reversal symmetry," Opt. Express 27, 31363-31375 (2019).
18. L. Chang, X. Jiang, S. Hua, C. Yang, J. Wen, L. Jiang, G. Li, G. Wang, and M. Xiao, "Parity-time symmetry and variable optical isolation in active passive-coupled micro-resonators," Nat. Photonics 8, 524 (2014).
19. A. Regensburger, C. Bersch, M.-A. Miri, G. Onishchukov, D. N. Christodoulides, and U. Peschel, "Parity-time synthetic photonic lattices," Nat. 488, (2012).
20. S. Longhi, "Invisibility in PT-symmetric complex crystals," J. Phys. A Math. Theor. 44, 485302 (2011).

21. H. F. Jones, "Analytic results for a PT -symmetric optical structure," J. Phys. A Math. Theor. 45, 135306 (2012).
22. M. Kulishov, J. M. Laniel, N. Bélanger, J. Azaña, and D. V. Plant, "Nonreciprocal waveguide Bragg gratings," Opt. Express 13(8), 3068–3078 (2005).
23. J. Čtyroký, V. Kuzmiak, and S. Eyderman, "Waveguide structures with antisymmetric gain/loss profile," Opt. Express 18(21), 21585–21593 (2010).
24. C. M. Bender, B. K. Berntson, D. Parker, and E. Samuel, "Observation of PT phase transition in a simple mechanical system," Am. J. Phys. 81, 173 (2013).
25. R. Fleury, D. L. Sounas, and A. Alù, "Negative Refraction and Planar Focusing Based on Parity-Time Symmetric Metasurfaces," Phys. Rev. Lett. 113, 023903 (2014).
26. Z. Lin, H. Ramezani, T. Eichelkraut, T. Kottos, H. Cao, and D. N. Christodoulides, "Unidirectional invisibility induced by PT-symmetric periodic structures," Phys. Rev. Lett. 106, 213901 (2011).
27. B. Peng, S. K. Ozdemir, F. Lei, F. Monifi, M. Gianfreda, G. L. Long, S. Fan, F. Nori, C. M. Bender, and L. Yang, "Parity-time-symmetric whispering-gallery microcavities," Nat. Phys. 10, 394-398 (2014).
28. Kord, Ahmed, Dimitrios L. Sounas, and Andrea Alù. "Active Microwave Cloaking Using Parity-Time-Symmetric Satellites." Phys. Rev. A, 10, 054040 (2018).
29. D. L. Sounas, R. Fleury, and A. Alù, "Unidirectional cloaking based on metasurfaces with balanced loss and gain," Phys. Rev. A, 4, 014005 (2015).

30. Z. Lin, H. Ramezani, T. Eichelkraut, T. Kottos, H. Cao and D. Christodoulides, "Unidirectional Invisibility Induced by PT-Symmetric Periodic Structures," Phys. Rev. Lett. 106, 213901 (2011).
31. A. Regensburger, C. Bersch, M.A. Miri, G. Onishchukov, D. N. Christodoulides, and U. Peschel, "Parity - time synthetic photonic lattices," Nat. 488, 167-171 (2012).
32. Mostafazadeh, Ali. "Invisibility and PT symmetry," Phys. Rev. A, 87 012103 (2013).
33. L. Feng, Y. L. Xu, W. S. Fegadolli, M. H. Lu, J. E. Oliveira, V. R. Almeida, Y. F. Chen, and A. Scherer, "Experimental demonstration of a unidirectional reflectionless parity-time metamaterial at optical frequencies," Nat. Mater. 12(2), 108–113 (2012).
34. Assawaworrarit, Sid, Xiaofang Yu, and Shanhui Fan. "Robust wireless power transfer using a nonlinear parity–time-symmetric circuit," Nat. 546.7658 (2017).
35. Y. J. Zhang, H. Kwon, M.A. Miri, E. Kallos, H. CanoGarcia, M. S. Tong, and A. Alu, "Non-invasive glucose sensor based on parity-time symmetry," Phys. Rev. App., 11, 4, 044049 (2019).
36. K. Z. Rajab, Y. Hao, D. Bao, C. G. Parini, J. Vazquez, and M. Philippakis, "Stability of active magnetoinductive metamaterials," J. App. Phys. 108, 054904 (2010).
37. K. V. Kepesidis, T. J. Milburn, J. Huber, K. G. Makris, S. Rotter & P. Rabl, "PT-symmetry breaking in the steady state of microscopic gain–loss systems," New J. Phys., 18, 095003 (2016).
38. J. Maxwell, "A dynamical theory of the electromagnetic field," Phil. Trans. R. Soc. 155, 459512 (1865).
39. J.C. Maxwell, "On physical lines of force", Phil. Mag. S. 4, Vol. 21, No. 139, p. 161 (1861).

40. S. Ramo, J. R. Whinnery, and T. V. Duzer, *Fields and Waves in Communication Electronics,* 3rd ed. (John Wiley, 1999),
41. K. Zhang and D. Li, *Electromagnetic Theory for Microwaves and Optoelectronics,* 2nd ed. (Springer, 2008),
42. C. A. Balanis, *Advanced Engineering Electromagnetics*, 2nd ed. (John Wiley, NJ, 2012).
43. R. E. Collin, *Field Theory of Guided Waves,* 2nd ed. (IEEE Press, NY, 1991).
44. J. P. Paul, C. Christopoulos, D. W. P. Thomas, "Generalized material models in TLM-Part 2: Materials with anisotropic properties," IEEE Trans. Antennas Propag. 47, 1535-1542 (1999).
45. L. D. Landau, J. S. Bell, M. J. Kearsley, L. P. Pitaevskii, E. M. Lifshitz, and J. B. Sykes, *Electrodynamics of Continuous Media,* 2nd ed. (Elsevier, London, England, 1984).
46. D. M. Pozar, *Microwave Engineering,* 4th ed. (John Wiley, New York, NY, 2011).
47. H. A. Haus, *Waves and Fields in Optoelectronics* (Prentice-Hall, New Jersey, 1983).
48. J. M. Liu, *Photonic Devices* (Cambridge University Press, Cambridge, 2005).
49. K. Iizuka, *Elements of Photonics*, Vol II (John Wiley, New York, NY, 2002).
50. J. Schindler, A. Li, M. C. Zheng, F. M. Ellis, and T. Kottos, "Experimental study of active LRC circuits with PT symmetries," Phys. Rev. A, 84, 040101 (2011).
51. N. Zettili, Quantum Mechanics: Concepts and Applications, 2nd ed. (John Wiley, New York, NY, 2009).

52. A. Yariv, *Quantum Electronics,* 3rd ed. (John Wiley, New York, NY, 1989).

53. S. Klaiman, U. Gunther, and N. Moiseyev, "Visualization of Branch Points in PT-Symmetric Waveguides," Phys. Rev. Lett. 101, 080402 (2008).

54. L. Ge, Y. D. Chong, and A. D. Stone, "Conservation relations and anisotropic transmission resonances in one-dimensional PT-symmetric photonic heterostructures," Phys. Rev. A 85(2), 023802 (2012).

55. Y. D. Chong, L. Ge, and A. D. Stone, "PT-symmetry breaking and laser-absorber modes in optical scattering systems," Phys. Rev. Lett. 106, 093902 (2011).

56. S. Longhi, "PT-symmetric laser absorber," Phys. Rev. A 82, 031801 (2010).

57. A. Mostafazadeh, "Spectral singularities of complex scattering potentials and infinite reflection and transmission coefficients at real energies," Phys. Rev. Lett. 102, 220402 (2009).

58. C. Vassallo, *Optical Waveguide Concepts*, 1st ed. (Elsevier, New York, NY, 1991).

59. J. B. Pendry, "Negative refraction makes a perfect lens." Phys. Rev. Lett. 85, 3966 (2000).

60. J.G. Linvill, "Transistor negative impedance converters," Proc. IR 41, 725 (1953).

61. J.L. Merrill, "Theory of the negative impedance converter", Bell Sys. Tech. J. 30, 88 (1951).

62. A. Larky, "Negative-impedance converters," IRE Trans. Circuit Theory, 124131, (1957).

63. Esaki, L., 1958, "New Phenomenon in Narrow Germanium p−n Junctions," Phys. Rev. 109, 603.

64. D. S. Nagarkoti, Y. Hao, D. P. Steenson, L. Li, E. H. Linfield, K. Z. Rajab, "Design of broadband non-Foster circuits based on resonant tunnelling diodes," IEEE Antennas Wireless Propag. Lett. 15, 1398 (2015).

65. Tade, O.O., Gardner. P., Hall, S.S. "Antenna bandwidth broadening with a negative impedance converter," Int. J. Microwave T. 249-260 (2013).

66. Sussman–Fort SE, Rudish RM. "Non-foster impedance matching of electrically-small antennas," IEEE Trans. Antennas Propag. 2230–2241 (2009).

67. F. Albarracin-Vargas, V. Gonzalez-Posadas, F. J. Herraiz-Martinez, and D. Segovia-Vargas. "Design method for actively matched antennas with non-foster elements," IEEE Trans. Antennas Propag. 4118–4123 (2016).

68. H. Mirzaei and G. V. Eleftheriades. "A resonant printed monopole antenna with an embedded non-foster matching network," IEEE Trans. on Antennas Prop. 5363–5371 (2013).

69. S. Saadat, H. Aghasi, E. Afshari, and H. Mosallaei, "Low-power negative inductance integrated circuits for GHz applications," IEEE Microw. Wireless Compon. Lett. 118–120 (2015).

70. J. B. Johnson. "Thermal Agitation of Electricity in Conductors," Phys. Rev. (1928).

71. P. Horowitz, and W. Hill, *The art of electronics* (Cambridge Univ. Press, 1989).

72. McWhorter, A. "1/f Noise and Related Surface Effects in Germanium," MIT Lincoln Laboratory: Cambridge, MA, (1955).

73. Hooge F. N. "1/f noise is no surface effect," Phys. Lett. 139–140 (1969).
74. Friis, H.T., "Noise Figures of Radio Receivers," Proc. of the IRE, 419-422 (1944).
75. Lane, Richard Q., "The Determination of Device Noise Parameters," Proc. of the IEEE, 1461-1462 (1969).
76. Caruso and Sannino, "Computer-Aided Determination of Microwave Two-Port Noise Parameters," IEEE Trans. On Microwave Theory and Techniques) 639-642 (1978).
77. R. W. Landee, *Electronic Designers*. New York: McGraw-Hill (1957).
78. G Gonzalez, *Microwave Transistor Amplifiers*, Prentice-Hall (1984).
79. B. Razavi *RF microelectronics*, Vol. 1. New Jersey: Prentice hall (1998).
80. C. A. Balanis, *Antenna Theory: Analysis and Design,* John Wiley & sons (2016).
81. S. R. Saunders and S. R. Simon, *Antennas and Propagation for Wireless Communication Systems,* (John Wiley, New York, NY, 1999).
82. H. Farooq, D. S. Nagarkoti, K. Z. Rajab, & Y. Hao, (2019, March). Noise Figure of a Unidirectional Cloaking Circuit Based on Parity-Time Symmetry. In *2019 13th European Conference on Antennas and Propagation (EuCAP)* (pp. 1-3) (2019).
83. Y. Fan, K. Z. Rajab, Y. Hao, Noise analysis of broadband active metamaterials with non-Foster loads, J. Appl. Phys. 113, 233905 (2013).

84. Shi, C., Dubois, M., Chen, Y., Cheng, L., Ramezani, H., Wang, Y. and Zhang, X., "Accessing the exceptional points of parity-time symmetric acoustics" Nat. Comm. 7, 11110 (2016).

85. [Online]. Available: http://www.ti.com/product/THS4303.

86. [Online]. Available: https://www.keysight.com/en/pd-1983602-pn-B2912A.

87. H. A. Wheeler, "Fundamental limitations of small antennas," Proc. IRE, 1479 (1947).

88. L. Chu, "Physical limitations of omni-directional antennas," J. Appl. Phys., 1163 (1948).

89. R. F. Harrington, "Effect of antenna size on gain, bandwidth and efficiency," J. Res. Nut. Bur. Stund., 64 (1960).

90. H. W. Bode, *Network Analysis and Feedback Amplifier Design.* (New York, NY, 1947).

91. R. M. Fano, "Theoretical limitations on the broadband matching of arbitrary impedances," J. Franklin Inst. 57–83 (1950).

92. D. C. Youla, "A new theory of broad-band matching," IEEE Trans. Circuit Theory, 30–50 (1964).

93. R. M. Foster, "A reactance theorem," Bell Syst. Tech. J. 259–267 (1924).

94. Cramer, H. *Mathematical methods of statistics.* (Princeton University Press, 1946).

95. T. Tuncer and B. Friedlander, *Classical and Modern Direction-of-Arrival Estimation.* (New York, NY, 2009).

96. K. L. Bell, Y. Steinberg, Y. Ephraim, and H. L. V. Trees, "Extended Ziv-Zakai lower bound for vector parameter estimation," IEEE Trans. Inf. Theory, 624–637 (1997).